INFORMATION TO USERS

This manuscript has been reproduced from the microfilm master. UMI films the text directly from the original or copy submitted. Thus, some thesis and dissertation copies are in typewriter face, while others may be from any type of computer printer.

The quality of this reproduction is dependent upon the quality of the copy submitted. Broken or indistinct print, colored or poor quality illustrations and photographs, print bleedthrough, substandard margins, and improper alignment can adversely affect reproduction.

In the unlikely event that the author did not send UMI a complete manuscript and there are missing pages, these will be noted. Also, if unauthorized copyright material had to be removed, a note will indicate the deletion.

Oversize materials (e.g., maps, drawings, charts) are reproduced by sectioning the original, beginning at the upper left-hand corner and continuing from left to right in equal sections with small overlaps. Each original is also photographed in one exposure and is included in reduced form at the back of the book.

Photographs included in the original manuscript have been reproduced xerographically in this copy. Higher quality 6" x 9" black and white photographic prints are available for any photographs or illustrations appearing in this copy for an additional charge. Contact UMI directly to order.

U·M·I

University Microfilms International
A Bell & Howell Information Company
300 North Zeeb Road, Ann Arbor, MI 48106-1346 USA
313 761-4700 800 521-0600

Order Number 9229211

Photoelectron angular distributions and phase interference in alkali atoms

Yin, Yi-Yian, Ph.D.

Purdue University, 1992

U·M·I
300 N. Zeeb Rd.
Ann Arbor, MI 48106

Graduate School Form 9
(Revised 8/89)

PURDUE UNIVERSITY
GRADUATE SCHOOL
Thesis Acceptance

This is to certify that the thesis prepared

By Yin Yi-Jian

Entitled

[illegible]

Complies with University regulations and meets the standards of the Graduate School for originality and quality

For the degree of [illegible]

Signed by the final examining committee:

Daniel S Elliott, chair

C Lee

E R Grant

S Datta

Approved by:

R J Schwarz
Department Head Date

This thesis ☐ is. ☒ is not to be regarded as confidential

Daniel S Elliott
Major Professor

PHOTOELECTRON ANGULAR DISTRIBUTIONS AND PHASE INTERFERENCE IN ALKALI ATOMS

A Thesis

Submitted to the Faculty

of

Purdue University

by

Yi-Yian Yin

In Partial Fulfillment of the

Requirements for the Degree

of

Doctor of Philosophy

May 1992

This thesis is dedicated to my
mother, father, and my family
for their love and support

ACKNOWLEDGEMENTS

The author wishes to express his warmest appreciation to his major professor Daniel S. Elliott for his proposing this project, for his valuable academic advice and joint laboratory work. Thanks are also due to other members of my Ph.D Advisory committee - Drs. Chin-Lin Chen, Edward R. Grant and Supriyo Datta for their valuable time and interest in my work.

I would like to thank other students who workes in our lab, especially Ce Chen. Numerous conversations and help throughout this project were invaluable. Help and encouragement from Edward J. Bodette, Bruce A. Ferguson, Cheng Xie are also greatly appreciated.

I would like to thank those who provided help necessary for completing this project. Mr. Claude Harrington in Machine Shop, and other in EE Department are appreciated for their great help.

I would like to thank wholeheartedly my wife De-Ying Yang and my daughter Song Yin for their understanding, encouragement and support. Without their cooperation, I would not have been able to complete my graduate study.

This work is supported by National Science Foundation, Grant No. PHY-9017244, Without it this work would not have been completed.

TABLE OF CONTENTS

Page

LIST OF TABLES

LIST OF FIGURES

Figure Page

ABSTRACT

Yin, Yi-Yian. Ph.D., Purdue University, May 1992. Photoelectron angular distributions and phase interference in alkali atoms. Major Professor: Dr. Daniel S. Elliott.

In this thesis we report an experimental study of the interference between one- and two-photon ionization processes from the ground state of rubidium atom. This interference is observed by measuring the photoelectron angular distribution under the influence of fundamental and second harmonic laser fields. Externally controlling the relative phase and amplitude between these two laser fields, we obtained interference in the angular distribution patterns. This study represents the first observation of the phase interference in photoionization angular distributions.

The photoelectron angular distributions resulting from the single-photon ionization of cesium and rubidium from its ground state to the continuum were measured. This is the first set of measurements of the single photon photoelectron angular distributions at a variety of energies in vicinity of the Cooper minimum from a single initial state of alkali metals. The results show a strong variation of asymmetry parameter β from its nonrelativistic value of 2. Spin-orbit coupling displaces the minimum in the cross section for excitation to the $\varepsilon P_{1/2}$ and $\varepsilon P_{3/2}$ and results in a rapid variation of the angular distribution with photon energy in this region.

Through the measurement of two-photon ionization angular distributions the quantum defects and spin-orbit coupling were investigated. These studies help us to understand the phase interference interaction, and the data in those studies would be used to analyze the interference processes.

CHAPTER 1
INTRODUCTION

1.1 Introduction

In this thesis we discuss measurements of photoelectron angular distributions for alkali atoms, the effects of spin-orbit coupling in alkali atoms and an optical interference phenomenon between one-photon and two-photon ionization processes.

In modern physics, measurements of collision processes can provide a great deal of information concerning the structure of the colliding particles. Experimental measurements of the total cross section and corresponding theoretical calculations give us information about the particle structure and their interaction. In addition to measurements of the total cross section, the angular distribution of scattered particles can be extremely useful. These distributions are sensitive to not only the transition amplitudes of various interactions, but also their relative phases. These data let us understand the initial and final states of the target as well as dynamic information on the collision process itself. The measurement of photoelectron angular distributions as one of the basic tools for the exploration of atomic and molecular structure is attracting more and more attention. Measurements of such angular distributions have been increasingly used for the purpose of studying atomic structure as well as the fundamental properties of the interaction of light with atoms or molecules.

Early in 1924, Bothe [1.1] first observed the electron angular distribution for one-photon ionization using x-rays to irradiate various molecules such as $CHCl_3$ and C_2H_5Br. For such high energy photons the momentum of the photon is not negligible with respect to the momentum of the bound electron. This results in a distortion

of the photoelectron angular distribution due to momentum transfer. Wentzel [1.2, 1.3] in 1926 first showed experimently the electrons ejected from K-shells would exhibit a $\sin^2\theta$ angular dependence, where θ is the angle between the incident light beam and the ejected electron path. Bethe [1.4] proved that within the limitations of using single electron wave functions in a central field, the angular distribution of electrons from any shell of arbitrary quantum numbers n, l is of the form $\alpha+\beta\sin^2\theta$. Other early studies of photoelectron angular distributions include that of Chaffee in 1931 [1.5].

In 1966 the angular distribution of photoelectrons from argon and xenon produced by the 58.4 nm helium resonance line was measured by Berkowitz and Ehrhardt [1.6]. They found that the photoelectron angular distribution has a maximum at 90° to the incident light beam. This was the first measurement of a photoelectron angular distribution with photon energies less than 10 eV. At this energy of the photon, the momentum transfer can be neglected. Several theoretical analyses of angular distributions in atomic and molecular photoionization were carried out for many facets of the subject [1.7-1.19]. Bebb determined two-photon ionization rates for alkali atoms theoretically and suggested that cesium, excited by a frequency doubled ruby-laser beam, would exhibit a non-resonant process in which a single intermediate state would dominate the process. Tully, Berry, and Dalton [1.12] in 1968 studied relaxation processes between magnetic substates induced by collisions. They derived nonrelativistic differential cross sections for photoionization of molecular systems with random orientation. Their work helped our understanding of the process of vibrationally induced autoionization and the interpretation of some angular distribution experiments in molecules.

In 1974 Edelstein, Lambropoulos, Duncanson, and Berry [1.20] first reported the multiphoton ionization angular distributions of electrons. In their experiment, titanium atoms were ionized by the light of a nitrogen laser from the low-lying excited a^3F_4 state. The measured angular distribution of photoelectrons from the process

gives limits on the ratio of amplitudes for transitions from the intermediate state to the final continuum S and D channels. The photoionization cross section for titanium from the excited state was determined as 1×10^{-18} cm^2 by measurement of the total number of photoelectrons.

From that time people began to use angular distributions to study various features of atomic electronic structure. In 1979 Leuchs, Smith, Khawaja, and Walther [1.21] studied a quantum interference effect. They measured the quantum beats of the hyperfine levels of the $3^2P_{3/2}$ state of sodium in photoionization. In this experiment the atoms were ionized stepwise by two pulsed lasers with a time delay between them. The photoelectron angular distribution as a function of time delay exhibits a periodic variation due to the quantum beat effect. This result provided a good measurement for hyperfine splitting of the intermediate state.

Kaminski, Kessler, and Kollath [1.22] and Strand, Hansen, Chen, and Berry [1.23] studied the phase shifts between continuum state wave functions separately. Angular distributions may be profoundly affected by interference between final-state partial waves of the outgoing electrons and can be used to obtain information about the ratio of the allowed transition amplitudes. In the Kaminski, Kessler, and Kollath experiment, a measurement of the angular distribution and spin polarization of the photoelectrons produced by linearly polarized light from 7^2P excited states of cesium was performed. The result was used to determine the relative phase difference $\phi_s - \phi_d$ for $\varepsilon^2S_{1/2}$ and $\varepsilon^2D_{3/2}$ continuum states and the transition matrix elements describing the photoionization process for the cesium excited state.

Feldmann and Welge [1.24, 1.25] in 1982 studied the characteristics of autoionizing states. Using tunable laser radiation between 555 and 557 nm, they showed that the angular distribution of photoelectrons sensitively reflects the influence of bound two-photon resonances and autoionizing three-photon resonances for selected wavelengths for strontium.

Angular distributions of photoelectrons from ground or excited states of atoms through resonant excitation usually depend strongly on the properties of resonant intermediate states and the final continuum states. Photoelectron angular distributions may reflect the mixture and the interaction of intermediate state wave functions. From 1980 to 1984 the ac-Stark effect on angular distributions was studied by Dixit, Lambropoulos, and Zoller [1.26-1.28] theoretically. They presented the theory of photoelectron angular distributions in resonant multiphoton ionization that rigorously takes into account saturation, the ac-Stark shift, and the laser linewidth effects. The theory shows that the influence of these effects on the distribution is incorporated through the coupling equations between the angle-resolved ionization probability and the bound state density matrix elements. In 1984 Ohnesorge, Diedrich, Leuchs, Elliott, and Walther [1.29] reported measurements of the effect of the ac-Stark shift on the angular distribution. In their experiment the influence of the dynamic Stark effect on photoelectron angular distribution for two-photon resonant three-photon ionization of sodium was studied carefully. Owing to the dynamic Stark shift of the atomic transition frequency, the angular distributions were modified with increasing intensity as different atomic states were tuned into and out of resonance with the laser frequency. These experimental and theoretical studies provided a good understanding of dynamical Stark effects.

In 1985 Matthias, Zoller, Elliott, Piltch, Smith, and Leuchs [1.30] reported their investigation of resonant three-photon ionization of barium to a structureless continuum via 6snd Rydberg states $19 \leq n \leq 30$. Their experiment showed that state mixing in the Rydberg states strongly affects the photoion and photoelectron yields as well as the angular distributions of photoelectrons.

In addition to those studies mentioned above, it is possible to obtain detailed information about phase interference from photoelectron angular distributions. In recent years a new type of interaction between an atomic system and a multi-frequency radiation field has attracted a lot of attention [1.31-1.36]. This new

type of interference represents another kind of interaction between an atomic system and a multi-frequency radiation field. The following processes are some examples: amplified spontaneous emission and four-wave mixing [1.37], multiphoton ionization and third-harmonic generation [1.38-1.40], multiphoton ionization and stimulated Raman scattering [1.41], two-photon absorption and two-photon resonant sum frequency generation [1.42].

Another interference interaction was reported as an example of this type of process [1.43, 1.44]. This process involves the interaction of third-harmonic generation and multiphoton ionization in which three-photon absorption and one-photon absorption are induced simultaneously. If the atom is allowed to interact with both the third-harmonic field and the fundamental field simultaneously, the atom can be excited to the upper state by a linear interaction or by a three-photon interaction. As a proper way to treat coherent processes, the total transition rate depends not only on the intensity of these two fields, but also on the interference of these two fields, i.e. the relative phase.

Elk, Lambropoulos, and Tang [1.45] investigated the theory of cancellation by interference between the absorption of three fundamental laser photons and one third-harmonic photon. In terms of the density matrix, and taking account of detuning, dephasing, and laser bandwidth, they explained how four-photon resonances can be canceled by a three-photon mechanism, if there is an atomic level at near three-photon resonance. The quantitative conditions for the existence of the effect were obtained. Their calculation showed that even for fairly large detunings, three-photon cancellation is responsible for the observed cancellation of four plus one resonantly enhanced multiphoton ionization peaks. At the same time, the results for focused beams will lead to a much more detailed understanding of the interplay between phase-matching, enhancement and cancellation.

Baranova, Chudinov, Shulginov, and Zel'dovich [1.46] studied interference of electrons ejected from a photomultiplier cathode. They found that the ionization rate depends not only on intensity but

also on the relative phase between the laser field E_ω and its second harmonic $E_{2\omega}$. Other interference phenomena between six-photon and seven-photon above threshold ionization were reported in 1990 by Muller, Bucksbaum, Schumacher, and Zaviyev [1.47]. Fairly large variations were found in their experimental study of multiphoton ionization of krypton, irradiated simultaneously by an infrared laser beam and its second harmonic. Neither of these experiments were sensitive to the total ionization rate, but rather measured the electron flux in the direction of polarization.

Photoelectron angular distributions provide a powerful tool to study the phase interference, but until now no research work of interference has been reported using this method. In this thesis we will discuss interference of photoionization angular distributions and report our experimental results. The studies in one- and two-photon ionization are very helpful to understand the phase interference interaction, and the data from those studies would be used to analyze the interference of angular distributions. From this processes much information about alkali atoms' structure would be determined.

1.2 Principles of photoelectron angular distributions

In studying photoelectron angular distributions we consider that the whole system consists of the isotropic atom and the incoming photons. The interaction is treated in the dipole approximation, and the photon has linear or circular polarization. Since the interaction of the photon and the atom has dipolar character, the total system has dipolar anisotropy, which is also displayed in the photoelectron angular distribution. Under the interaction of the atom and the photons, the angular distribution of the photoelectron is defined in terms of the angle Θ between polarization of the field and the direction of propagation of the ejected electron. In one-photon ionization we expect the angular distribution to have the form of $\cos^2\Theta$. In N-photon ionization processes, the Nth order dipole interaction with the photons leads to an angular distribution containing powers of $\cos\Theta$ to 2N. The physical interpretation is that in each absorption step the spatial anisotropy of the initially isotropic

atom can be increased because of the dipole character of the photon-atom interaction.

As a general situation, we consider an angular distribution for multi-photon ionization when the field is not resonant with any intermediate states. In resonant multi-photon ionization, the resonant intermediate states induce an anisotropy into the process which can make things complex. The angular distribution of the photoelectrons is proportional to the differential cross section of photoionization under the condition that the photon energy is less than a few electron Volts. To calculate the differential photoionization cross section, one evaluates the electric dipole matrix element for the transition from the initial ground state to the continuum state. For simplicity we neglect the effect of spin-orbit coupling and hyperfine coupling. We will consider these in chapters 3 and 4.

Another factor complicating the calculation of the photoelectron angular distribution is that the remaining ion may carry some of the anisotropy. This, however, does not apply to the ionization of alkali atoms with photons having an energy of a few electron Volts. The ground state of singly ionized alkali atoms is a $^1S_0$ state and the excited states of the ions lie so high in energy that they are not accessible by photoionization with visible laser light.

For a bound atom, the wave function is characterized by a principal, angular momentum and magnetic quantum numbers. In inversion symmetry the wave function can be expressed as the product of a radial and an angular part:

$$\Psi_{nlm}(\vec{r}) = R_{nl}(r)Y_{lm}(\theta,\phi), \qquad (1.1)$$

where $R_{nl}(r)$ is the radial factor and $Y_{lm}(\theta,\phi)$ is the spherical harmonic angular factor. The argument r of $R_{nl}(r)$ is the magnitude of the radius vector of the electron and θ,ϕ describes the direction of $\vec{r}$. The n, l, and m are the principal, angular and magnetic quantum numbers respectively.

The continuum state wave function is a superposition of an incoming spherical and an outgoing plane wave [1.48]:

$$\Psi_{\vec{k}}(\vec{r}) = \sum_{l'=0}^{\infty} i^{l'} e^{i\delta_{l'}} 4\pi G_{kl'}(r) \sum_{m=-l'}^{l'} Y_{l'm}(\Theta, \Phi) Y_{l'm}(\theta, \phi) \quad , \qquad (1.2)$$

where Θ and Φ describe the direction of the electron wave vector $\vec{k}$.

In the interaction of an atomic system with an electromagnetic field, we consider the total Hamiltonian as:

$$H = H^0 + H', \qquad (1.3)$$

where H^0 is the unperturbed atomic Hamiltonian, and H' is the interaction Hamiltonian between the atomic system and linearly polarized light which results in the emission and absorption of light by the atom. In the dipole approximation the interaction term for linearly polarized light is given by

$$H' = -e\vec{E} \cdot \vec{r} = -eE\, r \cos\theta, \qquad (1.4)$$

where $e\vec{r}$ is the dipole moment of the electron. The differential cross section is defined as the absolute square of the dipole matrix element:

$$\frac{d\sigma}{d\Omega} = \left| \left\langle \Psi_{\vec{k}}(\vec{r}) \right| r \cos\theta \left| \Psi_{nlm}(\vec{r}) \right\rangle \right|^2 . \qquad (1.5)$$

The corresponding selection rules are $\Delta l = \pm 1$. With these selection rules only two terms in the infinite sum in equation (1.5) that describes the continuum state have to be considered.

Then $d\sigma/d\Omega$ is the absolute square of the amplitude of two outgoing partial waves $l' = l + 1$ and $l' = l - 1$. The absolute square contains an interference term that depends on the difference of the corresponding scattering phases δ_{l+1}-δ_{l-1}. The information about the scattering phase is available only in the angular distribution [1.32].

When measuring the total cross section σ_{Tot}, the angular distribution has to be integrated over Θ and Φ. In this case, the interference term vanishes owing to the orthogonality of the spherical harmonics.

Considering equations (1.1) and (1.2) and neglecting the l-1 partial wave, (this simplification is useful for the purpose of determining the highest order of anisotropy to be expected for the angular distribution) one finds that the differential cross section can be expressed as:

$$\frac{d\sigma}{d\Omega} \approx \left|Y_{l+1,m}(\Theta,\Phi)\right|^2 \frac{(l+1)^2 - m^2}{(2l+1)(2l+3)} A_{l+1}^2, \qquad (1.6)$$

where

$$A_{l+1} = 4\pi \int_0^{\infty} dr \cdot r^3 G_{k,l+1}(r) R_{nl}(r) \qquad (1.7)$$

represents the radial factor. The angular part of electric dipole matrix element of the atom in equation (1.6) is found using the identity:

$$\int_0^{\pi} d\theta \sin\theta \int_0^{2\pi} d\phi \cos\theta\, Y^*_{l+1,m}(\theta,\phi) Y_{lm}(\theta,\phi) = \sqrt{\frac{(l+1)^2 - m^2}{(2l+1)(2l+3)}}. \qquad (1.8)$$

$\left|Y_K(\Theta,\Phi)\right|^2$ represents the angular distribution function of photoelectrons with Θ,Φ describing the direction of the ejected electrons.

If all magnetic sublevels, m, of the bound state are equally populated, $\frac{d\sigma}{d\Omega}$ of equation (1.6) has to be summed over m. Using the formula:

$$\sum_{m=-l}^{l} m^{2M} \left| Y_{lm}(\Theta, \Phi) \right|^2 = \sum_{j=0}^{M} a_j \sin^{2j}(\Theta) \qquad (1.9)$$

one obtains for the m-averaged angular distribution of equation (1.5) a constant plus $\sin^{2j}\Theta$ terms. The coefficients a_j in equation (1.9) can be calculated by differentiating the addition theorem for spherical harmonics with respect to Φ [1.48]. Following similar arguments, it can be shown that the general formula describing the photoelectron angular distribution for multi-photon ionization can be expressed as:

$$\frac{d\sigma_N}{d\Omega} = \frac{\sigma_{Tot}^{(N)}}{4\pi} \sum_{j=0}^{N} \beta_{2j} P_{2j}(\cos\Theta) \qquad (1.10)$$

The atom from an initially isotropic state may increase its anisotropy in each absorption of a photon by the interaction of the photon and atom.

In one-photon absorption (N=1), the above formula becomes:

$$\frac{d\sigma_1}{d\Omega} = \frac{\sigma_{Tot}^{(1)}}{4\pi}[1 + \beta P_2(\cos\Theta)], \qquad (1.11)$$

where $P_2(\cos\Theta)$ is the second order Legendre polynomial:

$$P_2(\cos\Theta) = \frac{1}{2}(3\cos^2\Theta - 1). \qquad (1.12)$$

The angular distribution can also be expressed as a power series in $\cos\Theta$,

$$\frac{d\sigma_1}{d\Omega} = A_1(1 + \alpha\cos^2\Theta), \qquad (1.13)$$

where:

$$A_1 = \frac{\sigma_{Tot}^{(1)}}{4\pi}\left(1 - \frac{\beta}{2}\right) \qquad (1.14)$$

$$\alpha = \frac{3\beta}{(2-\beta)}. \qquad (1.15)$$

In the case of two-photon absorption (N=2), we have the form:

$$\frac{d\sigma_2}{d\Omega} = \frac{\sigma_{Tot}^{(2)}}{4\pi}[1 + \beta_2 P_2(\cos\Theta) + \beta_4 P_4(\cos\Theta)], \qquad (1.16)$$

where the Legendre polynomial $P_4(\cos\Theta)$ is

$$P_4(\cos\Theta) = \frac{1}{8}(35\cos^4\Theta - 30\cos^2\Theta + 3). \qquad (1.17)$$

When expressed as a power series in $\cos\Theta$, the angular distribution for two-photon absorption is of the form:

$$\frac{d\sigma_2}{d\Omega} = A_2\left(1 + \alpha_2\cos^2\Theta + \alpha_4\cos^4\Theta\right), \qquad (1.18)$$

where the coefficient A_2, α_2, α_4 are

$$A_2 = \frac{\sigma_{Tot}^{(2)}}{4\pi}\left(1 - \frac{1}{2}\beta_2 + \frac{3}{8}\beta_4\right) \qquad (1.19)$$

$$\alpha_2 = \frac{12\beta_2 - 30\beta_4}{8 - 4\beta_2 + 3\beta_4} \qquad (1.20)$$

$$\alpha_4 = \frac{35\beta_4}{8 - 4\beta_2 + 3\beta_4} \qquad (1.21)$$

By measurement of photoelectron angular distributions, one may get the coefficients α, α_2 and α_4, or β, β_2 and β_4. From these data information about the atomic structure and atomic transitions may be obtained.

1.3 Scope of this thesis

The thesis is organized as follows. Some survey work related to photoelectron angular distributions by other researchers have been discussed in Chapter 1. Also fundamental formulas were introduced in this chapter.

Experimental setups and experimental methods are described in detail in Chapter 2. These include: the dye laser system and the optical system, the atomic beam generation apparatus, the signal analysis instrumentation and process, and the high vacuum system.

In Chapter 3 we will derive a mathematical expression for the one-photon ionization angular distribution under the influence of spin-orbit effects. The experimental results of measurements of photoelectron angular distributions of cesium and rubidium are presented here. Analysis of these results and comparison between our laboratory results and other authors' theoretical and experiment reports are also presented.

Chapter 4 is devoted to nonresonant two-photon ionization processes and their angular distributions. In this chapter we report the theoretical description of two-photon ionization, our experimental results, and the experimental result analysis.

In Chapter 5, the requirement and conditions which allow us to observe interference between one-photon and two-photon ionization are discussed in detail. The interference results are reported in this chapter. Further application of the interference processes are also discussed.

Conclusions for all these experimental investigations and theoretical discussions are presented in Chapter 6.

1.4 List of references

1.1 W. Bothe, "die Emissionsrichtung durch Rontgestrahlen Ausgeloster Photoelektronen", Z. Phys., Vol. 26, p. 59, (1924).

1.2 G. Wentzel, Z. Phys., "Zur die Richtungsverteilung der Photoelektronen", Vol. 40, p. 574, (1926).

1.3 G. Wentzel, Z. Phys, "Zur Theorie des Photoelektrischen Effekts", Vol. 41, p. 828, (1927).

1.4 H. A. Bethe, "Quanten Mechanik der Ein-und Zweielektronprobleme", in Handbuch der Physik, Bd. Springer, Berlin, (1933).

1.5 M. A. Chaffee, "The Angular Distribution of Photoelectrons Ejected by Polarized Ultraviolet Light in Potassium Vapor", Phys. Rev., Vol. 37, p. 1233, (1931).

1.6 J. Berkowitz and H. Ehrhardt, "Angular Distribution of Valence-Shell Photoelectrons", Phys. Lett., Vol. 21, p. 531, (1966).

1.7 H. B. Bebb, "Theory of Three-Photon Ionization of the Alkali Atoms", Phys. Rev. Vol. 153, p. 23, (1967).

1.8 W. Zernik, "Two-Photon Ionization of Atomic Hydrogen", Phys. Rev., Vol. 135, p. 135, (1964).

1.9 J. E. Rizzo and R. C. Klewe, "Optical Breakdown in Metal Vapours", Brit. J. Appl. Phys., Vol. 17, p. 1137, (1966).

1.10 T. Okuda, K. Kishi, and Sawada, "Two-Photon Ionization Process in Optical Breakdown of Cesium Vapor", Appl. Phys. Lett., Vol. 15, p. 181, (1969).

1.11 K. Kishi and T. Okuda, "Two-Photon Ionization of Alkali Metal Vapors by Ruby Laser", J. Phys. Soc. Japan, Vol. 31, p. 1289, (1971).

1.12 J. C. Tully, R. S. Berry, and B. J. Dalton, "Angular Distribution of Molecular Photoelectrons", Phys. Rev., Vol. 176, p. 95 (1968).

1.13 A. D. Buckingham, B. J. Orr, and J. M. Sichel, "Angular Distribution and Intensity in Molecular Photoelectron Spectroscopy", Phil. Trans. R. Soc. Lond. A Vol. 268, p. 95, (1970).

1.14 P. Lambropoulos, "Effect of Light Polarization on Multiphoton Ionization of Atoms", Phys. Rev. Lett., Vol. 28, p. 585, (1972).

1.15 P. Lambropoulos, "Multiphoton Ionization of One-Electron Atoms with Circularly Polarized Light", Phys. Rev. Lett., Vol. 29, p. 453, (1972).

1.16 S. Klarsfeld and A. Maquet, "Circular versus Linear Polarization in Multiphoton Ionization", Phys. Rev. Lett., Vol. 29, p. 79, (1972).

1.17 E. Arnous, S. Klarsfeld, and S. Wane, "Angular Distribution in Two-Quantum Atomic Photoeffect", Phys. Rev. A, Vol. 7, p. 1559, (1973).

1.18 V. L. Jacobs, "Theory of Atomic Photoionization Measurements", J. Phys. B: Atom. Molec. Phys., Vol. 5, P. 2257, (1972).

1.19 Dan Dill, "Resonances in Photoelectron Angular Distributions", Phys. Rev. A, Vol. 7, p. 1976, (1973).

1.20 S. Edelstein, M. Lambropoulos, J. A. Duncanson, and R. S. Berry, "Angular Distribution of Electrons from Two-Photon Ionization of Ti Atoms", Phys. Rev. A, Vol. 9, p. 2459, (1974).

1.21 G. Leuchs, S. J. Smith, E. Khawaja and H. Walther, "Quantum Beats Observed in Photonization", Opt. Commun., Vol. 31, p. 313, (1979).

1.22 H. Kaminski, J. Kessler, K. J. Kollath, "Photoionization of the 7^2P Excited States of Cesium", Phys. Rev. Lett. Vol. 45, p. 1161, (1981).

1.23 M. P. Strand, J. C. Hansen, R-L. Chen, and R. S. Berry, "Influence of Nuclear Spin on Angular Distribution and Polarization of Photoelectrons: Resonant Two-Photon Ionization of Na", Chem. Phys. Lett., Vol. 59, p. 205, (1978).

1.24 D. Feldmann and K. H. Welge, "Two- and Three-Photon Energy and Angular Distribution of Electrons", J. Phys. B, Atom. Molec. Phys., Vol. 15, p. 1651, (1983).

1.25 D. Feldmann, G. Otto, D. Petring, and K. H. Welge, "The Angular Distribution of Photoelectrons from the Three-Photon Ionisation of Xenon in the Region of Autoionising Resonances", J. Phys. B: Atom. Molec. Phys., Vol. 19, (1986).

1.26 S. N. Dixit, "Dynamics of the Ratio of Resonant Multiphoton Ionisation Probabilities for Circular and Linear Polarised Radiation", J. Phys. B, Atom. Molec. Phys., Vol. 14, p. L683, (1981).

1.27 P. Lambropoulos and P. Zoller, "Autoionizing States in Strong Laser Fields", Phys. Rev., Vol. A24, p. 379, (1981).

1.28 S. N. Dixit, P. Lambropoulos, "Theory of Photoelectron Angular Distributions in Resonant Multiphoton Ionization", Phys. Rev. A, Vol. 27, p. 861, (1983).

1.29 W. Ohnesorge, F. Diedrich, G. Leuchs, D. S. Elliott, and H. Walther, "Influence of the Dynamic Stark Effect on Photoelectron Angular Distribution in Multiphoton Ionization", Phys. Rev. A, Vol. 29, p. 1181, (1984).

1.30 E. Matthias, P. Zoller, D. S. Elliott, N. D. Piltch, S. J. Smith, and G. Leuchs, "Influence of Configuration Mixing in Intermediate States on Resonant Multiphoton Ionization", Phys. Rev. Lett., Vol. 50, p. 1914, (1983).

1.31 D. J. Jackson, J. J. Wynne and P. H. Kes, "Resonance Multiphoton Ionization: Interference effects due to Harmonic Generation", Phys. Rev. A, Vol. 28, p. 781, (1983).

1.32 M. G. Payne and W. R. Garrett, "Theory of the Effect of Third-Harmonic Generation on Three-Photon Resonantly Enhanced Multiphoton Ionization in Focused Beams", Phys. Rev. A, Vol. 28, p. 3409, (1983).

1.33 J. C. Miller and R. N. Compton, M. G. Payne, and W. W. Garrett, "Resonantly Enhanced Multiphoton Ionization and Third-Harmonic Generation in Xenon Gas", Phys. Rev. Lett., Vol. 45, p. 114, (1980).

1.34 R. N. Compton and J. C. Miller, "Two-Color Multiphoton Ionization of Xenon", J. Opt. Soc. Am. B, Vol. 2, p. 355, (1985).

1.35 D. Normand, J. Morellec, and J. Reif, "Resonant Multiphoton Ionization and Third-Harmonic Generation in Mercury Vapour", J. Phys. B: Atom. Molec. Phys., Vol. 16, p. L227, (1983).

1.36 J. H. Glownia and R. K. Sander, "Resonantly Enhanced Vacuum Ultraviolet Generation and Multiphoton Ionization in Carbon Monoxide Gas", Appl. Phys. Lett., Vol. 40, p. 648, (1982).

1.37 M. S. Malcuit, D. J. Gauthier, and R. W. Boyd, "Suppression of Amplified Spontaneous Emission by the Four-Wave Mixing Process", Phys. Rev. Lett., Vol. 55, p. 1086, (1985).

1.38 J. C. Miller and R. N. Compton, "Third-Harmonic Generation and Multiphoton Ionization in Rare Gases", Phys. Rev. A, Vol. 25, p. 2056, (1982).

1.39 Y. I. Geller and A. V. Shvabauskas, "Influence of Nonlinear Frequency Mixing on Multiphoton Ionization of Gases", Opt. Spectrosc. (USSR), Vol. 53, p. 227, (1982).

1.40 S. A. Bakhramov, I. G. Kirin, P. K. Khabibullaev, and N. Sh. Shaabdurakhmanova, "Influence of Multiphoton Ionization on Frequency Conversion in Alkali Metal Vapors", Sov. J. Quantum Electron., Vol. 12, p. 1557, (1982).

1.41 J. A. D. Stockdale, R. N. Compton, and A. Dodhy, "Laser-Induced Ionization and Stimuilated Electronic Raman Scattering in Cesium Vapor near the $np^2P_{3/2,1/2}$ (n=6,7,8,9) states", Multiphoton Processes, 4th International Conference, p. 266, edited by S. J. Smith, Boulder, (1987).

1.42 A. V. Smith, private communication.

1.43 C. Chen, Y-Y. Yin ,and D. S. Elliott, "Interference Between Optical Transitions", Phys. Rev. Lett., Vol. 64, p. 507, (1990).

1.44 C. Chen and D. S. Elliott, "Measurement of Optical Phase Variations Using Interfering Multiphoton Ionization Processes", Phys. Rev. Lett., Vol. 65, p. 1737, (1990).

1.45 M. Elk, P. Lambropoulos, and X. Tang, "Interference between Nonresonant Three-Photon Absorption and Third-Harmonic Generation and the Cancellation of Four-Photon Resonances", Phys. Rev. A, Vol. 44, p. R31, (1991).

1.46 N. B. Baranova, A. N. Chudinov, and B. Ya. Zel'dovich, "Polar Asymmetry of Photoionization by a Field with $\langle E^3 \rangle \neq 0$. Theory and Experiment", Opt. Comm., Vol. 79, p. 116, (1990).

1.47 H. G. Muller, P. H. Bucksbaum, D. W. Schumacher, and A. Lavriyev, "Above-Threshold Ionisation with a Two-Colour laser Field", J. Phys. B: Atom. Molec. Opt. Phys., Vol. 23, p. 1, (1990).

1.48 J. Cooper and R. N. Zare, In: Lectures on Thoretical Physics, vol.XIc, Atomic Collision Processes (eds. S. Geltman, K. Mahanthappa, W. Brittin), p. 317, New York: Gordon and Breach (1969).

CHAPTER 2
EXPERIMENTAL EQUIPMENT

2.1 Introduction

The major goal of this experiment is to measure the effect of interference between one-photon ionization and two-photon ionization on the photoelectron angular distribution. In the same time we have made precision measurements of these individual processes, in order to study fundamental atomic properties of rubidium and cesium. In this section we will describe the experimental setup for these measurements, which includes the dye laser system, the optical system, the high vacuum system, the photoelectron signal detection electronics, and the data analysis instrumentation.

In order to determine the photoelectron angular distributions over a wide range of photon energies, we used Nd:YAG-laser-pumped dye laser. The wavelengths of the fundamental laser fields used in these experiments were in the range from 550 to 628 nm and the second harmonic light was from 275 to 314 nm. Several different kinds of dye were used to obtain intense wavelength-variable dye laser output. A β-BaB_2O_4 (BBO) crystal were used to efficiently double the frequency of the laser output.

The photoelectron detection system was assembled by ourselves. It includes an electron lens, an electron multiplier, an electrical field shield, and three Helmholtz pairs of magnetic coils. Data analysis instrumentation and a mini-computer were used to analyze and record the photoelectron angular distribution signal.

A high vacuum chamber was required for these measurements in order to reduce the noise signal due to uv ionization of background gas and to reduce the probability of collisions of the atomic beam or

photoelectrons with air molecules. A differentially pumped system including a high speed cryopump, a diffusion pump, and a turbo-molecular pump were used to satisfy this requirement.

In this chapter, we are report the setup for the photoelectron angular distribution measurements of alkali metals and the interference experiment.

2.2 Dye laser system and optical system

The homemade dye laser system in this experiment is shown in figure 2.1. It consists of a tunable oscillator and three stages of amplification which are pumped by the second harmonic of a Nd:YAG laser. The Nd:YAG laser (Laser Photonics MY35) has maximum output of 1J per pulse at 1.06 μm with pulse to pulse stability of 2%. The repetition rate of the pulses used in our experiment was 10 Hz. Using a KDP crystal, one can get up to 350 mJ per pulse second-harmonic output at 532 nm. The pulse duration is 12-15 ns for second harmonic laser light. The energy stability (90% of the pulses) at 532 nm is $\pm$4%.

The dye oscillator is a Littman [2.1] type with longitudinal pumping. The purpose of using longitudinal pumping is to get good transverse mode structure. In a longitudinal pumping situation the excited area of the dye medium is round and uniform, providing favorable conditions for the production of a TEM_{00} transverse mode. The ratio of amplified spontaneous emission, which was produced by single-pass amplification with low gain, to total output was small. The laser cavity was very short ($\approx$5 cm) and the time averaged linewidth was narrow, so it was easy to keep this laser operating in a single longitudinal mode. This Littman laser provides a TEM_{00} mode and much more stable pulses than a conventional pulsed dye laser. All these characteristics make it an excellent laser oscillator.

Several dyes were used to obtain dye laser outputs in the range from 553 to 637 nm. For the wavelength range 553-571 nm rhodamine 6G dye in a methanol solution was used. The dye concentration was 2×10^{-4} molar for the oscillator and 0.8×10^{-4} molar for the amplifier. In this situation the peak output is at 560

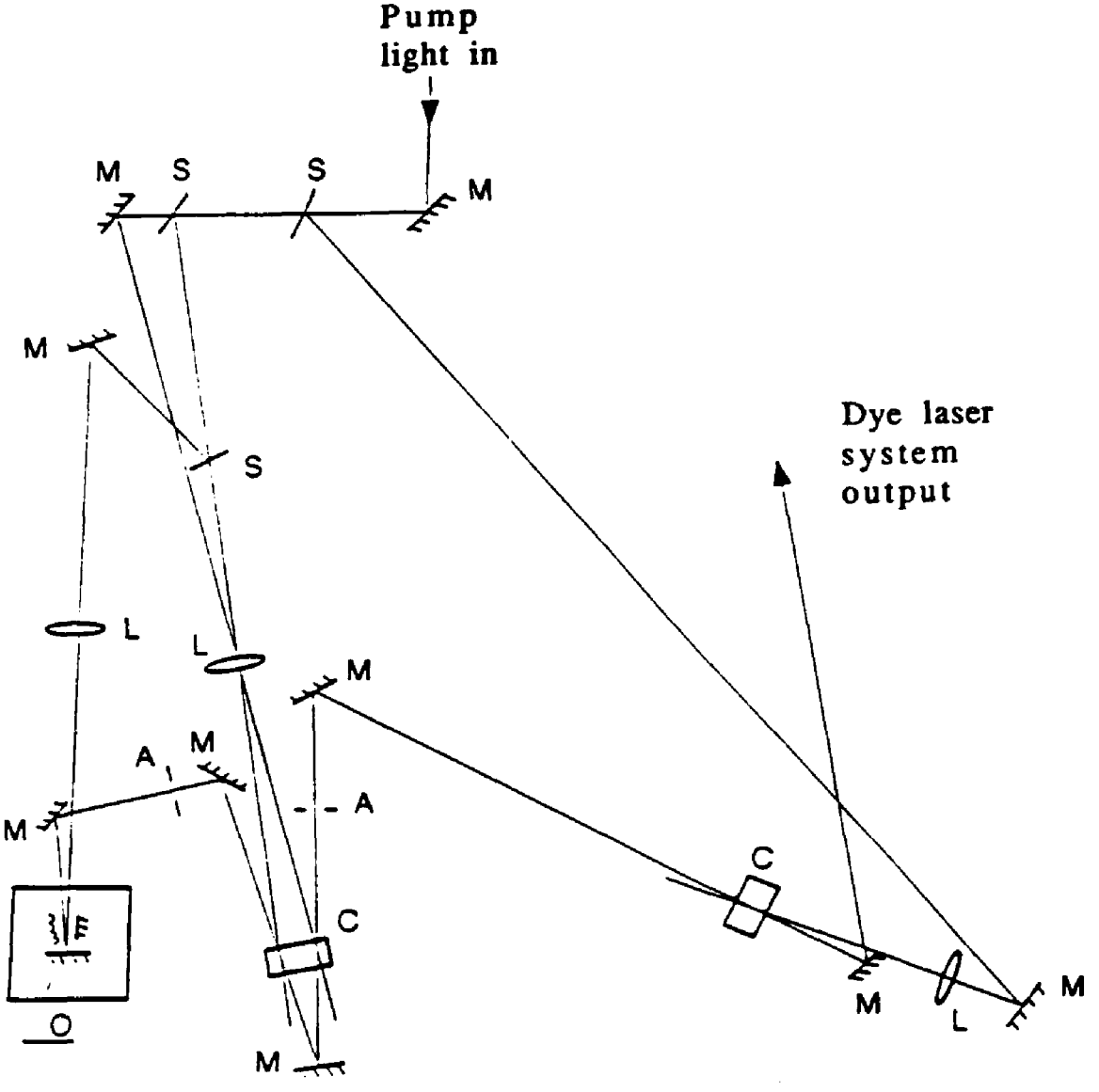

Figure 2.1 Dye laser system. (A) apertures, (C) dye cells, (L) lens, (M) mirrors, (O) Littman dye laser oscillator, (s) beam splitters.

nm, and the output at 565 nm falls down to one half that at the peak. With the 532 nm pump energy of 0.6 mJ per pulse, a 200 μJ TEM_{00} mode dye laser output was obtained. For laser wavelengths from 571 to 610 nm, the dye was rhodamine 610, also in methanol. The concentrations were 2×10^{-4} and 0.5×10^{-4} for oscillator and amplifier, respectively. For wavelengths from 610 to 628 the dye was rhodamine 640 in methanol, at a concentration of 1×10^{-4} and 0.5×10^{-4} respectively. For wavelengths from 628 to 637 nm we used DCM dye in ethyl alcohol. The concentrations were 4.4×10^{-4} and 1.1×10^{-4}.

The dye solution was pumped through a square quartz flow tube. We found that the vibration of the dye solution from the dye pump was one of the main factors causing laser intensity fluctuations and mode instability. In order to suppress this vibration, we installed an air muffler to absorb the vibration efficiently.

Three dye amplifier stages were used to amplify the light from the laser oscillator. These amplifiers were pumped by the same Nd: YAG laser. A temporal delay of about 3 ns between the pumping oscillator and first amplifier stage and between the neighboring amplifiers was introduced to match the arrival time of the dye and pump pulses. This delay is important because it not only increases the efficiency of amplification, but also reduces the loss of fluorescence in the amplifiers and the amplified spontaneous emission background. Before the first amplifier stage, a polarizer is fixed to keep the laser polarization in the vertical direction and ensure the linearity of polarization. The amplifiers are longitudinally-pumped flow dye laser cells having 1.5 inch diameter apertures, 1 cm inside thickness and Brewster-angled windows to reduce the reflection losses. In order to save space and optical components, the first and second stages of amplifiers are set in the same dye cell. Two apertures are installed, one between the oscillator and the first amplifier, and another between the second and third amplifiers, to maintain good mode structure and beam uniformity.

In our experiment, the laser energy is distributed such that the first stage pump has an energy of 6.5 mJ/pulse, the second stage has 65 mJ/pulse, and the third stage has 168 mJ/pulse. After three stages of amplifiers the maximum output energy at 560 nm is 60 mJ per pulse at the pump energy of 240 mJ per pulse. By blocking the pumping beam of the oscillator we found that the amplified spontaneous emission is so weak that we can disregard it safely.

The optical system and the photoelectron detection system are shown in figure 2.2. A high quality polarizer (type: air-spaced polarizer, Glan-Foucault) is inserted after the last stage of the amplifier to ensure the linearity of the laser beam polarization to better than 1000:1. In order to get a tunable ultraviolet laser beam in the range from 275 nm to 285 nm, the dye laser beam is focused by a 100 cm focal length lens into a β-BaB_2O_4 frequency-doubling crystal [2.2, 2.3]. This crystal has a 48° cut angle and a high damage threshold of 5 GW/cm^2. By rotating the BBO crystal it is not difficult to get phase matching for the wavelength range from 540 to 630 nm. Proper laser focussing is important to get high second-harmonic output, and at the same time prevent damage of the crystal. After the β-BaB_2O_4 crystal we put a uv filter to block the fundamental laser beam.

A half wave Fresnel rhomb was chosen to rotate the polarization direction of laser beam, because of its wide wavelength range. All the optical elements must have good optical surfaces and excellent flatness to minimize the laser light wave front distortion. This is especially important for interference experiment. In fact, wavefront distortion limits for the interference experiment were so restrictive that we chose not to rotate the light polarization for these measurements. We will discuss the measurement technique for the interference work in more detail in Chapter 5.

2.3 Generation of atomic beam of alkali metal and detection of photoelectrons

In this experiment a reasonably dense, well-collimated rubidium atomic beam is required. A detailed construction diagram of the

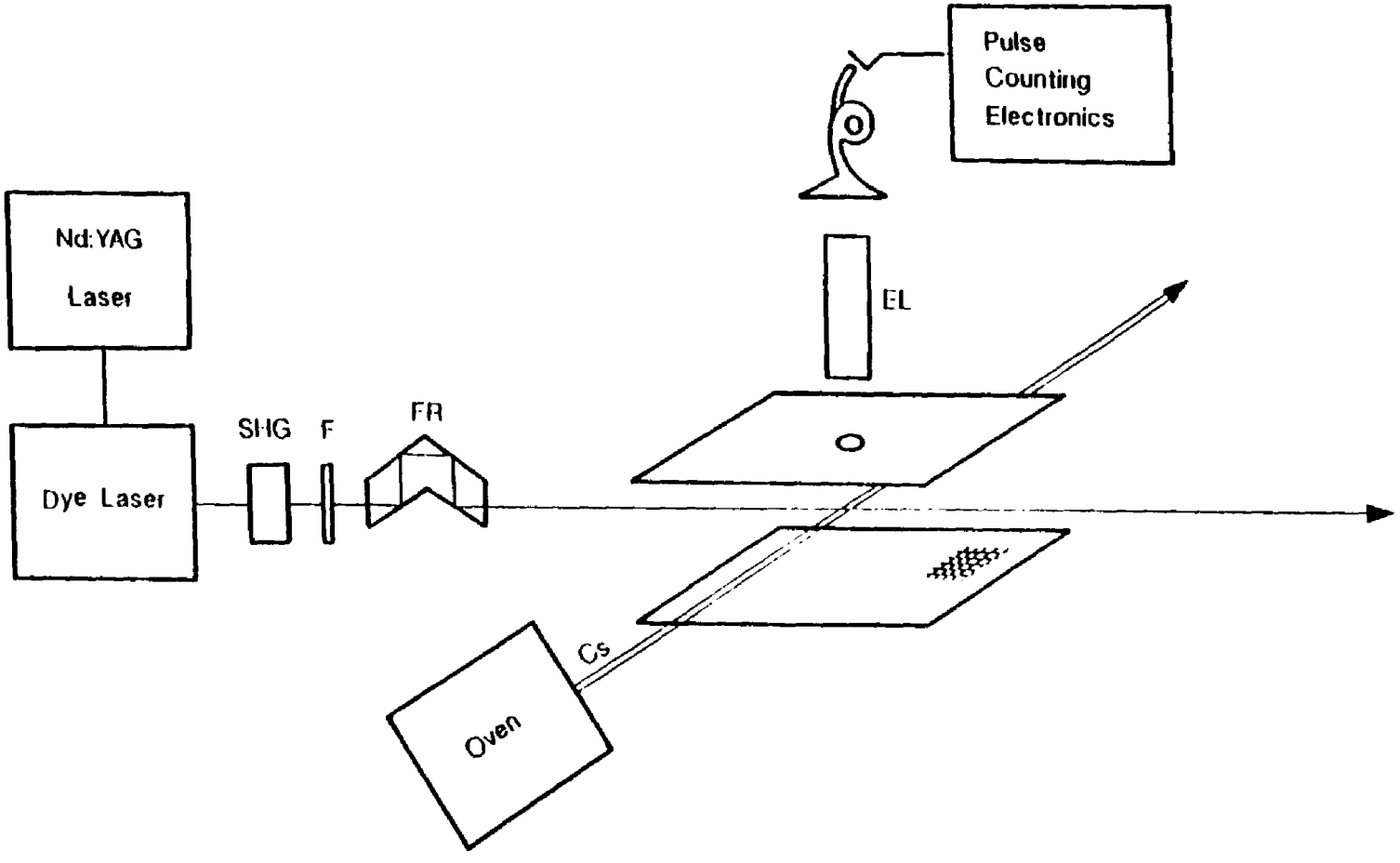

Figure 2.2 Optical systems and the photoelectron detection system. SHG: β-BaB_2O_4 crystal for second harmonic generation, F: uv filter, FR: Fresnel rhomb, EL: electron lens.

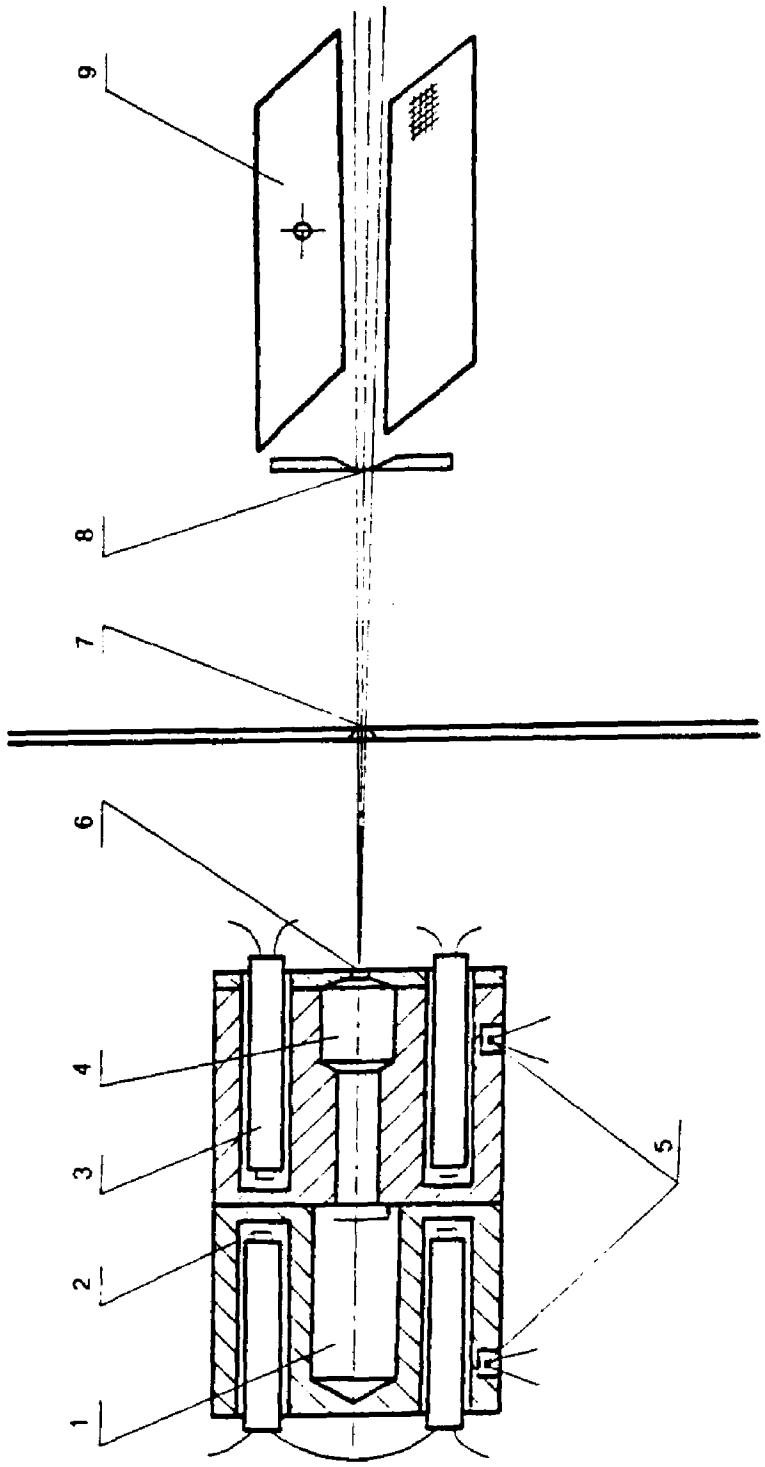

Figure 2.3 Interaction region and the generation of atomic beam. (1) oven, (2) heater, (3) ceremic isolator, (4) nozzle, (5) thermal couple, (6, 7, 8) aperture, (9) electrical shield planes.

two-stage oven is shown in figure 2.3. The oven is a combination of two parts: a reservoir of alkali-metals and a nozzle. The cylindrical reservoir is used to produce an alkali-metal vapor and has four heating cavities. The heaters are made of Nichrome wire, which is passed through ceramic tubes with four holes. All heaters are inserted in turn into the cavities for convenient assembly and efficiency. A nozzle is used to dissociate the alkali dimers. Under the tube of the nozzle a baffle is used to prevent lumps of alkali metal from entering the nozzle tube. Four similar but longer heaters are inserted into nozzle body to heat the nozzle. This requires a higher temperature than the oven. Both oven and nozzle bodies are made of stainless steel.

The nozzle is necessary for an alkali atomic vapor, because of the large number of alkali dimers produced in an effusive oven [2.4-2.7]. When the temperature of the oven increases, the dimer density in alkali vapors in thermal equilibrium with liquid increases very strongly. The dimers will dissociate if they undergo collisions in a relatively hot area, so the nozzle tube is long and thin. This nozzle must be separated from the oven reservoir, so that the vapor in the hot dissociating nozzle area is isolated from the equilibrated liquid-vapor region. The nozzle tube has a circular cross section, and its size and length is carefully chosen to dissolve as many dimers as possible. When the dimers pass through the tube, they may undergo many wall collisions but few gas collisions. Therefore, the vapor in the nozzle is not in a thermal equilibrium state as it is in the vapor-liquid equilibrium system of the oven.

The ratio of the dimer density to atom density can be expressed roughly as [2.8]:

$$K_p = \frac{P_{mol}}{P_{atom}^{\ 2}}, \qquad (2.1)$$

where P_{mol} and P_{atom} are the partial pressures of the dimer and atom of alkali separately. In equilibrium, if no processes other than dimer

to atom conversion are present, K_p only depends on the temperature of the oven.

Two thermocouples inserted into holes drilled in the oven and nozzle bodies are used to measure the temperature of the oven and nozzle separately. In our experiment a heater power of 15W is typically required to operate the oven at a temperature of about 160°C. The temperature of nozzle is 190 °C, which requires about 20W power.

Two apertures with diameter 1 mm form an atomic beam collimating system (figure 2.3). The distance from oven to second aperture is 280 mm. The first aperture separates the two differentially pumped chambers of the vacuum system, and prevents most of the atomic vapor from entering the interaction area. This reduces the metal atom vapor concentration efficiently in the interaction area. This extra metal vapor is one of the most important contributions to the background noise. The crossing angle between the atomic beam and the laser beam is 108°.

The intensity flow of the atomic beam or the number of molecules in the interaction area per second is [2.9]

$$I = \frac{1}{4\pi}\frac{A_d}{l_0^2} n \bar{v} A_s g \quad , \qquad (2.2)$$

where A_d is the area of the interaction region. The interaction region is defined by the intersection of the atomic beam and the laser beam which has a diameter of approximately 1 mm. l_0 is the length of the apparatus from source to detector, $\bar{v}$ is the average speed of the atoms in the oven, A_S is the output area of the vapor in oven, n is the density of atoms in the oven, and g is a geometrical coupling factor. The geometrical coupling factor g depends on the aperture areas and length of the oven and nozzle. By simple calculation, the intensity in the interaction area is 2.2×10^9 atoms/second, yielding a density of atoms at 7.4×10^6 atoms/cm^3.

The collimated atomic beam travels between a pair of electrically grounded parallel plates separated by 2.75 cm which shield the interaction region from outside electric fields. In order to cancel the earth's magnetic field in the interaction region, three pairs of Helmholtz magnetic coils with diameter 900 mm are installed outside the vacuum system. The currents of the coils are carefully adjusted to assure that the total magnetic field is less than 10 mG in the interaction area. The lower ground plate is constructed of a fine stainless steel mesh (82% transmitting, 50 threads per cm), so that the interaction area can be efficiently shielded and at the same time the scattered alkali-metal atoms may be evacuated from interaction area. The upper plate has a 2.2 mm aperture, through which the measured photoelectrons pass. The size of this aperture and that of the interaction region define the angular resolution of our measurement, which we estimate to be approximately 10 degrees.

The detector consists of an electron lens and a channel electron multiplier which are mounted above the aperture. The electron lens is constructed from a pair of aluminum cylindrical rings with the inside diameter of 14.2 mm and height of 34.1 mm. The gap between two cylinders is 1.1 mm. These two cylinders have bias voltages of 10 V and 60 V, respectively. For this size and bias voltage, the focal point is calculated to be 23 mm behind the rear cylinder. A channel electron multiplier (type: CDEM, #407N) was installed just at this position. A voltage of 1800-2300 Volts is used to get a gain of about 5×10^6. At this gain an electron may produce a 2-5 mV pulse into 50 Ω load. A 100 pF capacitor was used to connect the output pulse to the pre-amplifier and isolate the high voltage. A stainless steel box is used to shield the electron lens and channel electron multiplier to prevent scattered electrons from entering the electron multiplier. Because of the high voltage of the channel electron multiplier the shield must be very tight. The background noise can thus be reduced dramatically. For laser wavelengths from 275 to 314 nm the background noise is less than ten electrons for

600 laser shots, and for laser wavelength from 553 to 628 the background noise is less than one electron per 600 laser shots.

2.4 Signal analysis of the photoelectron angular distributions

A diagram of the signal amplification and analysis instrumentation is shown in figure 2.4.

The photoelectron signal produced by the channel electron multiplier is very weak, in general, only 2-5 mV. A pre-amplifier consisting of 2-3 stages ($\times$10/stage) was set to amplify the signal to approximately 1 Volt.

A fraction of the electron pulses are unfortunately due to noise rather than ionization of the rubidium in the atom beam. One source of noise is related to the reflections from the two vacuum chamber windows. When this scattered light hits metallic materials within the chamber or air molecules or alkali-metal atoms, it may produce many photoelectrons which can be detected by the electron detector. Another source of noise is the alkali metal vapor accumulated on the chamber components. Because the alkali atom has a very low ionization potential, even low concentrations of alkali vapors may produce strong background noise levels.

In order to reduce the influence of these noise pulses a gated electronics system is used. Most noise pulses appear later than the real photoelectron signals because they have longer optical and electron paths. A trigger signal derived from the Nd:YAG laser Pockels cell is used to trigger the gate source and produce a variable width gate signal. The gate signal is delayed by a variable delay line and applied to the linear gate. The position of the gate is adjusted to match the photoelectron signal, and the width of the gate is set to 30 ns. After careful adjustment the background noise may be reduced to the minimal levels quoted above. Finally, the photoelectron signal is sent to a scalar and a mini-computer for accumulation of the data.

The laser intensity is monitored by a photodiode. A pulse integrator receives the electrical signal from photodiode, integrates it and sends the results to the computer for analysis. If the intensity of

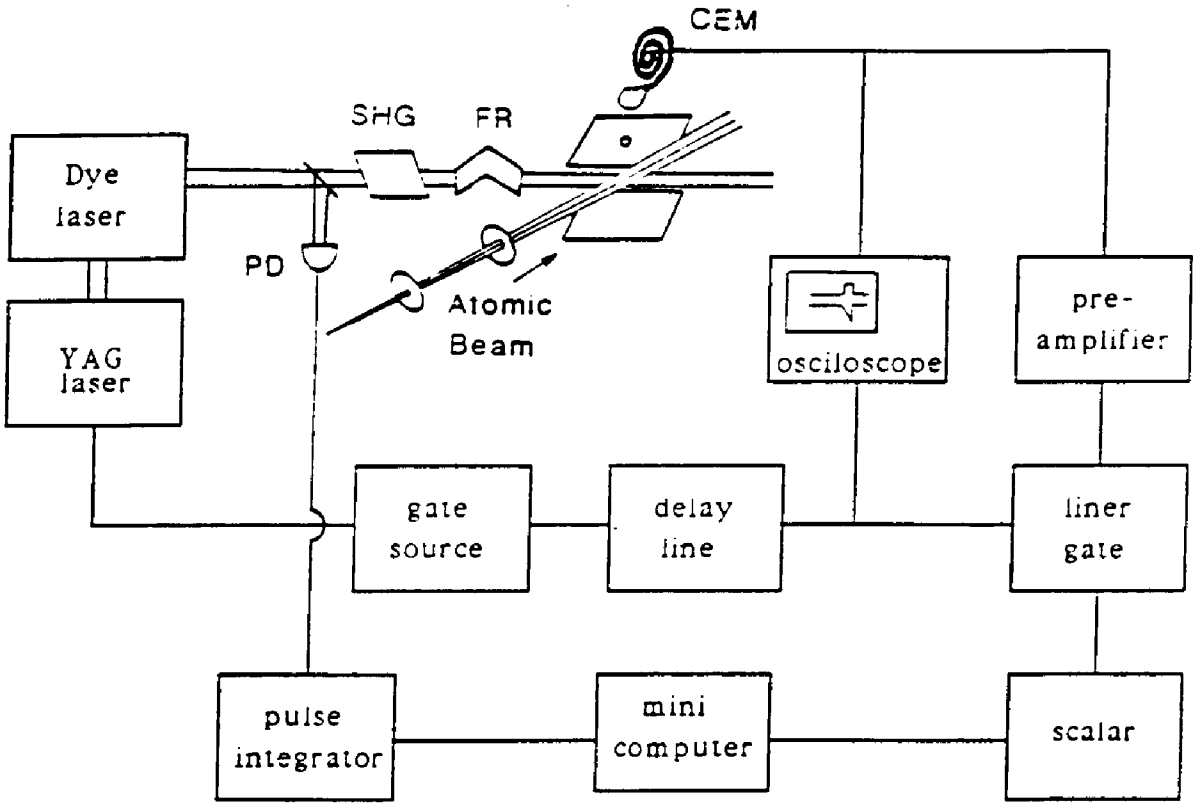

Figure 2.4 Diagram of signal analysis system.

the dye laser is out of range (too strong or too weak), the photoelectron signal to that shot will be discounted. This intensity range must be set properly. If this range is too large, the laser intensity variations will influence the precision of the measured photoelectron signal. If the range is too small, too many laser shots will be out of range, increasing the measurement time and the experiment instability. Typical window size is ±5% of the average laser power.

2.5 Vacuum system establishment and inspection

The oven, nozzle, interaction area, and the photoelectron detection system are housed inside the high vacuum system. The schematic of the vacuum system is shown in figure 2.5. It consists of a high vacuum chamber, a cryopump, a turbo-molecular pump, a diffusion pump and a cold trap. The vacuum chamber is the critical part in which the interaction region and the photoelectron detector are mounted. A cryopump (type: CSA-102, pump speed: 1500 liter/second) is mounted just under the interaction area, so the alkali metal atoms may be evacuated efficiently. There are two reason for us to choose a cryopump. One reason is that the cryopump can condense the alkali metal atoms much better than other kinds of pumps. The second reason is that cryopump prevents deposits of oil vapor on the mesh and plane, which would cause the electrical potentials and influence the measurement of results. A turbo-molecular pump (type: Turb-V80, pump speed: 75 liter/second) is mounted opposite to the atomic beam, so that the atomic beam, passing though the chamber, may be pumped out immediately. Using these two pumps simultaneously, a high vacuum degree of 1×10^{-8} torr is achieved.

The oven chamber is installed in a separate chamber of the system, which is pumped by a 4" diffusion pump (type: CVI, PMCS-4B, pump speed: 700 liter/second). These two chambers are separated, and only a 1 mm diameter hole connects them. This prevents most alkali metal atoms from entering the interaction

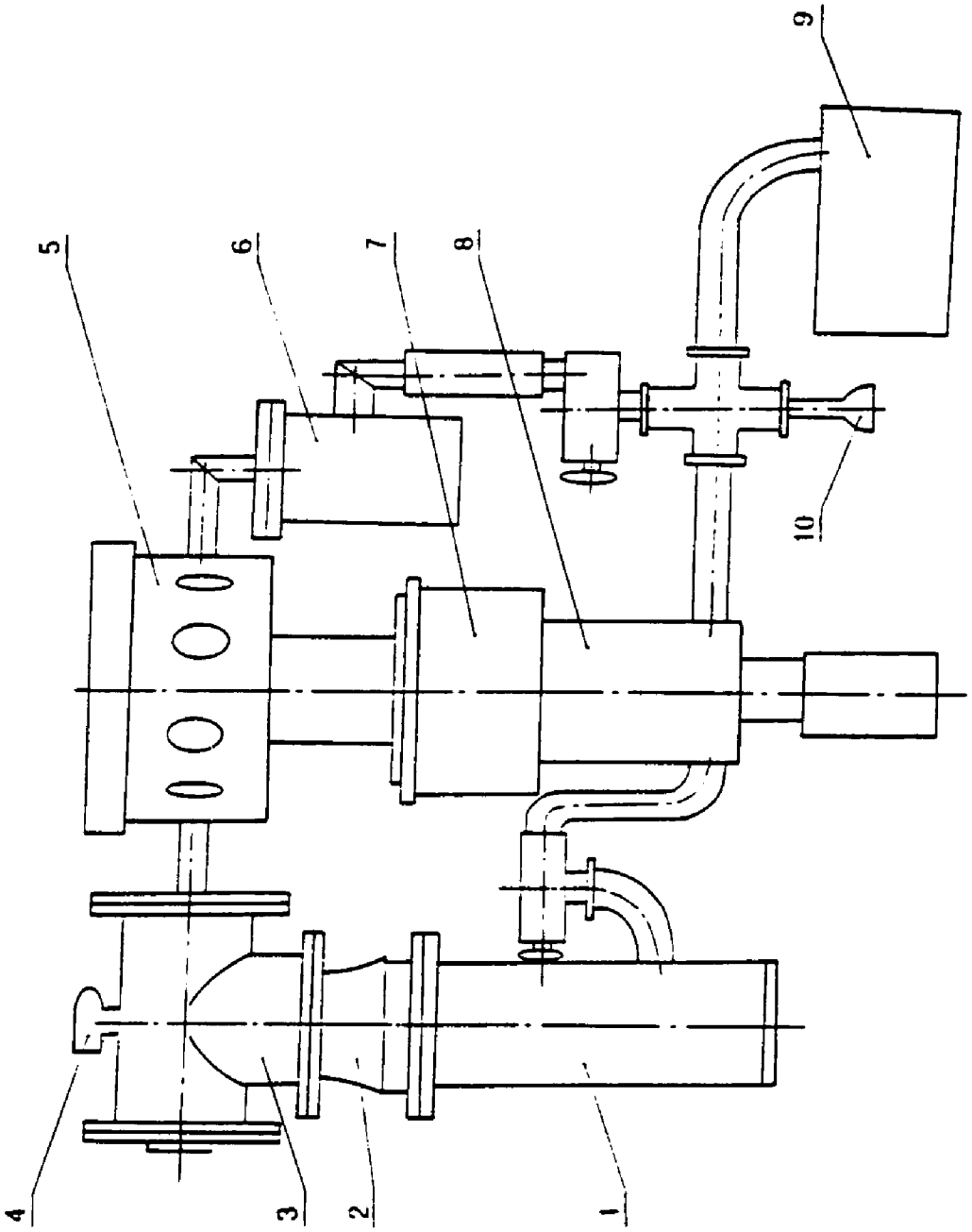

Figure 2.5 Vacuum system. (1) diffusion pump, (2) cold trap, (3) oven cavity, (4) ion gauge, (5) vacuum chamber, (6) turbo-molecular pump, (7) valve, (8) cryopump, (9) mechanical pump, (10) thermocouple gauge.

chamber and keeps the chamber clear. The oven cell pressure is typically 2×10^{-7} torr.

2.6 List of references

2.1 M. G. Littman, "Single-Mode Pulsed Tunable Dye Laser", Appl. Opt., Vol. 23, p. 4465, (1984).

2.2 K. Kato, "Second-Harmonic Generation to 2048 Å in β-BaB_2O_4", IEEE J. Q. E., Vol. QE-12, p. 1176, (1976).

2.3 J. T. Lin and C. Chen, "Choosing a Nonlinear Crystal", Lasers & Optronics, November, P. 59, (1987).

2.4 M. Lambropoulos and S. E. Moody, "Design of a Three Stage Alkali Beam Source", Rev. Sci. Instrum., Vol. 48, p 131, (1977).

2.5 G. M. Carter and D. E. Pritchard, "Recirculating Atomic Beam Oven", Rev. Sci. Instrum., Vol. 49, p. 120, (1978).

2.6 G. J. Witteveen, "Low-Consumption Atomic Beam Source", Rev. Sci. Instrum., Vol. 48, p 1131, (1977).

2.7 G. S. Tompa, J. L. Lopes, and G. Wohlrab, "Compact Efficient Modular Cesium Atomic Beam Oven", Rev. Sci. Instrum., Vol. 58, p 1537, (1978).

2.8 T. F. Hill, "Introduction to Statistical Thermodynamics", (1960).

2.9 N. F. Ramsey, "Molecular Beams", p. 11-19, published by Oxford University, (1985).

CHAPTER 3
PHOTOELECTRON ANGULAR DISTRIBUTIONS FOR ONE-PHOTON IONIZATION: SPIN-ORBIT EFFECT

3.1 Introduction

The spin-orbit interaction has a variety of effects on optical transitions in the alkali metal atoms. In 1930, Fermi [3.1] first indicated that the spin-orbit perturbation of the alkali wave functions was responsible for the anomalous doublet line-strength ratio of discrete P states. Fermi used perturbation theory to show that the spin-orbit interaction is repulsive in the $j=\frac{3}{2}$ state and attractive in the $j=\frac{1}{2}$ state, thus leading to differences between the $P_{3/2}$ and $P_{1/2}$ radial wave function for the excited electron. Seaton [3.2] in 1951 calculated atomic photoionization cross sections of the alkali metals. He showed that the spin-orbit interaction in the continuum state shifts the Cooper minimum for the $\varepsilon P_{3/2}$ and $\varepsilon P_{1/2}$ states, resulting in a non-zero minimum of the photoionization cross section.

Fano [3.3 3.4] in 1969 predicted theoretically that the spin-orbit coupling in atoms results in an important and interesting property of ejected electrons, i.e. that polarized electrons would result from photoionzation of unpolarized atoms by circularly polarized photons. This may be revealed by examining the difference between the radial matrix elements for the $j=\frac{1}{2}$ and $j=\frac{3}{2}$ continuum for an electric dipole transition from the ground state to P-state continuum. The perturbed radial matrix elements are $R_{1/2}=R(\varepsilon,\frac{1}{2})$ and

$R_{3/2}=R(\varepsilon,\frac{3}{2})$, which correspond to $j=\frac{1}{2}$ and $j=\frac{3}{2}$, respectively. In order to compare the various spin-orbit effects of alkali atoms for a wide range of wavelengths of light, a perturbation parameter $x(\varepsilon)$ was introduced to describe the perturbation of the spin-orbit interaction. $x(\varepsilon)=\frac{2R_{3/2}+R_{1/2}}{R_{3/2}-R_{1/2}}$, serves as the main parameter that characterizes the asymmetry in the radial matrix elements. A series of experiments were done to verify the Fano effect [3.5-3.8]. Fano suggested the measurement of $P(\varepsilon)$ which is an energy dependent polarization parameter. The $P(\varepsilon)$ averaged over all directions of photoelectron emission can be expressed in terms of perturbation parameter $x(\varepsilon)$ as $P(\varepsilon)=\frac{(2x+1)+4(x+1)(x-2)(1-\cos\delta)/9}{x^2+2}$, where δ is the phase difference between $\varepsilon P_{3/2}$ and $\varepsilon P_{1/2}$ states.

Another important polarization parameter, $Q(\varepsilon)$, which was measured by Baum, Lubell, and Raith [3.6, 3.9], is related to the perturbation function $x(\varepsilon)$. This polarization parameter $Q(\varepsilon)$ is obtained by measurement of the ion counting-rate asymmetry $\Delta=\frac{I^+-I^-}{I^++I^-}$, where I^+ and I^- are the counting rates corresponding to the left- and the right-circular photon polarization, respectively. The ion counting-rate Δ is given as $\Delta=Q(\varepsilon)P_{ph}P_{at}$ where P_{ph} is the circle polarization and P_{at} is the electronic polarization of the atom. This polarization parameter $Q(\varepsilon)$ can be expressed in terms of $x(\varepsilon)$ by $Q(\varepsilon)=\frac{2x-1}{x^2+2}$.

A measurement was performed by Baum *et al.* who used a mercury arc lamp as a light source. A polarization filter and a quarter wave plate transferred the light to right or left-circularly polarized light. A polarized atomic beam was obtained by an oven and a permanent six-pole magnet. Three different alkali atoms, potassium, rubidium, and cesium, were measured.

The best of semi-empirical calculations are those of Weisheit [3.10] and Norcross [3.11], who achieved very close agreement with experiment. Considering the various spin-orbit effects based Fano's analysis and the effects of core polarization, they calculated the dipole transition moment and obtained the asymmetry of the oscillator strengths for bound state transitions, photoionization cross sections, and spin orientation of photoelectrons.

The spin-orbit effect has a great influence on photoelectron angular distributions. In equation (1.9) of chapter 1, the photoelectron angular distribution of one-photon absorption depends on only two dynamical parameters: the total photoionization cross section σ_{Tot} which determines the intensity of the photoelectrons, and the asymmetry parameter β [3.12, 3.13, 1.18] which determines the angular distribution of photoelectrons. In general, the σ_{Tot} depends on the photon energy; however, β is expressed theoretically as a ratio which is independent of energy, when the scattering process under study has only a single allowed final-state channel due to geometrical considerations.

Of course such energy-independence never occurs in reality due to the existence of different channels and their couplings. We may expect that the deviation of β from the predicted constant value will provide information of additional channels and their coupling strengths. In one-photon ionization from the single S-subshell to an εP final state channel, the photoelectron angular distribution parameter β will equal two and will be independent of the energy of the incident photon if spin-orbit effects are not important. But a number of experiments and theoretical studies have found that the parameter β for S $\rightarrow$P transition is not always a constant value two.

Cooper and Zare [1.18, 3.14] proved that the angular distribution of photoelectrons ejected in an electric dipole process can be expressed as:

$$\frac{d\sigma}{d\Omega} = \frac{\sigma_{Tot}}{4\pi}\left(1 + \frac{\beta}{2}\left(\frac{3}{2}\sin^2\Theta - 1\right)\right), \qquad (3.1)$$

where β is the asymmetry parameter and Θ is the angle between the momentum direction of the ejected electron and the polarization of light. β depends on the two radial dipole matrix elements R_{l-1} and R_{l+1}, corresponding to the two possible electron partial waves of angular momentum l-1 and l+1. Another factor which influences the β value is the relative phase difference $\delta=\delta_{l+1}-\delta_{l-1}$ of these two partial waves. Obviously β is dependent on incident photon energy ε:

$$\beta(\varepsilon)=\frac{l(l-1)R_{l-1}^2+(l+1)(l+2)R_{l+1}^2-6l(l+1)R_{l-1}R_{l-1}\cos\delta}{(2l+1)[lR_{l-1}^2+(l+1)R_{l+1}^2]} \qquad (3.2)$$

where R is a radial matrix element:

$$R_{l+1}=\int_0^\infty dr\Psi\left(\varepsilon p\frac{1}{2},r\right)r\Psi\left(n s\frac{1}{2},r\right) \qquad (3.3)$$

and δ is the phase shift difference associated with the asymptotic wave functions of the continuum states, $\delta=\delta_{l+1}-\delta_{l-1}$.

In a closed-shell system the situation is somewhat simpler, because the electrostatic interactions are spherically symmetric. Thus it would seem that for s electrons, the photoelectron angular distribution should be independent of energy. If only the nonrelativistic Hamiltonian is considered, this is indeed the case. The inclusion of relativistic interactions, however, deviates this point of view since the spin-orbit interaction is inherently anisotropic. For example, the photoionization of the outer s electron in an alkali-metal atom can go via $S\rightarrow P_{1/2}$ or $S\rightarrow P_{3/2}$ transitions. Thus the alternate channels allow for an interference. The alkali metals, therefore, offer an excellent case for the study of anisotropic interactions due to the spin-orbit effect since the core is $^1S_0$ and entirely spherical. There were a series of theoretical calculations about alkali atom photoionization [3.11, 3.12, 3.15-3.22].

These anisotropic effects are also in evidence in the noble gases, but the situation is far more complicated in the noble gases owing to the extensive interchannel coupling present. The importance of spin-orbit interactions for the 5s subshell of xenon has been predicted earlier by Walker and Waber [3.23], who presented a theoretical calculation in jj coupling using Dirac-Slater wave functions. The β parameter was predicted to be nearly 0.9 at threshold, to increase rapidly to 1.5 at an energy 13.6 eV above threshold, and thereafter to rise slowly toward the value 2.0 at an energy 81.6 eV above threshold. Ong and Manson [3.24, 3.25] used Dirac-Fock wave functions to calculate photoelectron angular distributions and obtained results similar to those of Walker and Waber. Johnson and Cheng [3.26, 3.27] have carried out the most detailed calculation of the $5S \rightarrow \varepsilon P$ photoionization of Xenon. They found theoretically that under suitable conditions, the relativistic corrections to the interaction of a photoelectron with its parent ion are enhanced and large anisotropic final state effects appear, so the angular asymmetry parameter is reduced by a factor of 9 from its nonrelativistic value of two near the Cooper minimum. They predict a minimum value of β for Xenon of about zero near the minimum in the 5S cross section. Other theoretical calculations include Huang and Starace [3.28].

On the experimental side, Dehmer and Dill's measurement [3.29] of the angular distribution asymmetry parameter β for the 5S subshell of xenon was a striking demonstration of the importance of relativistic interactions to photoabsorption processes. Other work includes White *et al.* [3.30] who used three different photon energies (26.8, 30 and 32 eV) to prove that the asymmetry parameter β is different from the nonrelativistic value of two, particularly near the Cooper minimum.

Recently, Cuellar *et al.* [3.31] reported measurements of photoelectron angular distributions for resonantly enhanced three-photon ionization of cesium via the excited ns (n=8-12) states. The intermediate state, ns $^2S_{1/2}$, was selected by tuning the wavelength of the dye laser output. Since the ns $^2S_{1/2}$ state was isotropically populated by the linearly polarized laser, the problem is essentially

reduced to a single-photon ionization of the excited s-state, with one data point per s-state. Since the photo-electron energy is near the Cooper minimum in each of these cases, β shows a strong wavelength dependence.

3.2 Principle of the photoelectron angular distribution for one-photon absorption with spin-orbit interaction

The alkali atoms are especially attractive for the investigation of photoionization processes. The alkali atoms' ionization potentials are small, so that only one ultraviolet photon or two visible photons are sufficient to ionize the atoms. Therefore, the second harmonic of a visible laser can be used for the experiment which makes it possible to investigate the wavelength dependence of the photoionization cross sections and angular distributions. In addition, because of the simplicity of the alkali metal energy level scheme, the theoretical understanding and interpretation of the experiment results are relatively easier than for other more complex atoms. The energy level diagram (figure 3.1) shows the transition from ground S-state to $P_{3/2}$ and $P_{1/2}$ continuum states.

As mentioned in Chapter 1 the angular distribution may be expressed as:

$$\frac{d\sigma}{d\Omega} = \left| \left\langle \Psi_R(\vec{r}) \right| r \cos\theta \left| \Psi_{nlm}(\vec{r}) \right\rangle \right|^2 . \qquad (1.6)$$

The matrix element represents a transition of the atom from the 5S ground state to the P-continuum states through the absorption of a single photon.

Obviously spin-orbit coupling is absent in the initial S-state because its orbital momentum quantum number equals zero. However, spin-orbit coupling in the continuum leads to degenerate eigenstates with $j=\frac{1}{2}$ and $j=\frac{3}{2}$. The dipole selection rules for an optical transition with linearly polarized light are:

$$\Delta l = \pm 1 \qquad (3.4)$$

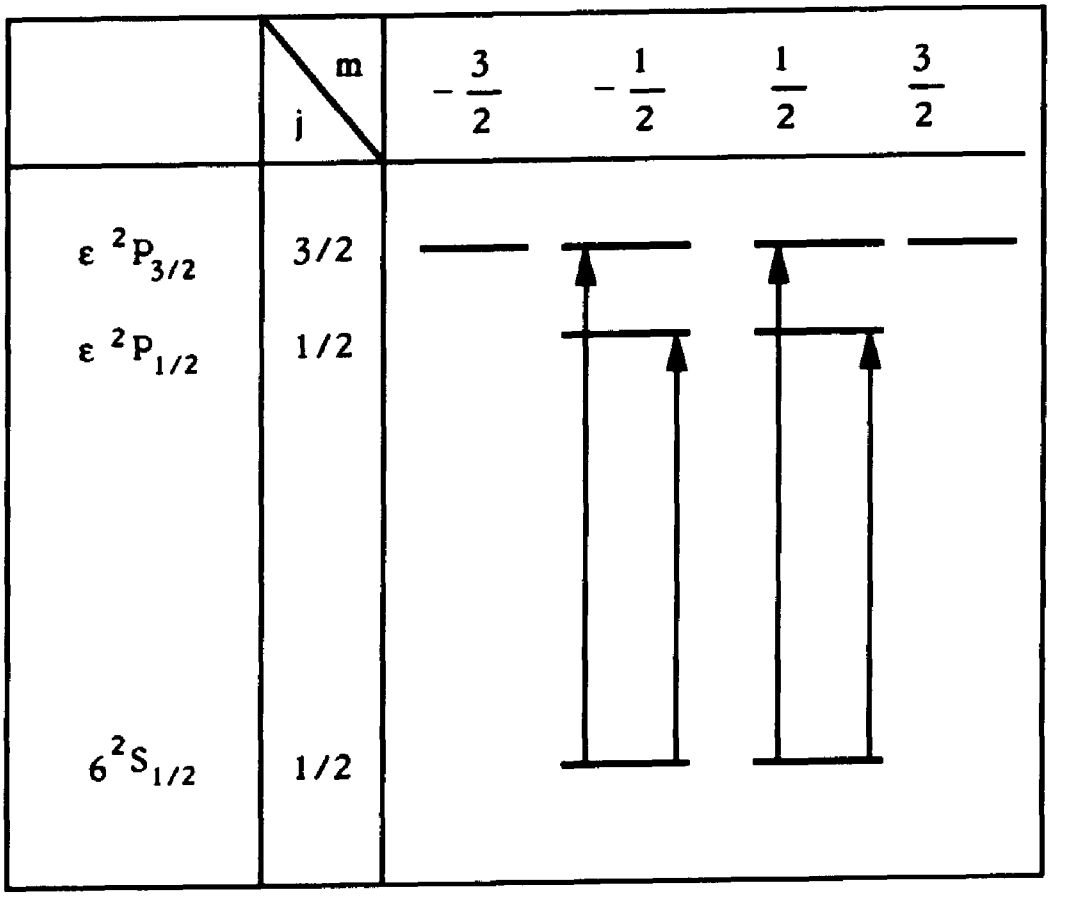

Figure. 3.1 Photoionization transition for cesium atom from $6^2S_{1/2}$ ground state to $\varepsilon\ ^2P_{1/2}$ and $\varepsilon\ ^2P_{3/2}$ continuum states.

$$\Delta j = 0, \pm 1 \qquad (0 \not\leftrightarrow 0) \tag{3.5}$$

$$\Delta m_j = 0 \tag{3.6}$$

We restrict ourselves to photoionization from the ground state. For the alkali metal atoms, the ground state is $n^2S_{1/2}$ or more explicitly $|nljm_j\rangle = |n0\tfrac{1}{2}\tfrac{1}{2}\rangle$ and $|n0\tfrac{1}{2}-\tfrac{1}{2}\rangle$, where n=2 for Li, n=3 for Na, n=4 for K, n=5 for Rb, and n=6 for Cs. The final state is composed of one or more of the following: $\left|Kp\,\frac{1}{2}\,\frac{1}{2}\right\rangle$, $\left|Kp\,\frac{3}{2}\,\frac{1}{2}\right\rangle$, $\left|Kp\frac{1}{2}-\frac{1}{2}\right\rangle$, and $\left|Kp\frac{3}{2}-\frac{1}{2}\right\rangle$. So in this interaction of a rubidium atom in the ground 5s state with linearly polarized radiation, the transition channels are limited to (for simplicity we use rubidium as an example):

$$\left|5s\,\frac{1}{2}\,\frac{1}{2}\right\rangle \longrightarrow \left|Kp\,\frac{1}{2}\,\frac{1}{2}\right\rangle$$
$$\left|5s\,\frac{1}{2}\,\frac{1}{2}\right\rangle \longrightarrow \left|Kp\,\frac{3}{2}\,\frac{1}{2}\right\rangle$$

$$\left|5s\frac{1}{2}-\frac{1}{2}\right\rangle \longrightarrow \left|Kp\frac{1}{2}-\frac{1}{2}\right\rangle$$
$$\left|5s\frac{1}{2}-\frac{1}{2}\right\rangle \longrightarrow \left|Kp\frac{3}{2}-\frac{1}{2}\right\rangle .$$

The angular distribution may be expressed as:

$$\frac{d\sigma}{d\Omega} = E^{2\omega}e^{i\phi}\sum_{g}\left|\sum_{j}\left\langle \Psi_{\kappa}(\vec{r})\,|\,j'm'\right\rangle\left\langle j'm'\,|\,r\cos\theta\,|\,jm\right\rangle\right|^2 \tag{3.7}$$

Using equation (1.6) and setting the l=0, m=0, as well as considering the Clebsch-Gordan coefficients [3.32], one gets:

$$\frac{d\sigma}{d\Omega} = E^{2\omega} e^{i\phi} \left\{ \left| -\frac{1}{\sqrt{3}} \left\langle \Psi_{\kappa}(\vec{r}) \middle| \frac{1}{2}\,\frac{1}{2} \right\rangle \frac{1}{\sqrt{3}} + \sqrt{\frac{2}{3}} \left\langle \Psi_{\kappa}(\vec{r}) \middle| \frac{3}{2}\,\frac{1}{2} \right\rangle \frac{1}{\sqrt{3}} \right|^2 + \left| \frac{1}{\sqrt{3}} \left\langle \Psi_{\kappa}(\vec{r}) \middle| \frac{1}{2}\,-\frac{1}{2} \right\rangle \frac{1}{\sqrt{3}} + \sqrt{\frac{2}{3}} \left\langle \Psi_{\kappa}(\vec{r}) \middle| \frac{3}{2}\,-\frac{1}{2} \right\rangle \frac{1}{\sqrt{3}} \right|^2 \right\}. \tag{3.8}$$

The projections of the excited eigenstates $|jm_j\rangle$ on the outgoing plane wave are given by:

$$\left\langle \Psi_{\kappa}(\vec{r}) \middle| \frac{1}{2}\,\frac{1}{2} \right\rangle = -i e^{i\delta_{1/2}} R_{1/2} \left[\sqrt{\frac{2}{3}} Y_{11}(\Theta, \Phi) - \sqrt{\frac{1}{3}} Y_{10}(\Theta, \Phi) \right]$$

$$\left\langle \Psi_{\kappa}(\vec{r}) \middle| \frac{3}{2}\,\frac{1}{2} \right\rangle = -i e^{i\delta_{3/2}} R_{3/2} \left[\sqrt{\frac{1}{3}} Y_{11}(\Theta, \Phi) + \sqrt{\frac{2}{3}} Y_{10}(\Theta, \Phi) \right]$$

$$\left\langle \Psi_{\kappa}(\vec{r}) \middle| \frac{1}{2}\,-\frac{1}{2} \right\rangle = -i e^{i\delta_{1/2}} R_{1/2} \left[\sqrt{\frac{2}{3}} Y_{1-1}(\Theta, \Phi) - \sqrt{\frac{1}{3}} Y_{10}(\Theta, \Phi) \right]$$

$$\left\langle \Psi_{\kappa}(\vec{r}) \middle| \frac{3}{2}\,-\frac{1}{2} \right\rangle = -i e^{i\delta_{3/2}} R_{3/2} \left[\sqrt{\frac{1}{3}} Y_{1-1}(\Theta, \Phi) + \sqrt{\frac{2}{3}} Y_{10}(\Theta, \Phi) \right] \tag{3.9}$$

where $R_{1/2}$ and $R_{3/2}$ are the radial matrix element:

$$R_{1/2} = \int_0^{\infty} dr \Psi^*\left(\varepsilon p \frac{1}{2}, r\right) r \Psi\left(5s\frac{1}{2}, r\right) \tag{3.10}$$

$$R_{3/2} = \int_0^{\infty} dr \Psi^*\left(\epsilon p \frac{3}{2}, r\right) r \Psi\left(5s\frac{1}{2}, r\right) \qquad (3.11)$$

The spherical harmonic functions $Y_{10}(\Theta, \Phi)$, $Y_{11}(\Theta, \Phi)$ and $Y_{1-1}(\Theta, \Phi)$ are given by:

$$Y_{10}(\Theta, \Phi) = \sqrt{\frac{3}{4\pi}} \cos\Theta \qquad (3.12)$$

$$Y_{11}(\Theta, \Phi) = -\sqrt{\frac{3}{8\pi}} \sin\Theta e^{i\phi} \qquad (3.13)$$

$$Y_{1-1}(\Theta, \Phi) = \sqrt{\frac{3}{8\pi}} \sin\Theta e^{-i\phi} . \qquad (3.14)$$

Putting these forms inside equation (3.9), and using the Clebsch-Gordan coefficients and equation (1.8), and considering

$$Y_{11}^*(\Theta, \Phi) Y_{10}(\Theta, \Phi) + Y_{1-1}(\Theta, \Phi) Y_{10}^*(\Theta, \Phi) = 0 \qquad (3.15)$$

at last we get:

$$\frac{d\sigma}{d\Omega} = \frac{1}{27} E \left\{ 2 \left| R_{3/2} e^{i\delta_{3/2}} - R_{1/2} e^{i\delta_{1/2}} \right|^2 \left| Y_{11}(\Theta, \Phi) \right|^2 + \left| 2R_{3/2} e^{i\delta_{3/2}} + R_{1/2} e^{i\delta_{1/2}} \right|^2 \left| Y_{10}(\Theta, \Phi) \right|^2 \right\} \qquad (3.16)$$

Replacing the spherical harmonic functions (3.12-3.14) in equation (3.16) and using the form

$$\left| R_{3/2} e^{i\delta_{3/2}} - R_{1/2} e^{i\delta_{1/2}} \right|^2 = R_{3/2}^2 + R_{1/2}^2 - 2R_{3/2} R_{1/2} \cos\delta \qquad (3.17.)$$

$$\left|2R_{3/2}e^{i\delta_{3/2}}+R_{1/2}e^{i\delta_{1/2}}\right|^2=4R_{3/2}^2+R_{1/2}^2+4R_{3/2}R_{1/2}\cos\delta \qquad (3.18)$$

we get:

$$\frac{d\sigma_1}{d\Omega}=A_1(1+\alpha\cos^2\Theta), \qquad (3.19)$$

where α and A_1 equal

$$\alpha=3\frac{R_{3/2}^2+2R_{3/2}R_{1/2}\cos(\delta_{3/2}-\delta_{1/2})}{R_{3/2}^2+R_{1/2}^2-2R_{3/2}R_{1/2}\cos(\delta_{3/2}-\delta_{1/2})} \qquad (3.20)$$

$$A_1=\frac{E^{2\omega}e^{i2\phi}}{8\pi\left(R_{3/2}^2+R_{1/2}^2-2R_{3/2}R_{1/2}\cos(\delta_{3/2}-\delta_{1/2})\right)}. \qquad (3.21)$$

Correspondingly the asymmetry parameter β has form:

$$\beta(\varepsilon)=\frac{2\alpha}{3+\alpha}=2\frac{R_{3/2}^2+2R_{1/2}R_{3/2}\cos(\delta_{3/2}-\delta_{1/2})}{2R_{3/2}^2+R_{1/2}^2}. \qquad (3.22)$$

In many situations the phase shift difference is approximately equal to zero, i.e. $\cos(\delta_{3/2}-\delta_{1/2})\approx 1$ [33, 34]. This may be explained as following. Because the spin-orbit effects in the P continuum state are relatively small, the $\varepsilon P_{3/2}$ and $\varepsilon P_{1/2}$ wave functions are similar, and the phase shift difference is small and approximately constant over the entire energy range.

3.3 Experimental determination of photoelectron angular distributions for $6^2S_{1/2} \rightarrow \varepsilon P_j$ photoionization of cesium near the Cooper minimum

Cesium is the atom of choice for many studies of spin-orbit effects, both theoretical and experimental. One reason for this is that cesium is the most massive non-radioactive alkali metal and thus the spin-orbit perturbation is relatively large.

Ong and Manson in 1979 [3.15] calculated photoionization cross section of the outer ns electron in alkali metals, Na, K, Rb, and Cs, using Dirac-Fock wave functions. Their results showed strong variations of the photoelectron angular distribution parameter β with photon energy. This deviation is due to the spin-orbit interaction of the continuum electron which gives rise to two final states $\varepsilon P_{3/2}$ and $\varepsilon P_{1/2}$. Their matrix elements for the transitions to the $\varepsilon P_{3/2}$ and $\varepsilon P_{1/2}$ differ from each other, thereby resulting in an energy-dependent β. Their calculation showed that the phase shifts for $\varepsilon P_{3/2}$ and $\varepsilon P_{1/2}$ continuum waves have several outstanding characteristics: in all the alkali metals over the energy range of 4 to 5 eV above threshold the phase shifts $\delta_{3/2}$ and $\delta_{1/2}$ are very slowly varying and the phase-shift differences are almost constant. The value of the difference for cesium is approximately 0.031π.

In 1979 Huang and Starace [3.16], considering the experiment results of Baum *et al.* [3.6], reported their calculations of cesium photoionization and photoelectron spin polarization, taking proper account of the final-state spin-orbit interaction. In addition to the spin-orbit interaction of the photoelectron in the field of the nucleus, they evaluated exactly the matrix elements of the mutual spin-orbit operator. The final state perturbation matrix elements were then used to obtain improved final state wave functions in the $j=\frac{1}{2}$ and $j=\frac{3}{2}$ photoelectron channels. Their results are in qualitative agreement with previous Dirac-Fock calculations, but agree more closely with experiment near threshold than all previous ab initio calculations.

Since the energy at which the cross section for the $j=\frac{1}{2}$ channel vanishes occurs very close to the ionization threshold, the cross section for ionization remains relatively large throughout the region about the Cooper minimum making cesium a good source of spin polarized electrons. By [3.22, 3.23, 3.35] the polarization is 100% at about λ=295 nm. This property allows us to observe a wide variation of photoelectron angular distributions.

The photoionization transition for the cesium atom from the $6^2S_{1/2}$ ground state to $\varepsilon P_{1/2}$ and $\varepsilon P_{3/2}$ continuum states is shown in figure 3.1. For cesium ionization from $6^2S_{1/2} \rightarrow \varepsilon P_j$, the asymmetry parameter may be expressed as in equation (3.22). In the absence of spin-orbit coupling, $R_{3/2}=R_{1/2}$ and the asymmetry parameter β reduces to 2. $R_{3/2}$ and $R_{1/2}$ are affected by the spin-orbit perturbation, however, and as the photon energy is varied near the Cooper minimum, $R_{3/2}$ and $R_{1/2}$ each pass through zero, but at somewhat with different energies. Because of the slight radial contraction of j=1/2 channel, the $nS_{1/2} \rightarrow \varepsilon P_{1/2}$ amplitude vanishes first. The β is expected to decrease rapidly from its normal value of two. From equation (3.18) we see that when $R_{1/2} \rightarrow 0$, $\beta \rightarrow 1$. Beyond this zero point, $R_{1/2}$ changes sign and increases again while $R_{3/2}$ decreases. $\beta=0$ at $R_{3/2}=-2R_{1/2}$. In this range the maximum emitted photoelectron flux is parallel to the polarization of light. In figure 3.2 we see that when β approaches 0 (β=0.0626 at λ=294.4), the photoelectron angular distribution becomes nearly spherical. Beyond this point, as the laser wavelength continues to decrease, β becomes negative so that the maximum emitted electron flux direction changes to $\Theta=90°$. β reaches a minimum value, approximately -1 ($R_{3/2} = -\frac{1}{2}R_{1/2}$), and then begins to increase again as $R_{3/2} \rightarrow 0$. Our experimental results clearly show the change in angular distributions and the existence of the Cooper minimum.

We measured the cesium angular distribution at eight different wavelengths near the Cooper minimum [3.36]. Our work represents the first measurements of photoelectron angular distributions for

different photon energies in an alkali metal atom with initial ground state. The data clearly shows the importance of spin-orbit effects in the photoionization continuum and support the previous theoretical predictions of a Cooper minimum.

The experimental photoelectron angular distributions are shown in figure 3.2. The degree of linear polarization of the rotated beam was measured to be better than 1000:1. The photoionization threshold corresponds to a laser excitation wavelength of 318.4 nm for cesium. Our measurements were made in the wavelength range from λ=266.0 nm to λ=313.5 nm. The data at 266 nm were taken using the fourth harmonic of the Nd:YAG laser. The polarization of the uv light rotated by means of optical Fresnel rhomb. The laser polarization rotates by twice the rotation angle of Fresnel rhomb. No disparity was observable between the data in the first half of the rhomb rotation and the data in the second half. Taking advantage of the symmetry of geometry, the data at angle Θ is the average of data at Θ and Θ+180°.

In figure 3.2 the crosses show the experimental data, each data point representing 2400 laser pulses. Each data point has been adjusted to correct for coincidence errors, assuming the electron detection is governed by Poisson statistics. The power of the uv beam and the density of the atomic beam were adjusted to a level such that the maximum probability of detecting an electron per laser shot was approximately 30%. The background was measured at a variety of angles Θ by blocking the atomic beam, but no asymmetry was observable within the accuracy of these measurements. Thus the signal was determined by subtracting the background from each data point in the angular distributions. The solid line for each distribution is the result of a least mean squares fit of equation (3.1) to the data. The standard deviation of each data point is quite consistent with the shot noise limit $\sigma \approx \sqrt{n}$, where n is the number of detected electrons.

Space change effects are also minimal. This is especially important for measurements of angular distributions of low kinetic energy electrons, where stray residual fields can influence

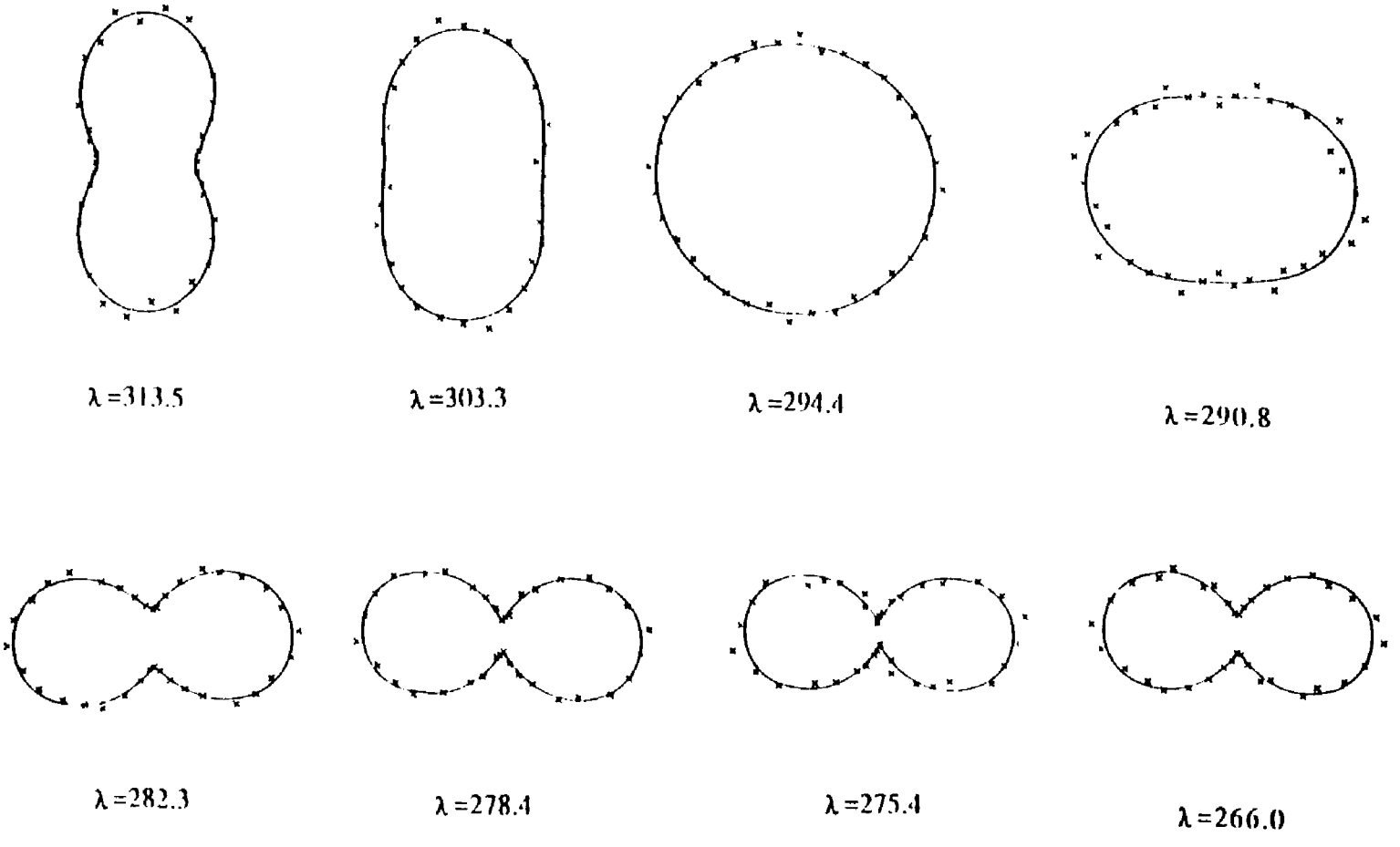

Figure 3.2 Photoelectron angular distributions of cesium with light of wavelength from 266 to 313.5 nm. The laser polarization is in the vertical direction.

measurements significantly. The electric fields in our measurements of angular distributions would cause a change in the effective aperture size, thus influencing the angular resolution. Since a non-zero effective aperture size results in a relative increase of the isotropic part of the angular distribution, any stray fields which are present could cause a systematic error to our data. In the next chapter, dealing with the measurement of two-photon angular distributions we will show that the residual fields are very weak in the interaction region. At this field our calculation showed a negligible effect of asymmetry parameter β, even at the lowest photoelectron kinetic energies.

The measured asymmetry parameters β determined by equation (3.1) are given in table 3.1. These values have been adjusted for the effect of the finite aperture size and interaction volume. This is determined by averaging the square of the cosine of the angle Θ over both these regions. Our calculation shows the 0.9% decrease for asymmetry parameter β. $\Delta\beta_S$ is purely statistical, and represents one standard deviation of the mean. Considering the background noise count rate we give another uncertainty, $\Delta\beta_T$, in table 3.1. These values were obtained by scaling $\Delta\beta_S$ by a factor (1+r), where r represents the ratio of the standard deviation of the noise to the standard deviation of the signal data.

Table 3.1 Experimental results of measurement of cesium, including asymmetry parameter, β, the Fano parameter, $x(\varepsilon)$. The uncertainties of each represent one standard deviation of the mean.

λ(nm)	ε(eV)	β	$\Delta\beta_s$	$\Delta\beta_T$	x	Δx
313.5	0.061	0.817	0.039	0.039	1.75	0.05
303.3	0.194	0.452	0.025	0.032	1.37	0.03
294.4	0.317	-0.068	0.014	0.031	0.95	0.02
290.8	0.370	-0.289	0.033	0.046	0.79	0.03
282.3	0.498	-0.727	0.020	0.068	0.45	0.06
178.4	0.559	-0.848	0.018	0.053	0.33	0.06
275.4	0.608	-0.889	0.050	0.086	0.28	+0.10/-0.15
266.0	0.767	-0.882	0.030	0.057	-0.36	0.06

From table 3.1 we note that the β values decrease as the Cooper minimum is approached and increase again after the minimum is passed. The asymmetry parameter passes through zero near λ =294.4 nm, at which point the photoelectron angular distribution is nearly spherical. Our experiment clearly shows the rapid variation of the photoelectron angular distribution over a wide range of wavelengths near the Cooper minimum. The data for the asymmetry parameter β appear to have a minimum value greater than -1. There are several factors such as the finite aperture size and residual electric field effects which would result in $\beta_{min}>-1$. But these influences are very small. In figure 3.3 we compare the measured asymmetry parameters β with other author's results. We have also shown Norcross's calculated results of the asymmetry parameter for cesium as the dot-dashed line in figure 3.3 [3.12]. From figure 3.3 the parameter β from our measurements of the photoelectron angular distributions and the β through measurements of the Fano parameter $x(\varepsilon)$ show almost the same values. The theoretical results of Ong and Manson [3.15] (dashed line), and of Huang and Starace [3.16] (solid lines) are also shown in figure 3.3.

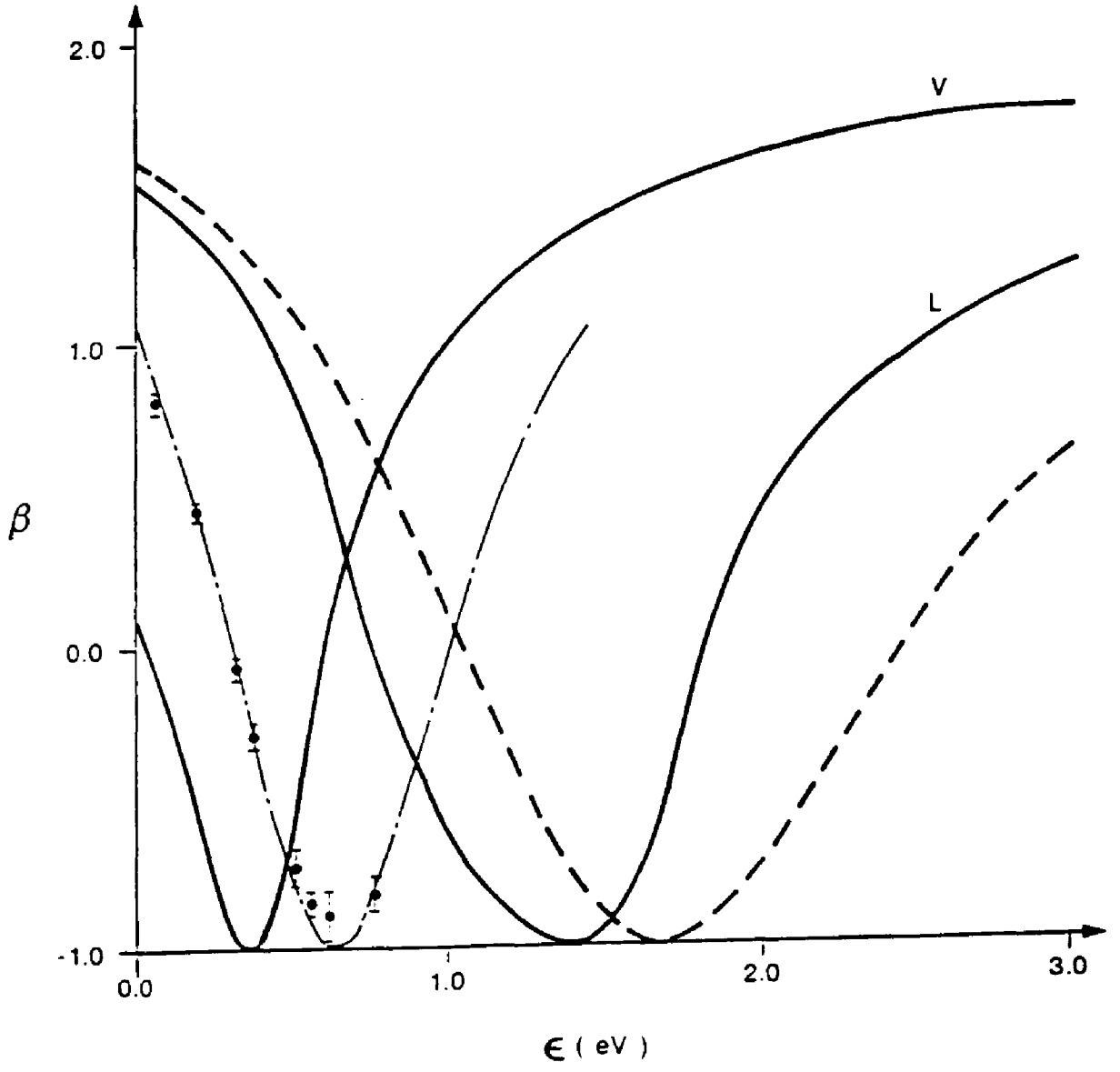

Figure 3.3 Asymmetry Parameter β of cesium $6^2S_{1/2} \rightarrow \varepsilon P_j$ photoionization vs. photoelectron energy ε. The data points represent the results of this work. Results of ab initio calculations of Ong and Manson [3.27], dashed line, and Huang and Starace [3.28], solid lines, are also shown. The latter were carried out in length (L) and velocity (V) gauges, the results of which are shown here. The dot-dashed line represents the results of calculations by Norcross [3.26] for the Fano parameter, which we have converted to β.

As mentioned before the spin-orbit effects not only cause the change of asymmetry parameter β, but also cause the change of Fano parameter $x(\varepsilon)$, which is a measure of the difference of the transition moments $R_{1/2}$ and $R_{3/2}$. Table 3.1 also shows the Fano parameter $x(\varepsilon)$ of our results. Clearly the sign of $x(\varepsilon)$ cannot be determined from our measurements, but we can get it from this table. The phase shift difference $\delta=\delta_{3/2}-\delta_{1/2}$ is very small, so the angular distribution asymmetry parameter β is a very good approximation determined by Fano parameter $x(\varepsilon)$. The asymmetry parameter β may be deduced by

$$\beta=\frac{2}{3}\cdot\frac{3(x^2-1)-2(x+1)(x-2)(1-\cos\delta)}{(x^2+2)}\,. \qquad (3.24)$$

The $x(\varepsilon)$, as a function of the electron kinetic energy, ε, are shown in figure 3.4. We have also shown in figure 3.4 the results of the two other experimental results of $x(\varepsilon)$ and two semi-empirical calculations for comparison. The data points from Baum et al. [3.6, 3.8, 3.9] shown as open circles in figure 3.4 are derived from the measurements of the asymmetry $Q(\varepsilon)$ in the photoionization current from a polarized cesium beam for left or right circularly polarized light [3.6]. Another set of data points, represented by $x(\varepsilon)$ in figure 3.4, come from Heinzmann, Kessler, and Lorenz [3.7], who measured the spin polarization of the ejected electron, $P(\varepsilon)$, and obtained $x(\varepsilon)$ using $P(\varepsilon)=(2x+1)/(x^2+2)$. The uncertainties for our data are much smaller than the others for lower electron kinetic energies, while for higher electron energies they are comparable. The solid lines on the figure 3.4 are results of the semi-empirical calculations of Weisheit [3.11]. The dashed line is from the results of Norcross [3.12]. From figure 3.4 our data is in good agreement with the Norcross curve. Other results of the Fano parameter calculations [3.18, 3.19, 3.37, 3.38] in cesium are not shown in this figure.

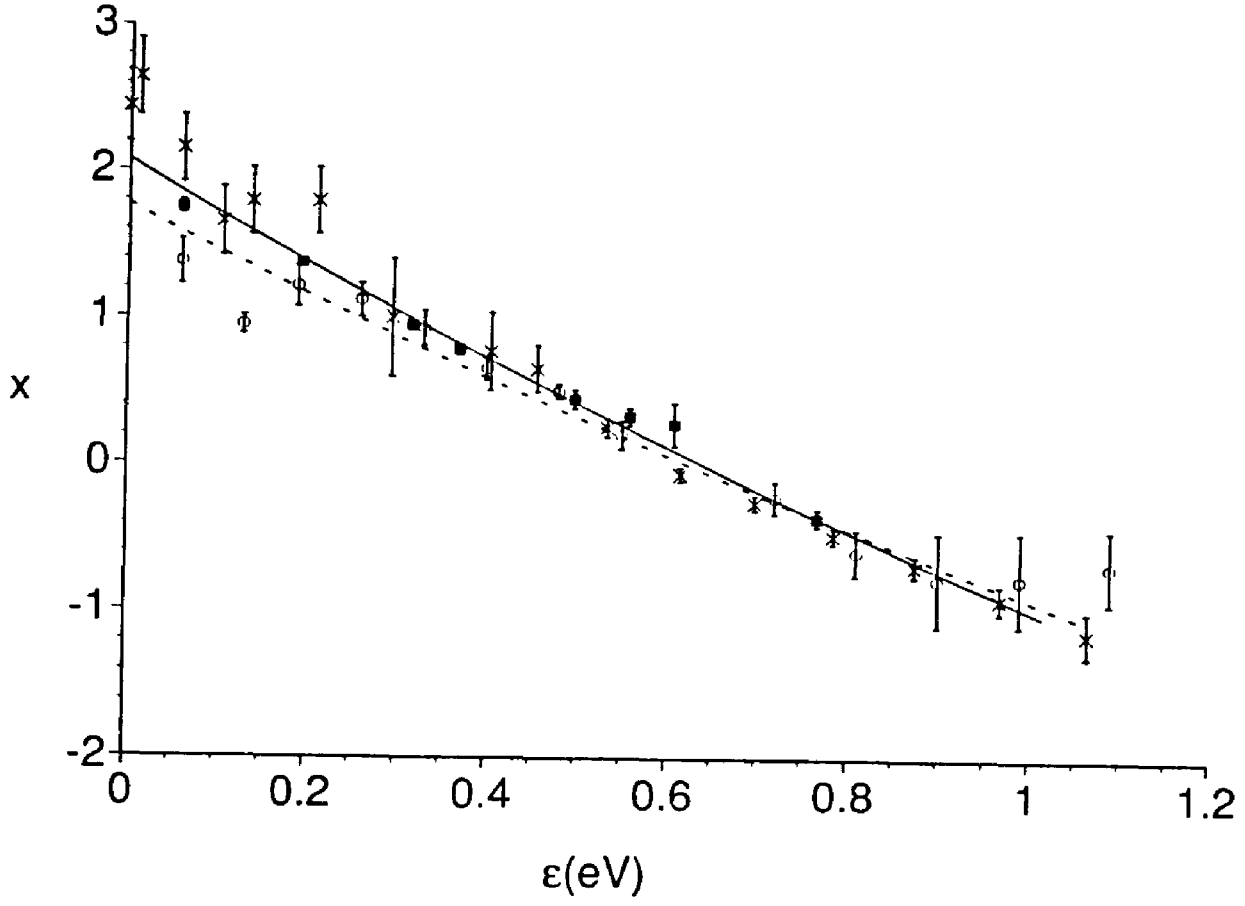

Figure 3.4 The Fano parameter, x, as a function of photoelectron energy. The present data is shown by the square data points. The uncertainties of our data in the range $0.19 < \varepsilon < 0.4$ are less than the size of the squares. The results of Heinzmann, Kessler and Lorenz are shown as x's, and those of Baum Lubell and Raith as circles. Also shown are the results of semi-empirical calculations by Weisheit [3.7], dashed line, and Norcross [3.26], solid line.

3.4 Experimental results of rubidium photoelectron angular distributions for $5^2S_{1/2} \rightarrow \varepsilon P_j$

Another atom whose photoelectron angular distributions we measured is rubidium, whose initial state is the ground 5s state. Absorbing an ultraviolet photon, the rubidium atom may transfer from the ground 5S to the $\varepsilon P_{3/2}$ and $\varepsilon P_{1/2}$ continuum states. The photoionization transition is shown in figure 3.5.

Some calculations were done [3.15, 3.18, 3.20, 3.39] for the rubidium photoelectron angular distribution. Ong and Manson's calculation of rubidium showed that the Cooper minimum occurs in the threshold region. The phase shifts for $\varepsilon P_{3/2}$ and $\varepsilon P_{1/2}$ continuum wave function of rubidium is 0.013π and nearly constant in the near threshold range.

The experimental results are shown in figure 3.6 in a polar diagram [3.40]. The experimental condition was similar to that of cesium experiment. The laser intensity at 280 nm was 40 μJ. For each data point, 1000-1800 laser pulses were used. The crosses are the experimental data points, and the solid line was obtained in a least mean squares fit of the analytical function (3.1) of the experimental points. The error bars in some data points represent the typical standard deviation of these data. The errors in our experiment are very small. The angular distribution was measured for five different wavelengths in the range from 266 nm to 286 nm. From the diagram the shapes can be seen to change with increasing photon energy. The β values for the different laser wavelengths are compiled in table 3.2. The experimental errors representing the standard deviation of the fit are shown in the table 3.2 too.

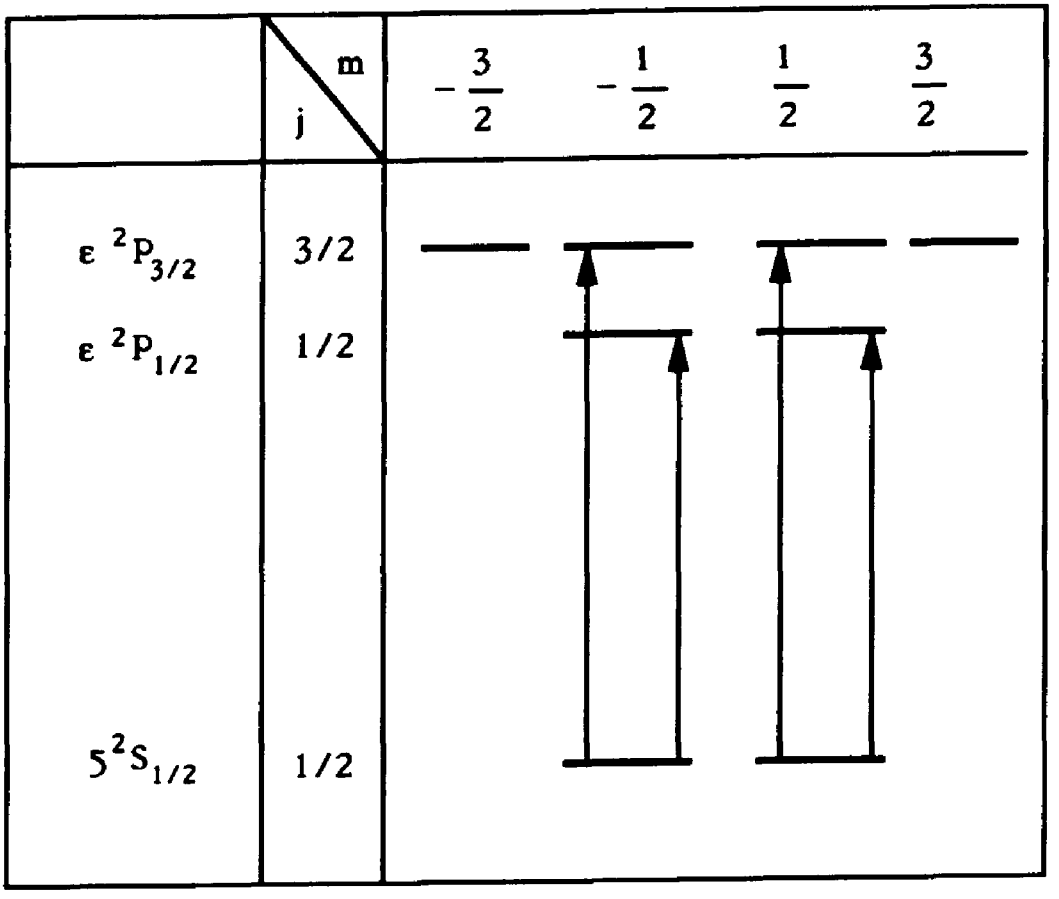

Figure. 3.5 Photoionization transition for rubidium atom from $5^2P_{1/2}$ ground state to $\varepsilon\ ^2P_{1/2}$ and $\varepsilon\ ^2P_{3/2}$ continuum states.

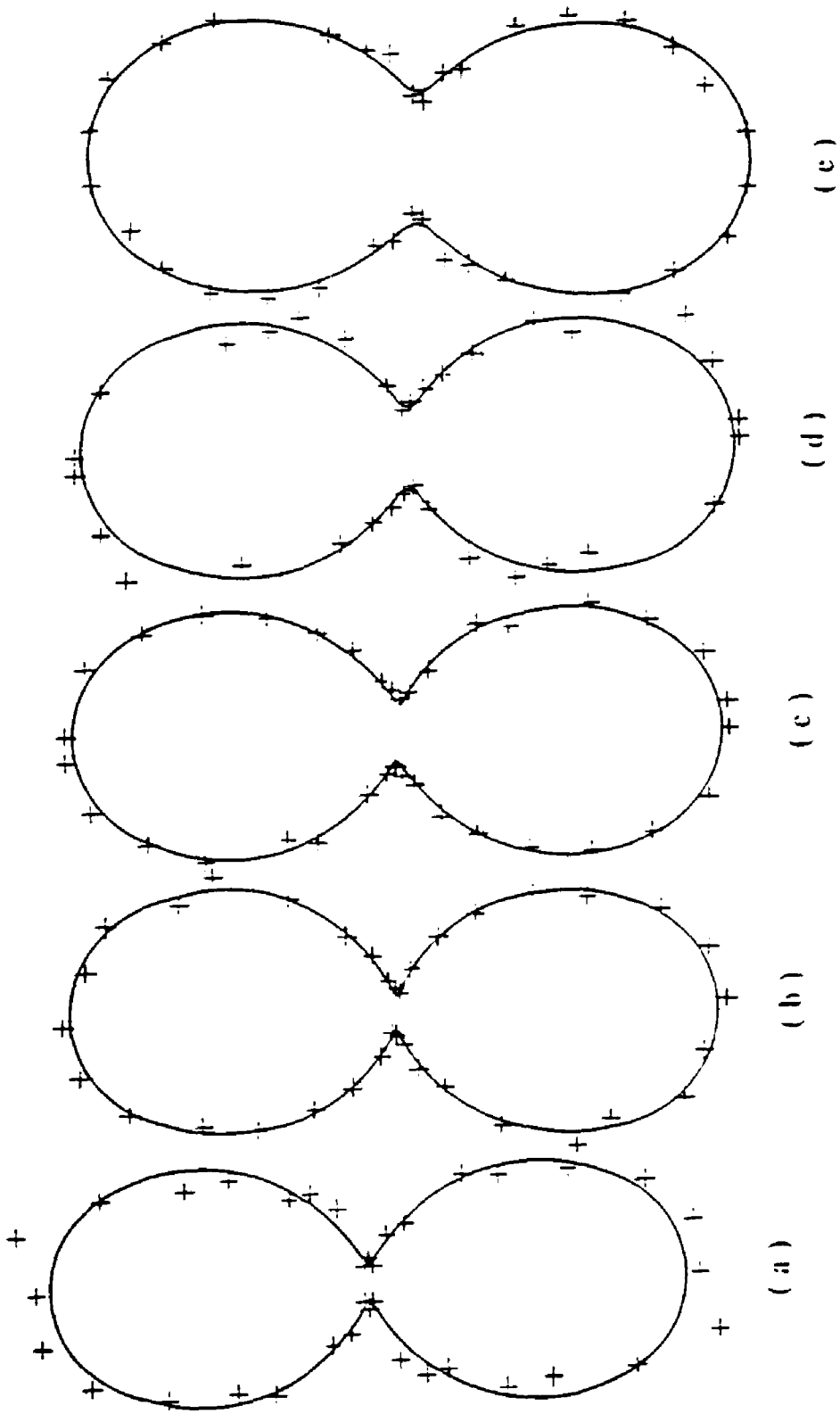

Figure 3.6 Photoelectron angular distributions of rubidium with light of wavelength from 266 to 285.3 nm. The laser polarization is in the vertical direction. (a) λ=285.3 nm, (b) λ=284.0 nm, (c) λ=280.3 nm, (d) λ=275.3 nm, (e) λ=266.0 nm.

Table 3.2 Experimental results of measurement of rubidium for asymmetry parameter, β, the Fano parameter, $x(\varepsilon)$, and uncertainties of $\Delta\beta$.

λ n m	α	β	$\Delta\beta$	$x(\varepsilon)$
266.0	3.913	1.132	0.023	2.204
275.3	6.913	1.395	0.036	2.794
280.3	12.072	1.602	0.031	3.362
283.5	17.251	1.704	0.021	4.204
285.3	19.992	1.759	0.036	4.497

Figure 3.7 shows our β-value vs. energy of the incident photons. For comparison the experimental curve of Baum, Lubell, and Raith who measured the ionization intensity asymmetries for polarized atoms using right or left circularly polarized light, and theoretical curves of Weisheit, and Ong and Manson are drawn on the same diagram. The results of the Baum, Lubell, and Raith, and Weisheit were reported in terms of the Fano parameter, $x(\varepsilon)=(2R_{3/2}+R_{1/2})/(R_{3/2}-R_{1/2})$, but these are easily converted to β. Both the theoretical results show rapid variation of β from a value close to two for low electron energies to -1, and then an increase again to 2 for large electron energy. The data in this work is in good agreement with Weisheit's calculated results and Baum's experimental data.

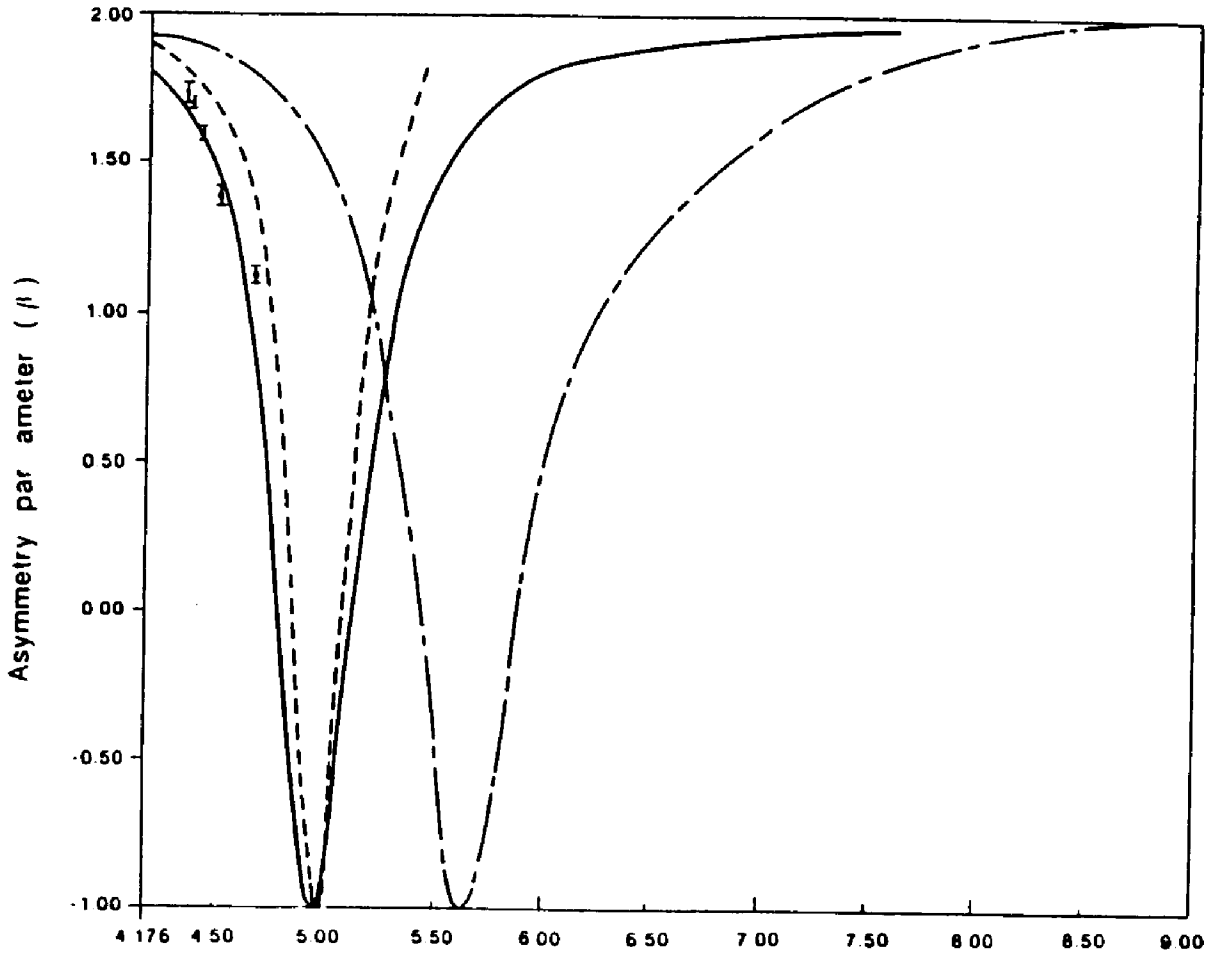

Figure 3.7 Asymmetry parameter β of rubidium $5^2S_{1/2} \rightarrow \varepsilon P_j$ photoionization vs. photoelectron energy ε. Data points represent the results of this work. Results of Weisheit's calculation [3.11], solid line, and Baum *et al.* experimental data [3.6], dashed line are also shown. Dot and dashed line represents the results of calculations by Ong and Manson [3.15].

3.5 List of references

3.1 E. Fermi, "Uber das Intensitatsverhaltnis der Dublettkomponenten der Alkalien", Z. Phys., Vol. 59, p. 680, (1930).

3.2 M. J. Seaton, "A comparison of theory and experiment for photo-ionization cross section", Proc. Roy. Soc. (London) Ser. A, Vol. 208, p. 418, (1951).

3.3 U. Fano, "Spin Orientation of photoelectrons ejected by circularly polarized light", Phys. Rev. A, Vol. 178, p. 169, (1969).

3.4 U. Fano, "Spin Orientation of Photoelectrons: Erratum and Addendum", Phys. Rev., Vol. 184, p. 250, (1969).

3.5 J. Kessler and J. Lorenz, "Experimental Verification of the Fano Effect", Phys. Rev. Lett., Vol.24, P. 87, (1970).

3.6 G. Baum, M. S. Lubell and W. Raith, "Spin-orbit perturbation in heavy alkali atoms", Phys. Rev. Lett., Vol. 25, p. 267, (1969).

3.7 U. Heinzmann, J. Kessler, and J. Lorenz, "Elektronen-spinpolarisation bei der Photoionisation Unpolarisierter Casiumatome mit zirkularpolarisiertem Licht", Z. Physik, Vol. 240, p. 42, (1970).

3.8 G. Baum, M. S. Lubell and W. Raith, "Measurement of the Spin-orbit perturbation in the P-State Continuum of Heavy Alkali-Metal Atoms: K, Rb, and Cs", Phys. Rev., Vol. 5, p. 1073, (1972).

3.9 M. S. Lubell and W. Raith, "Polarization effects in photoionization of cesium", Phys. Rev. Lett., Vol. 23, p. 211, (1969).

3.10 J. C. Weisheit, "Photoabsorption by ground-state alkali-metal atom", Phys. Rev. A, Vol. 5, p. 1621, (1972).

3.11 D. W. Norcross, "Photoabsorption by Cesium", Phys. Rev. A, Vol.7, P. 606, (1973).

3.12 G. V. Marr, "The effect of spin-orbit interaction on the angular distribution of photoelectrons from alkali atoms", J. Phys. B: Atom. Molec. Phys., Vol. 7, p. L47, (1974).

3.13 C. N. Yang, "Photoelectron angular distribution for the outer shell of the alkali-metal atoms" Phys. Rev., Vol. 74, p. 764, (1948).

3.14 J. Cooper and R. N. Zare, "Angular distribution of photoelectrons", J. Chem. Phys., Vol. 48, p. 942, (1968).

3.15 W. Ong and S. T. Manson, "Photoelectron Angular Distributions for the Outer Shell of the Alkali-Metal Atoms", Phys. Rev. A, Vol. 20, P. 2364, (1979).

3.16 K-N. Huang and A. F. Starace, "Ab Initio Treatment of Final-State Spin-Obit Interactions: Photoionization of the 6S electron in Cesium", Phys. Rev. A, Vol.19, P. 2335, (1979).

3.17 D. Hofsaess, "Photoabsorption of Alkali and Alkaline Earth Elements Calculated by the Scaled Thomas Fermi Method", Z. Physik, A281, P. 1, (1977).

3.18 I. L. Beigman, L. A. Vainshten, and V. P. Shevelko, "The Effect of Polarization of the Atomic Core on the Oscillator Strengths and Photoionization Cross-Sections of Alkali Element Atoms", Opt. Spec., Vol. 28, p. 229, (1970).

3.19 B. N. Chichko and V. P. Shevelko, Physica Scripta, Vol. 23, P. 1055, (1981).

3.20 W. Hansen, "The Application of Polarisation-Influenced Thomas-Fermi Ion Modes to Alkali-Atom Transitions", J. Phys. B17, p. 4833, (1984).

3.21 M. S. Pindzola, "Angular Distribution of Photoelectrons from Relativistic Wave Functions", Phys. Rev. A, Vol. 32, p. 1883, (1985).

3.22 T. E. H. Walker and J. T. Waber, "Angular Distribution of Photoelectrons from Relativistic Wave Functions", Phys. Rev. Lett, Vol. 30, p. 307, (1973).

3.23 T. E. H. Walker and J. T. Waber, "Spin-Orbit Coupling and Photoionization", J. Phys, B7, p. 674, (1974).

3.24 W. Ong and S. T. Manson, "The photoelectron angular distribution of xenon 5s", J. Phys. B: Atom. Molec. Phys., Vol. 11, p. L65, (1978).

3.25 Warren Ong and Steven T. Manson, "Dirac-Fock Calculations of Photoelectron Angular Distributions of the Outer s Shells of the noble Gases", Phys. Rev. A, Vol. 19, p. 688, (1979).

3.26 W. R. Johnson and K. T. Cheng, "Relativistic effects on low-energy $5s \rightarrow \varepsilon p$ photoionization for xenon", Phys. Rev. Lett., Vol. 40, p. 1167, (1978).

3.27 W. R. Johnson and K. T. Cheng, "Photoionization of the outer shells of neon, argon, krypton, and xenon using the relativistic random-phase approximation", Phys. Rev. A, Vol. 20, p. 978, (1979).

3.28 K. N. Huang and A. F. Starace, "Photoionization of the 5s Subshell of Xenon: A Multichannel K-matrix Calculation Including Spin-Orbit Interaction", Phys. Rev. A, Vol. 21, p. 697 (1980).

3.29 J. L. Dehmer and D. Dill, "Angular distribution of Xe $5s \rightarrow \varepsilon p$ photoelectrons: direct evidence", Phys. Rev. Lett. Vol. 18, p. 1049, (1976).

3.30 M. G. White, S. H. Southworth, P. Kobrin, E. D. Poliakoff, R. A. Rosenberg, and D. A. Shirley, "Angular Distribution of Xe $5s \rightarrow \varepsilon p$ photoelectrons near the Cooper minimum", Phys. Rev. Lett., Vol. 43, p. 1661, (1979).

3.31 L. E. Cuellar, R. N. Compton, H. S. Carmin, Jr. and C. S. Feigerle, "Photoelectron Angular Distributions for ns (n=8-12) Subshells of Cesium: Relativistic Effects", Phys. Rev. Lett., Vol. 65, p. 163, (1990).

3.32 L. I. Schiff, "Quantum Mechanics", Third edition, by McGraw-Hill, Inc.

3.33 T. A. Carlson and A. E. Jonas, "Angular distribution of the photoelectron spectra for Ar, Kr, Xe, He, N_2 and CO", J. Chem. Phys. Vol. 10, p. 4913, (1971).

3.34 D. J. Kennedy and S. T. Manson, "Photoionization of the noble gases: cross section and angular distributions", Phys. Rev. A Vol. 5, p. 227, (1972).

3.35 T. E. H. Walker and J. T. Waber, "The relativistic Theory of the Angular distribution of Photoelectrons in jj Coupling", J. Phys, B6, p. 1165, (1973).

3.36 Yi-Yian Yin and D. S. Elliott, "Experimental Determination Angular Distribution for $6^2S_{1/2} \rightarrow \varepsilon P_j$ Photoionization of Cs near the Cooper Minimum", submited to the Phys. Rev. A.

3.37 J. M. Raimond, M. Gross, C, Fabre, S. Haroche, and H. H. Stroke, "Laser Measurement of Intensity Ratio Anomalies in Principal Series Doublets of Caesium Rydberg States: Does the D_1 Line Vanish?", J. Phys, B11, p. L765, (1978).

3.38 J-J. Chang and H. P. Kelly, "Relativistic Calculations for Photoionization Cross Sections and the Spin Orientation of Photoejected Electrons from Potassium, Rubidium, and Cesium Atoms", Phys. Rev. A, Vol. 5, p. 1713, (1972).

3.39 M. Szulkin and J. Kavuowski, "Core Polarisation and Relativistic Effects in the Alkali Atoms", J. Phys. B14, p. 4729, (1981).

3.40 Yi-Yian Yin and D. S. Elliott, "Measurements of Spin-Orbit Perturbation in Atomic Rubidium through Photoelectron Angular Distributions", Phys. Rev. A, Vol. 45, p. 281, (1991).

CHAPTER 4
PHOTOELECTRON ANGULAR DISTRIBUTION IN TWO-PHOTON IONIZATION AND SPIN-ORBIT INTERACTION

4.1 Introduction

In Chapter 3 we discussed the process of single-photon ionization and the effect that the spin-orbit interaction has on it. Multiphoton ionization by the interaction between the laser field and atomic systems has also attracted considerable interest experimentally and theoretically in the last decade.

In this chapter we introduce precision measurements of the photoelectron angular distribution of rubidium under two-photon absorption conditions from the ground s-state to s and d continuum states, and discuss the asymmetry parameters derived from these distributions. Through these measurements we investigated the influence of the spin-orbit interaction, coupling to different continuum states, and the phase shifts on the ionization processes. All of this information will help us to understand the properties about the interference processes between one- and two-photon ionization in alkali metals.

Many theoretical research works have been concerned with two-photon angular distributions resulting from the interaction of an intense laser field with an atomic system [4.1-4.12, 1.7, 1.8]. Since in most of the experiments reported the external laser field strength is small compared to the internal atomic field strength, the theoretical analysis may be based on the time-dependent perturbation theory developed to the lowest nonvanishing order. Bebb and Gold [4.1, 4.2, 1.7] in 1966 presented a number of calculations of multiphoton transitions in noble gases and alkali atoms using a perturbation

theory. Their theory gave the basis for the interpretation of many experiments at that time.

Quantum-defect theory provides the most expedient method for calculating photoionization processes of the alkalis. Burgess and Seaton [4.3] in 1960 gave the general formula of transition matrix elements for photoionization by considering the model of a single electron moving in a central field. Once the effective quantum numbers n* are known, the approximate bound-state radial wave functions may be obtained. To determine bound-free transition elements approximate free-state radial functions having a well characterized asymptotic form can be used. Their phases are given by $\delta=\pi\mu$, where μ is the extrapolated quantum defect (μ=n-n*). From their theory both bound-bound and bound-free transition integrals may be obtained.

Lambropoulos and Teague [4.7, 4.10-4.12] discussed two-photon and three-photon ionizations of alkali atoms with spin-orbit coupling effects. In calculating the generalized cross section, the spin-orbit effects have been considered. The authors determined the photoelectron angular distribution and the spin-polarization for a two-photon process in terms of transition amplitudes which involve the usual (N-1) fold summations over intermediate atomic states for an N-photon ionization. The explicit formula for the transition amplitudes in terms of radial dipole matrix elements was given and a numerical calculation was performed for alkali atoms. Other work includes that of Pindzola [4.13].

Many experiments were done to study two-photon and multiphoton ionization [4.14-4.23]. Petite, Fabre, Agostini, Crance, and Aymar [4.14] in 1984 measured four- and five-photon absorption for cesium in a nonresonant situation. Using a time-of-flight spectrometer, they measured the energy spectrum and angular distribution of photoelectrons. Strong-field effects are clearly demonstrated by evidence of simultaneous four- and five-photon ionization and by intensity dependent angular distributions. Their measurements gave information about the intensity dependence of four- and five-electron signal for intensities near the saturation

intensity, relative values of angular distribution coefficients, and the ratio of four- and five-photon ionization signals.

Blazewicz, Tang, Compton, and Stockdale [4.15] reported photoelectron energy and angular distributions for resonantly enhanced multiphoton ionization through the three-photon allowed $6s[3/2]^0_1$ and $6s[1/2]^0_1$ states of xenon at laser power densities of 10^9 - 10^{11} W/cm^2. A pulsed amplified dye laser pumped by Nd:YAG laser was used to induce multiphoton ionization. Ionization from three-photon resonance with the $6s[3/2]^0_1$ state gives two photoelectron peaks corresponding to leaving the ion in either the $^2P_{3/2}$ or $^2P_{1/2}$ state. Their experiment showed that these two channels of photoionization give distinctly different angular distributions.

Dodhy, Compton Stockdale, Cooper, Tang, and Lambropoulos [4.16-4.18] reported photoelectron angular distributions for two-photon absorption in rubidium and cesium atoms both in resonant and nonresonant processes. In nonresonant processes they measured the angular distribution at just above the ionization threshold. For cesium and rubidium four different photon energies in the range from λ=620 nm to λ=632.5 nm, corresponding to the photoelectron energy of 25 meV-100 meV, were used. The angular parameters for different energies were obtained. In the resonant case, the photoelectron angular distribution of rubidium for a wavelength at 560 nm was observed. The first photon was in resonance with the $4d^2D$ state via an electric quadruple transition, and when the laser light was detuned from it, angular distributions also were obtained for the first and second above-threshold ionization (ATI) photoelectron peaks. The authors found that tuning to the $4d^2D$ resonance creates a large enhancement of two-photon ionization photoelectron signals, but causes only a modest increase in the above threshold ionization signal. These results are significant because the angular distribution data, particularly in low order,

characterizes the continuum states and the probabilities of transition between them.

Hellmuth, Leuchs, and Smith [4.21] measured two- and three-photon ionization and quantum interference effects of sodium. Two lasers delayed with respect to each other from 0 to 38 ns were used to photoionize the sodium atoms. The quantum interference effect was observed both in the total rate of photoelectron emission and in the photoelectron angular distribution as the delay between the two laser pulses was varied. This periodic variation is the quantum beat signal of the four hyperfine levels of the $3^2P_{3/2}$ states. Their experiment showed that multiphoton ionization angular distributions are an efficient method to study the hyperfine structure of an atom.

4.2 Principle of photoelectron angular distributions for two-photon ionization with spin-orbit interaction and quantum defects

In multiphoton ionization, the angular distribution is determined by many factors. The initial and intermediate atomic states involved in the ionization process, the final state of the ionized atom, the phase difference of partial waves of the free electron, the transition amplitudes to the partial waves, and the character of the radiation field, each play an important role in determining the distributions.

The spin-orbit coupling in unpolarized atoms causes the existence of an important property of the ejected electron beam, the electron-spin polarization. We have discussed this effect for single-photon ionization in Chapter 3. Although differences exist between the single and multiphoton case, the physical basis is the same: the spin-orbit interaction in bound states and in the continuum produces the spin orientation of the photoelectrons, the projection axis being the direction of the wave vector of the incident light. In the off-resonance case, when the two-photon process is performed through a virtual state, the influence of the spin-orbit coupling is indirect in the sense that a greater number of channels than those in the on-resonance case are introduced and it adds more contributions to the total transition amplitude for the same photon energy.

In this thesis we restrict our discussion to ionization only from the ground state and omit any excited states. In two-photon ionization from the ground s state to the continuum s and d states (figure 4.1) the selection rules are the same as single-photon ionization (equations 3.5-3.7), but applied twice, so the channels for linearly polarized light are:

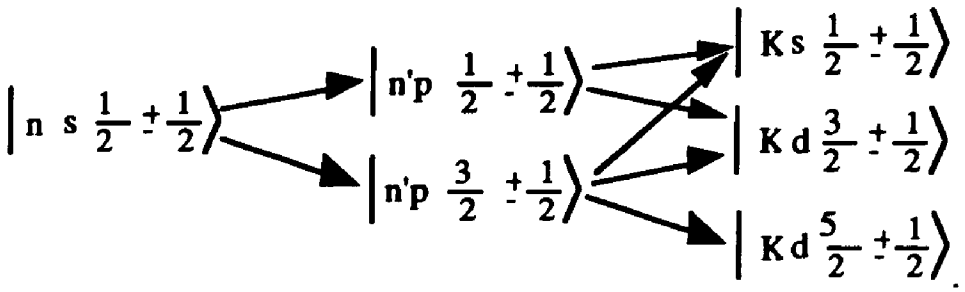

Considerable attention has been given to selection of the most suitable wave functions for use in evaluating the radial dipole matrix elements. The quantum defect Coulomb functions could be most satisfactorily employed for the bound-state functions as well as for the continuum functions. The Coulomb functions are simple enough to allow evaluation of the large number of matrix elements needed while still providing reliable results.

In order to get the explicit expression of the cross section, one needs to sum over all intermediate-states. By Lambropolous and Teague's calculation [4.10] for general two-photon ionization the angular distribution is expressed as:

$$\frac{d\sigma}{d\Omega} \propto \frac{1}{2}\left\{\left|T^0_{++}\right|^2 + \left|T^0_{-+}\right|^2 + \left|T_{--}\right|^2 + \left|T_{+-}\right|^2\right\} \qquad (4.1)$$

where T_{++}, T_{--}, T_{-+}, and T_{+-} have the form:

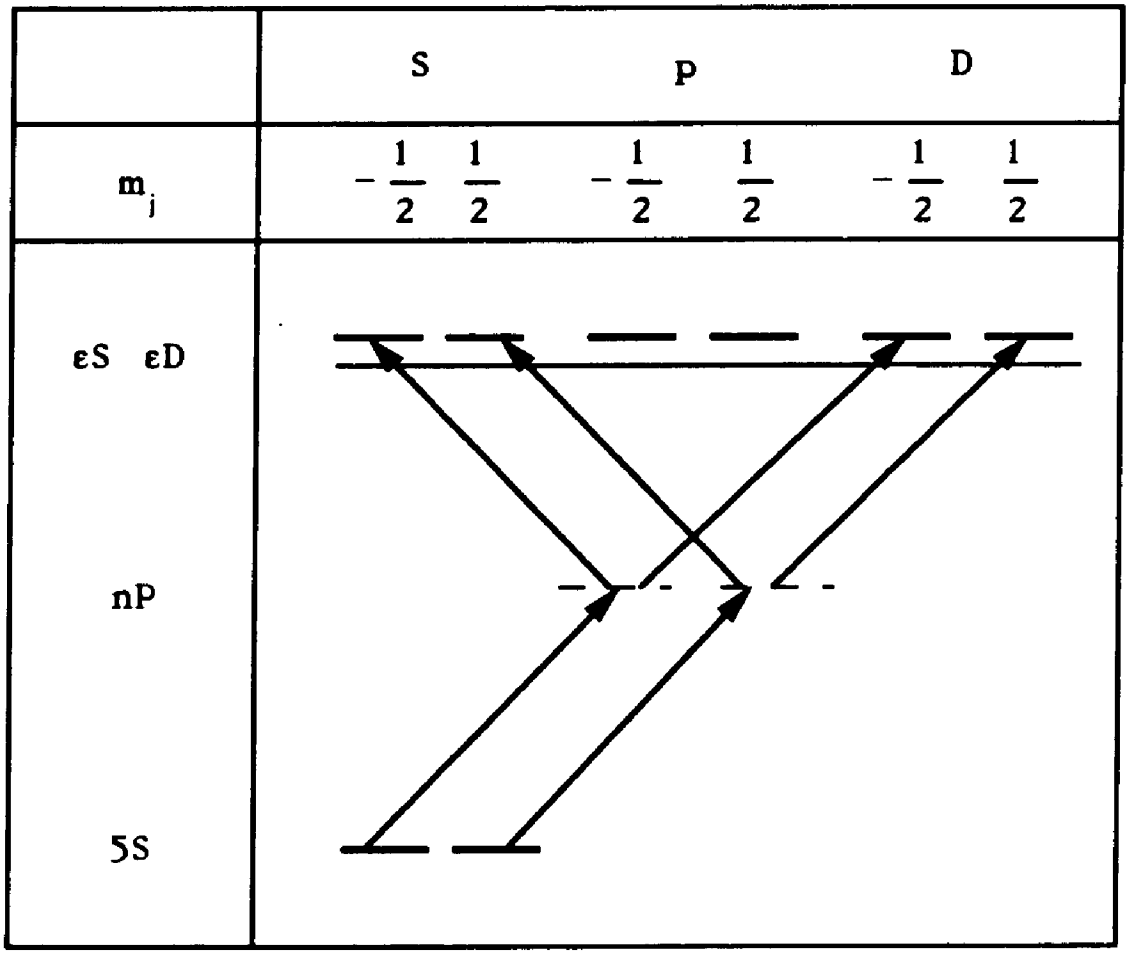

Figure. 4.1 Photoionization transition for rubidium atom from $5\,^2S_{1/2}$ ground state to $\varepsilon\,^2S_{1/2}$ and $\varepsilon\,^2D_{3/2,\,5/2}$ continuum states.

$$T^0_{++} = \left(E^{\omega} e^{i\phi_1}\right)^2 \left[Y_{00}(\hat{K}) e^{i\delta_0} \left(\frac{1}{9}\right)(S_1 + 2S_2) \right.$$

$$\left. + Y_{20}(\hat{K}) e^{i\delta_2} \left(\frac{-2}{45\sqrt{5}}\right)(5S_3 + S_4 + 9S_5) \right] = T^0_{--} \qquad (4.2)$$

$$T^0_{-+} = \left(E^{\omega} e^{i\phi_1}\right)^2 Y_{21}(\hat{K}) e^{i\delta_2} \left(\frac{1}{15}\sqrt{\frac{2}{15}}\right)(5S_3 + S_4 - 6S_5) = T^0_{+-} \qquad (4.3)$$

The T_{++} and T_{--} correspond to spin-preserving interactions from m_s=1/2 and m_s=-1/2 ground states, respectively, while T_{-+} and T_{+-} are for spin changing interactions. The S_i (i=1-5) represent the two-photon transition amplitude, and can be expressed as following:

$$S_1 = 4\pi \sum_{n'} R^{K0}_{n1(1/2)} R^{n1(1/2)}_{n'0} \left(\omega_{n1(1/2)} - \omega_{no} - \omega\right)^{-1} \qquad (4.4)$$

$$S_2 = 4\pi \sum_{n'} R^{K0}_{n1(3/2)} R^{n1(3/2)}_{n'0} \left(\omega_{n1(3/2)} - \omega_{no} - \omega\right)^{-1} \qquad (4.5)$$

$$S_3 = 4\pi \sum_{n'} R^{K2(3/2)}_{n1(1/2)} R^{n1(1/2)}_{n'0} \left(\omega_{n1(1/2)} - \omega_{no} - \omega\right)^{-1} \qquad (4.6)$$

$$S_4 = 4\pi \sum_{n'} R^{K2(3/2)}_{n1(3/2)} R^{n1(3/2)}_{n'0} \left(\omega_{n1(3/2)} - \omega_{no} - \omega\right)^{-1} \qquad (4.7)$$

$$S_5 = 4\pi \sum_{n'} R^{K2(3/2)}_{n1(3/2)} R^{n1(3/2)}_{n'0} \left(\omega_{n1(3/2)} - \omega_{no} - \omega\right)^{-1} . \qquad (4.8)$$

Grouping these transition moments in three combinations,

$$A = \frac{1}{3}(S_1 + 2S_2) \qquad (4.9)$$

$$B = \frac{1}{15}(5S_3 + S_4 + 9S_5) \qquad (4.10)$$

$$C = \frac{1}{5}(5S_3 + S_4 - 6S_5), \qquad (4.11)$$

one gets:

$$\frac{d\sigma}{d\Omega} = (A^2 + B^2 + 2AB\cos\delta)$$

$$\left(1 + \frac{-6B^2 + C^2 - 6AB\cos\delta}{A^2 + B^2 + 2AB\cos\delta}\cos^2\Theta + \frac{9B^2 - C^2}{A^2 + B^2 + 2AB\cos\delta}\cos^4\Theta\right), \qquad (4.12)$$

where $\delta=\delta_s-\delta_d$ is the phase difference of the S and D states partial waves. As mentioned in chapter 1, the photoionization angular distribution for two-photon ionization can be expressed as:

$$\frac{d\sigma_2}{d\Omega} = A_2\left(1 + \alpha_2\cos^2\Theta + \alpha_4\cos^4\Theta\right). \qquad (1.18)$$

Comparing equation (4.12) with it we obtain the parameters α_1 and α_2 as:

$$\alpha_2 = \frac{-6B^2 + C^2 - 6AB\cos\delta}{A^2 + B^2 + 2AB\cos\delta} \qquad (4.13)$$

$$\alpha_4 = \frac{9B^2 - C^2}{A^2 + B^2 + 2AB\cos\delta}. \qquad (4.14)$$

The theoretical value of the relative phase δ for S and D continuum states has been calculated according to [4.3, 1.22]

$$\delta = \delta_s - \delta_d$$
$$= (\delta'_s - \delta'_d) + (\delta''_s - \delta''_d) + \pi \quad (4.15).$$

Here $\delta'_s - \delta'_d$ is the difference of the Coulomb phase of the s and d partial waves for ionized electrons and the $\delta''_s - \delta''_d$ is the difference of the quantum defects for nS and nD states extrapolated into the continuum. The additional π accounts for the different signs of the radial transition elements. The δ'' was given as $\delta'' = \delta''_s - \delta''_d = \pi\mu$, where μ is the quantum defect. The quantum defect was extrapolated into the continuum by fitting an energy dependent quantum defect $\mu(\varepsilon)$ to the negative energy S and D states. $\mu(\varepsilon)$ may be determined by

$$\mu(\varepsilon) = \mu^0 + \mu'\varepsilon \quad (4.16)$$

For the d states there are of course two series corresponding to the two j values 3/2 and 5/2 of the doublets. The results were found to be completely insensitive to which term of the doublet was used and in fact independent of the values of the energy dependent term $\mu'\varepsilon$ [4.2].

The $\delta'_s - \delta'_d$ may be determined as [4.3]:

$$\delta'_s - \delta'_d = \tan^{-1}\frac{1}{2\sqrt{\varepsilon}} + \tan^{-1}\frac{1}{\sqrt{\varepsilon}}, \quad (4.17)$$

where $\varepsilon=(k/z)^2$ is in Rydbergs, k is the electron momentum and z=1 is the effective charge.

By simple calculation from equations (4.13) and (4.14) the $\tilde{A}$ and $\tilde{C}$ are given as:

$$\tilde{A} = -\frac{\alpha_2 + \alpha_4 + 3}{\alpha_2 + \alpha_4} \pm \frac{\sqrt{(\alpha_2 + \alpha_4 + 3)\cos^2(\delta_s - \delta_d) - (\alpha_2 + \alpha_4)(\alpha_2 + \alpha_4 - 3)}}{\alpha_2 + \alpha_4} \qquad (4.18)$$

$$\tilde{C} = \pm \sqrt{\frac{6\tilde{A}\cos(\delta_s - \delta_d) + (6 + \frac{9\alpha_2}{\alpha_4})}{1 + \frac{\alpha_2}{\alpha_4}}}, \qquad (4.19)$$

where $\tilde{A}$ and $\tilde{C}$ are defined as $\tilde{A}=A/B$ and $\tilde{C}=C/B$.

Our purpose is to calculate ratios of cross sections from the 5S state to S and D continuum states. Integrating the angular distributions one gets:

$$\sigma = \int \frac{d\sigma}{d\Omega} d\Omega$$

$$\propto \frac{1}{9}(S_1 + S_2)^2 + \frac{2}{225}(5S_3 + S_4)^2 + \frac{12}{25}S_5^2. \qquad (4.20)$$

The cross sections σ_s, $\sigma_{3/2}$, $\sigma_{1/2}$, and σ_d are determined respectively as:

$$\sigma_s = \frac{1}{9}(S_1 + S_2)^2 \qquad (4.21)$$

$$\sigma_{3/2} = \frac{2}{225}(5S_3 + S_4)^2 \qquad (4.22)$$

$$\sigma_{5/2} = \frac{12}{25}S_5^2 \qquad (4.23)$$

and

$$\sigma_d = \sigma_{3/2} + \sigma_{5/2}$$

$$= \frac{2}{225}(5S_3 + S_4)^2 + \frac{12}{25}S_5^2 . \qquad (4.24)$$

From equations (4.9-4.11) the ratios of cross sections for the s to d state and the 5/2 to 3/2 states are expressed as:

$$\frac{\sigma_s}{\sigma_d} = \frac{15}{2}\frac{A^2}{6 + C^2} \qquad (4.25)$$

$$\frac{\sigma_{5/2}}{\sigma_{3/2}} = \frac{3}{2}\left(\frac{3 - C}{2 + C}\right)^2 . \qquad (4.26)$$

Thus our two-photon ionization angular distributions can be used to determine these ratios of cross-sections, if the phase shifts of the various continuum states can be determined independently.

4.3 Experimental determination of photoelectron angular distributions of rubidium for two-photon ionization

Because of our interest in observing interference effects in rubidium, we have chosen this element for our two-photon ionization angular distribution measurements. After absorbing two laser photons the rubidium atom may transfer from initial 5S ground state to the $\varepsilon S_{1/2}$ and $\varepsilon D_{3/2,5/2}$ continuum states.

Dodhy, Compton, and Stockdale reported [4.24] in 1985 their measurements of photoelectron angular distributions for nonresonant two-photon ionization of rubidium and cesium atoms just above the ionization threshold. The wavelength range for their measurements was from 582 to 589 nm for rubidium, and for cesium was from 620 to 632 nm. In this laser light the ejected photoelectrons have a very low kinetic energy of only 25-100 meV, increasing the experimental difficulty significantly.

Using the equipment described in Chapter 2, we measured the photoelectron angular distribution in two-photon ionization for rubidium. The angular distribution was measured for eight different wavelengths in the wavelength range from 532.0 nm to 591.0 nm. Obviously, the total cross section in two-photon ionization is much smaller than that in one-photon ionization, so an intense laser beam was used. The average laser power was 10 mJ. The power and the rubidium atom beam density were controlled to a level such that the maximum probability of detecting an electron per laser shot was approximately 30%. For each data point, measurements of 2400 laser pulses were used. The light polarization was measured to be better than 1000:1. The polarization of the light was rotated by means of an optical Fresnel rhomb. Taking advantage of the symmetry of geometry, the data at angle Θ is the average of the data at Θ and $\Theta+180^{o}$.

Figure 4.2 shows the experimental results of the photoelectron angular distribution measurements. A correction for pile-up errors, assuming Poisson statistics, was applied. The maximum correction was 9%. The photoionization threshold corresponds to a laser excitation wavelength of 593.8 nm. The crosses are the experimental data points, and the solid line was obtained in a least mean squares fit of the analytical function (1.18) of the experimental points. The error bars for some of the data points are shown, representing the typical standard deviation calculated from the scatter in the count rate taken over several subsets of data at each angle. The deviation is quite consistent with the shot noise limit $\sigma \approx \sqrt{n}$ where n is the number of detected electrons.

These two-photon angular distribution measurements were done near the ionization threshold. Careful arrangement of the experimental setup was taken to make sure the area was free of electrical fields. For a wavelength of 591 nm the ionized photoelectron kinetic energy is as low as 0.0196 eV, corresponding to electron speed of 8.3×10^{6} meters per second. Because in the angular distribution measurements the trajectories of photoelectrons could be altered by the electric field, very weak electric fields in the flight

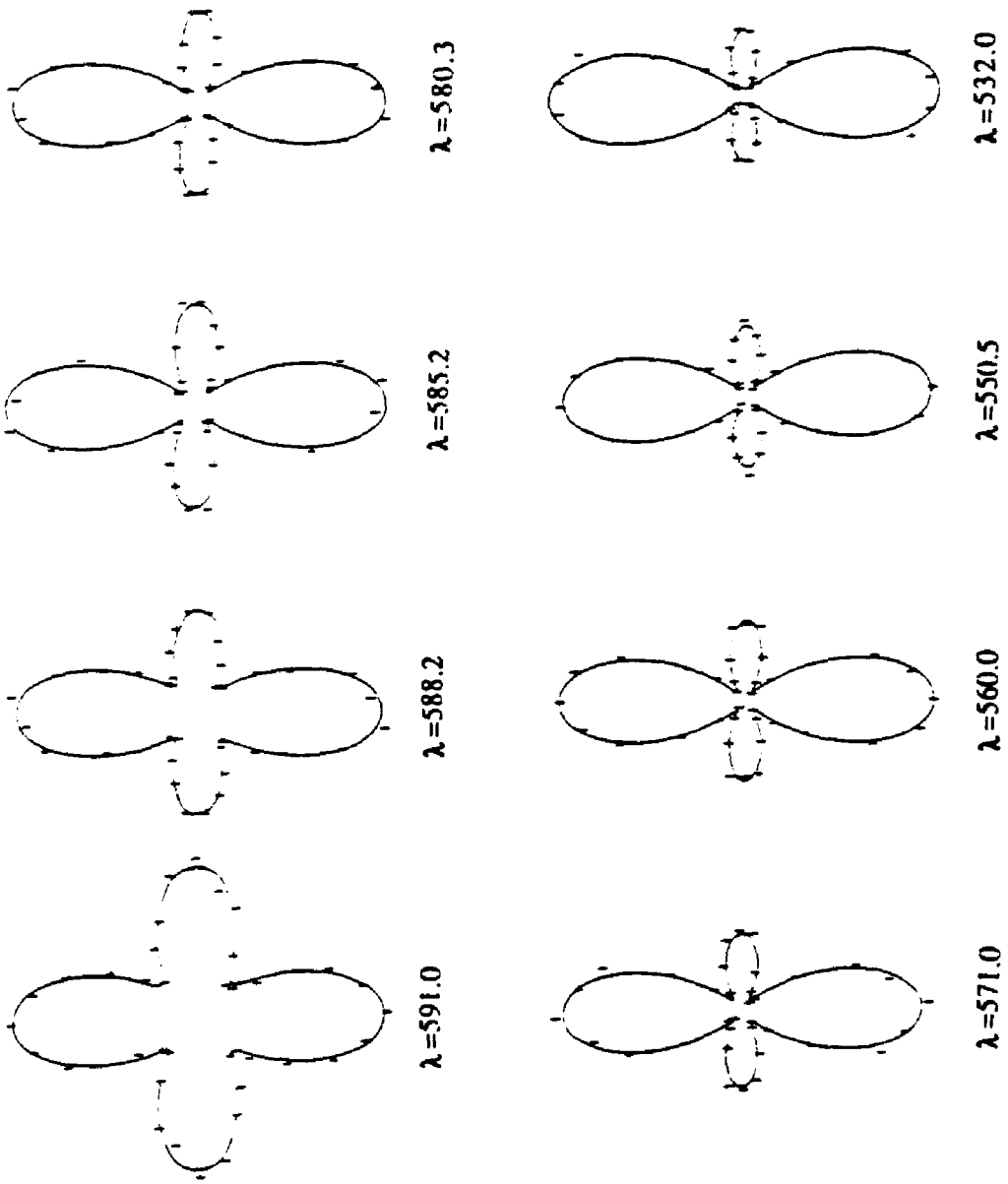

Figure 4.2 Two-photon ionization angular distributions of rubidium with light of wavelength from 532 to 591 nm. The laser polarization is in the vertical direction.

area could cause errors, especially at the wavelength near the ionization threshold. An attractive potential would accelerate the photoelectrons toward the detector. Those photoelectrons initially ejected away from the detector would be reversed if the field strength were large enough, and would arrive at the detector significantly later than the electrons initially ejected towards the detector, resulting in a time-delayed photoelectron pulse. In our observations these time-delayed electrons never appeared. These results showed that that residual electric field in the interaction region is very weak, less than 19.6 mev$\times$(2/qd). We conclude that this field only has a negligible effect on our measurement of the photoelectron angular distribution for wavelengths shorter than 585.2 nm. For larger wavelengths, the distribution could be more significant.

Table 4.1 Experimental results of measurement of rubidium for two-photon angular distributions, including asymmetry parameter α_2 and α_4. The uncertainties of each represent one standard deviation of the mean.

λ(nm)	ε(eV)	α_2	$\Delta\alpha_2$	α_4	$\Delta\alpha_4$
591.0	0.0196	-3.09	0.11	3.25	0.11
588.2	0.0396	-3.54	0.13	4.19	0.12
585.2	0.0612	-4.06	0.12	4.86	0.11
580.3	0.0970	-4.20	0.11	5.15	0.11
571.0	0.167	-4.48	0.18	5.78	0.18
560.0	0.251	-4.55	0.11	5.86	0.11
550.5	0.328	-4.67	0.17	6.24	0.18
532.0	0.485	-5.06	0.19	6.99	0.20

Figure 4.3 and figure 4.4 show the α_2 and α_4 values for different wavelengths of the incident photons. For comparison the

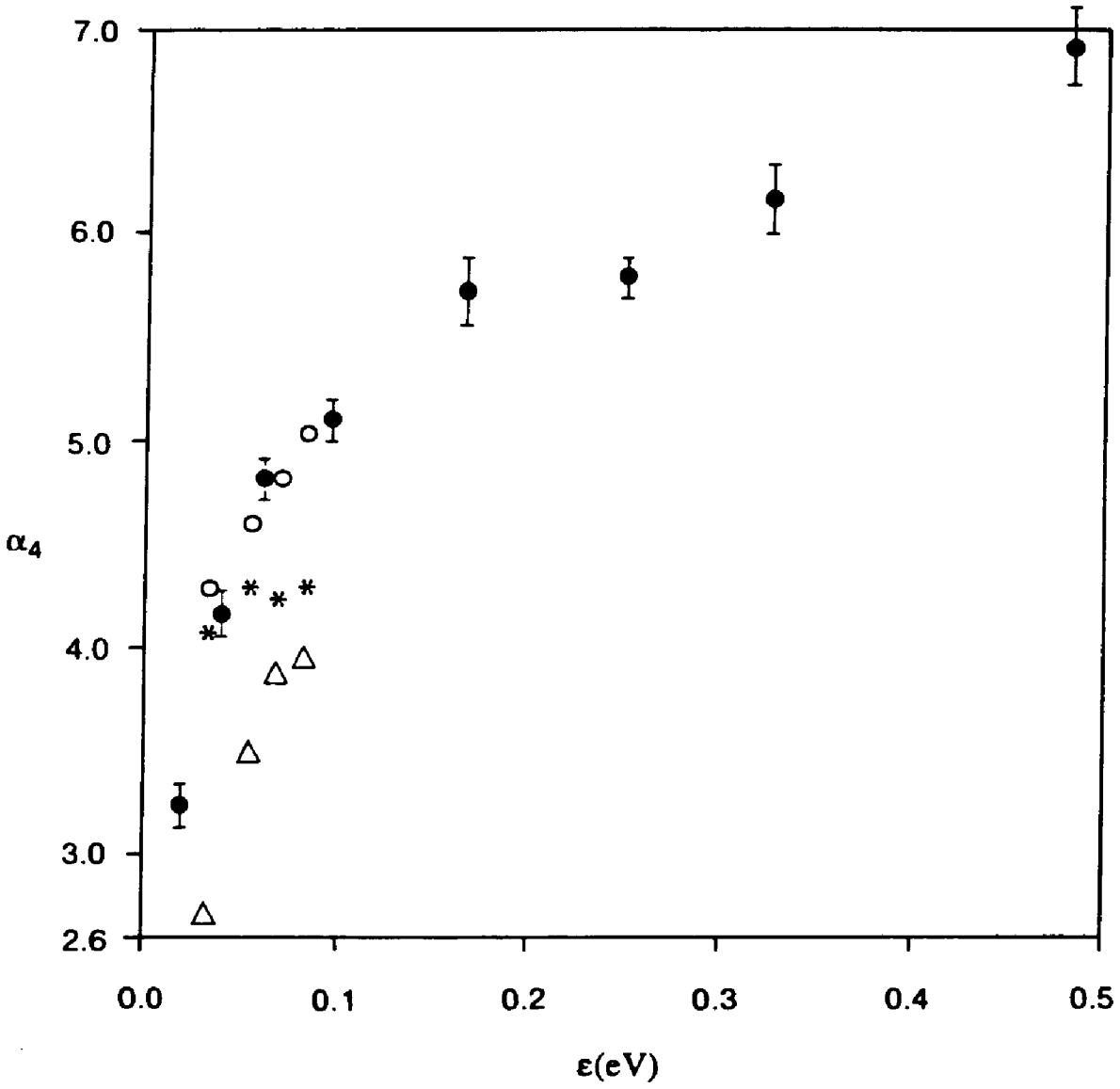

Figure 4.4 Parameter α_4 of rubidium $5^2S_{1/2} \rightarrow \varepsilon S_{1/2}$ and $\varepsilon D_{3/2,5/2}$ two-photon ionization vs. photoelectron energy ε. Data points represent the results of this work. Experiment results of Dodhy, Compton, and Stockdale [4.24] are shown as Δ's. The theoretical calculations are shown as o's for Sturmian method and ∗'s for Hartree-Fock method.

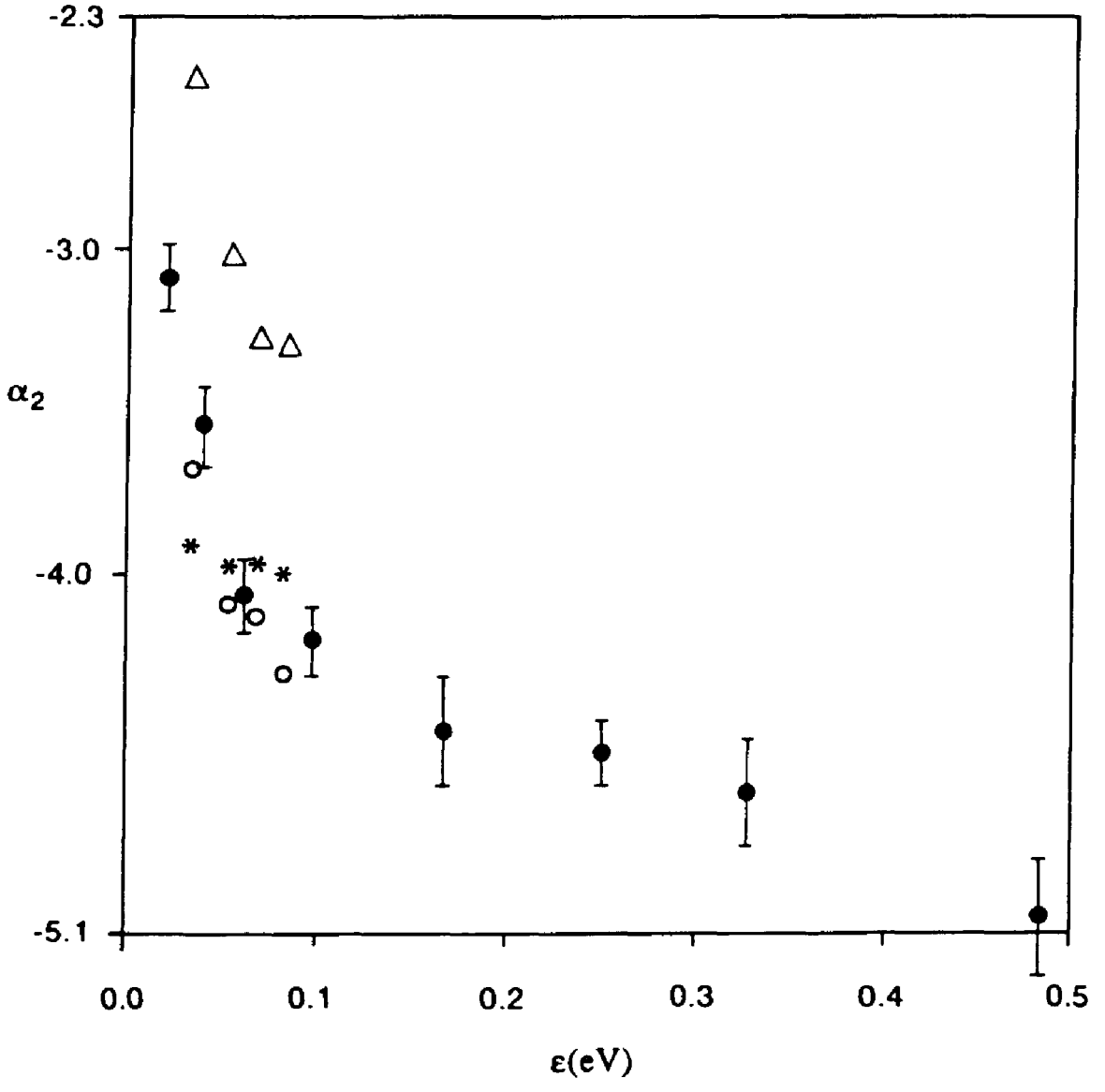

Figure 4.3 Parameter α_2 of rubidium $5^2S_{1/2} \rightarrow \varepsilon S_{1/2}$ and $\varepsilon D_{3/2,5/2}$ two-photon ionization vs. photoelectron energy ε. Data points represent the results of this work. Experiment results of Dodhy, Compton, and Stockdale [4.24] are shown as Δ's. The theoretical calculations are shown as o's for Sturmian method and ∗'s for Hartree-Fock method.

experimental data of Dodhy, Compton, and Stockdale [4.24] are drawn in the same diagrams. Results of theoretical calculations for α_2 and α_4 reported in [4.24] are shown in the same diagrams. One is from a Sturmian method calculation and the other is from a Hartree-Fock calculation.

Equation (4.16) was used to determine the quantum defect phase difference $\delta''_s - \delta''_d$. Bebb gave the parameters μ^o and μ' for rubidium (table 4.2).

Table 4.2 Quantum defect parameters of rubidium.

	μ_s^o	μ_s'	μ_d^o	μ_d'
Rb	3.134	-0.158	1.351	0.743

From this table we get the quantum defect parameter $\delta''_s - \delta''_d$ for different wavelengths. Using equations (4.15)-(4.24) we can determine the ratio $\frac{\sigma_s}{\sigma_d}$ and $\frac{\sigma_{5/2}}{\sigma_{3/2}}$. Table 4.3 lists the ratios and their uncertainties.

Table 4.3 The calculated ratio of $\frac{\sigma_s}{\sigma_d}$ and $\frac{\sigma_{5/2}}{\sigma_{3/2}}$, including their corresponding uncertainties.

λ(nm)	ε(eV)	δ_s-δ_d	$\frac{\sigma_s}{\sigma_d}$	$\frac{\sigma_{5/2}}{\sigma_{3/2}}$ (1)	$\frac{\sigma_{5/2}}{\sigma_{3/2}}$ (2)
591.0	0.0196	45.6°	0.390(95)	0.187(27)	22.7(2.21)
588.2	0.0396	48.7°	0.179(43)	0.178(23)	24.8(2.08)
585.2	0.0612	51.2°	0.207(49)	0.413(67)	6.63(0.87)
580.3	0.0970	54.5°	0.194(43)	0.466(72)	5.67(0.72)
571.0	0.167	59.8°	0.150(49)	0.53(15)	4.80(1.19)
560.0	0.251	64.9°	0.198(45)	0.76(20)	3.09(0.73)
550.5	0.328	69.1°	0.163(50)	0.66(20)	3.69(0.99)
532.0	0.485	75.5°	0.134(47)	1.13(1.04)	2.00(1.78)

These results are not in good agreement with other reports [4.25, 4.26]. Their reported calculation ratio of $\frac{\sigma_{5/2}}{\sigma_{3/2}}$ are from 1.4 to 1.7. The reason for the discrepancy is unknown. However, it is important to remember that photoelectron angular distribution measurements only provide two parameters, α_2 and α_4, from which only two of three atomic parameters, $\frac{\sigma_s}{\sigma_d}$, $\frac{\sigma_{5/2}}{\sigma_{3/2}}$, and phase shift δ_s-δ_d, can be determined.

As an alternative analysis, we may fix the ratio of $\frac{\sigma_{5/2}}{\sigma_{3/2}}$ at 1.6, and determine the parameters δ_s-δ_d and ratio of $\frac{\sigma_s}{\sigma_d}$. These results are shown in table 4.4.

Table 4.4 The calculated ratio of δ_s-δ_d and $\frac{\sigma_s}{\sigma_d}$.

λ(nm)	ε(eV)	δ_s-δ_d	$\frac{\sigma_s}{\sigma_d}$
591.0	0.0196	63.3°	1.128
588.2	0.0396	73.4°	0.839
585.2	0.0612	64.4°	0.423
580.3	0.0970	65.7°	0.366
571.0	0.167	69.3°	0.276
560.0	0.251	68.2°	0.247
550.5	0.328	73.9°	0.238
532.0	0.485	74.4°	0.133

These results are also not in good agreement with other authors results. Further experimental work and theoretical calculations are needed to get more information. The difficulty here comes in part from the fact that these measurements do not form a complete determination of the atomic parameters. We must depend on data determined by other means for one of these parameters, and then determine the other two. We see from the result of tables 4.3 and 4.4 that this procedure does not produce acceptable results, and a more "complete" experiment must be performed to rectify this. One solution is that of Kaminski, Kessler, Kollath [1.22] in which they experimentally determine the photoelectron angular distribution and the photoelectron spin polarization for two photon ionization of atomic cesium. The angular distribution with interfering interactions, described in the next chapter, also has the potential for making a complete determination of the atomic ionization parameters. This will be explored in future studies.

4.4 List of references

4.1 H. B. Bebb and A. Gold, "Multiphoton Ionization of Hydrogen and Rare-Gas Atoms", Phys. Rev., Vol. 143, p. 1, (1965).

4.2 H. B. Bebb, "Quantitative Theory of the Two-Photon Ionization of the Alkali Atoms", Phys. Rev., Vol. 149, p. 25, (1966).

4.3 A. Burgess and M. F. Seaton, "A General Formula for the Calculation of Atomic Photo-ionization Cross Sections", R. Astron. Soc., Vol. 120, p. 121, (1960).

4.4 A. Burgess, "Table of Hydrogenic Photoionization Cross-Sections and Recombination Coefficients", R. Astron. Soc. Mem., Vol. 69, P. 1, (1964).

4.5 J. Mizuno, "Two-Photon Ionization of Li, Na, and K with polarized Photons", J. Phys. B: Atom. Molec. Phys., Vol. 6, p. 314, (1973).

4.6 E. J. Robinson and S. Geltman, "Single- and Double-Quantum Photodetachment of Negative Ions", Phys. Rev., Vol. 153, p. 4, (1967).

4.7 P. Lambropoulos, "On Producing Totally Polarized Electrons Through Multiphoton Ionization", J. Phys. B: Atom. Molec. Phys., Vol. 7, p. L33, (1974).

4.8 M. S. Pindzola, "Two-Photon Excitation of Atomic Oxygen", Phys. Rev. A, Vol. 17, p. 1021, (1978).

4.9 A. Declemy, A.Ruchman, M. Jaoucn, and G. Laplanche, "Two-Photon Ionization of Alkali Atoms in the Framework of Infinite Summations and Spin-Orbit Coupling", Phys. Rev. A, Vol. 23, p. 1823, (1981).

4.10 P. Lambropolous and M. R. Teague, "Two-Photon Ionization with Spin-Orbit Coupling", J. Phys. B, Vol. 9, p. 587, (1976).

4.11 K. J. Kollath, "Theory for Laser Photoionization of Excited Atoms: $n^2P_{1/2,3/2}$ States of Cs", J. Phys. B. Atom. Molec. Phys. Vol. 13, p. 2901, (1980).

4.12 M. R. Teague and P. Lambropoulos, "Three-Photon Ionization with Spin-Orbit Coupling", J. Phys. B: Atom. Molec.Phys., Vol. 9, p. 1251, (1976).

4.13 M. S. Pindzola, "Two and Three Photon Ionization of Cesium", private communication.

4.14 G. Petite, F. Fabre, P. Agostini, M. Crance, and M. Aymar, "Nonresonant Multiphoton Ionization of Cesium in Strong Fields: Angular Distributions and Above-Threshold Ionization", Phys. Rev. A, Vol. 29, p. 2677, (1984).

4.15 P. R. Blazewicz, X. Tang, R.N. Compton, and J. A. D. Stockdale, "Photoelectron Angular Distributions From Resonantly Enhanced Multiphoton Ionization of Xenon via the $6s[3/2]_1{}^0$ and 6s States:Experiment and Theory", J. Opt. Soc. Am. B, Vol. 4, p. 770, (1987).

4.16 A. Dodhy, R. N. Compton and J. A. D. Stockdale, "Multiphoton Ionization of Rubidium Atoms Near the $4d^2D$ Quadrupole Transition", Phys. Rev. A, Vol. 33, p. 2167, (1985).

4.17 R. N. Compton, J. A. D. Stockdale, C. D. Cooper, X. Tang, and P. Lambropoulos, "Photoelectron Angular Distributions from Multiphoton Ionization of Cesium Atoms", Phys. Rev. A, Vol. 30, p. 1766, (1984).

4.18 A. Dodhy, A. D. Stockdale, R. N. Compton, X. Tang, P. Lambropoulos and A. Lyras, "Two-Photon Resonant Three-Photon Ionization nd^2D States of Cesium, Rubidium, and Sodium: Photoelectron Angular Distributions", Phys. Rev. A, Vol. 35, p. 2878, (1987).

4.19 D. Feldmann, D. Petring, G. Otto, and K. H. Welge, "Angular Distribution of Photoelectrons from Above-Threshold Ionization (ATI) of Xenon by 532 nm 355 nm and 266 nm Radiation", Z. Phys. D, Vol. 6, p. 35, (1987).

4.20 D. Feldmann, B. Wolff, M. Wemhoner, and K. H. Welge, "Above-Threshold-Ionization of Atomic Hydrogen: Angular Distribution of Photoelectrons", Z. Phys. D, Vol. 6, p. 293, (1987).

4.21 T. Hellmuth, G. Leuchs, S. J. Smith, and H. Walther, "Springer-Series in Optical Sciences", (edited by W. O. N. Guimaraes, C-T, Lin, and A, Mooradian), Vol. 26, p. 194, (1980).

4.22 E. H. A. Granneman and M. J. Van der Wiel, "Two-Photon Ionization Measurements in Atomic Caesium by Means of an Argon Ion Laser", J. Phys. B, Vol. 8, p. 1617, (1975).

4.23 M. Klewer, M. J. M. Beertlage, E. H. A. Granneman, and M. J. Van der Wiel, "Two-Photon Ionization Rates of Caesium for Linear and Circular Polarization (515-455 nm)", J. Phys. B, Vol. 10, p. L243, (1975).

4.24 A. Dodhy, R, N. Compton and A. D. Stockdale, "Photoelectron Angular Distribution for Near-Threshold Two-Photon Ionization of Cesium and Rubidium Atoms", Phys. Rev. Lett., Vol. 54, p. 422, (1985).

4.25 F. Arqueros, P. E. LaRocque, M. S. O'Sullivan, and B. P. Stoicheff, "Intensity Ratios of $^2D_{5/2,3/2} \leftarrow {}^2S$ Doublets in the Two-Photon Absorption Spectrum of Rb and Cs", Opt. Lett., Vol. 9, p.82, (1984).

4.26 B. Warner, "Atomic Oscillator Strengths-III", Mon. Not. R. Astr. Soc., Vol. 139, P. 115, (1968).

CHAPTER 5
INTERFERENCE OF BETWEEN ONE-PHOTON AND TWO-PHOTON IONIZATION PROCESSES

5.1 Introduction

In recent years a new type of interaction [1.31-1.34, 5.1-5.6] between an atomic system and a multi-frequency radiation field has attracted a lot of attention. This interaction is much different from what had been studied in the past.

In previously studied processes, each frequency component of the field induced a different step of the atomic transition. These interactions between the atom and components of the field are of a stepwise fashion. Some processes such as optical pumping, resonantly enhanced multiphoton absorption, and selective photodissociation are good examples of these interactions.

It is well known [1.35] that the enhancement of three-photon resonant five-photon ionization through the 6s state of Xe will diminish and eventually disappear into the nonresonant background, if the gas pressure is raised to a certain value. This may be explained by an interference between the absorption of the resonantly generated third harmonic and absorption of three pump-laser photons. If the magnitude and phase of the third harmonic are appropriate, the interference can be destructive, as in the cancellation of the excitation of the resonant state. A series of experiments done by Wynne and Jackson [5.1-5.2], Payne and Garrett [1.32], Miller, Compton, and Blazewicz [1.33, 1.34], Agarwal and Tewari [1.40] provided much insight into the interference physics of cancellation on resonance. This new type of interference represents another kind of interaction between an atomic system and a multi-frequency radiation field. Amplified spontaneous

emission and four-wave mixing, multiphoton ionization and third-harmonic generation, multiphoton ionization and stimulated Raman scattering, two-photon absorption, are all examples of this kind of interference.

Chen, Yin, and Elliott reported in 1990 the interference between two interactions in mercury atoms [1.43, 1.44]. In this process, the effect of a multi-frequency laser field on the net transition moment for absorption by an atom into an excited state was studied. This process involves the interaction of the mercury atom with a laser field and its third-harmonic in which three-photon absorption and one-photon absorption are induced simultaneously. When the third-harmonic radiation at frequency 3ω is incident upon an atom, it can be absorbed linearly by the atom, exciting the atom from the ground state to an excited state. The atom can also interact with the fundamental field at the fundamental frequency ω, which is approximately one-third of the transition frequency of the atom. The atom may absorb the fundamental frequency by a three-photon process. The atom is allowed to interact with both of the third-harmonic field and the fundamental field simultaneously, and could be excited to the upper state by a linear interaction or by a three-photon interaction. The effect of "simple" interference between two different but coherent pathways appears. The total transition rate depends not only on the intensity of these two fields, but also on the interference of these two fields, i.e the relative phase.

Another interference interaction was studied by Baranova, Chudinov, Shulginov, and Zel'dovich [1.46]. This work involved in interference of electrons ejected from the photomultiplier cathode. Using a picosecond pulse of a Nd laser, E_{ω}, and its second harmonic, $E_{2\omega}$, simultaneously to illuminate the photocathode of a PMT, they found that the ionization rate depends not only on the intensity but also on the relative phase between the laser field E_{ω} and its second harmonic $E_{2\omega}$. Other interference phenomena between six-photon and seven-photon above threshold ionization were reported by Muller, Bucksbaum, Schumacher, and Zaviyev [1.47]. Fairly large variations were found in their experimental study of multiphoton

ionization of krypton, irradiated simultaneously by an infrared laser beam and its second harmonic.

A long standing goal of photochemistry is the use of radiation to control the distribution of products in chemical reactions. The advanced properties of laser light: phase coherence, high intensity, short pulse duration, and monochromaticity provide an excellent tool for achieving this goal. The variation of the wavelength of the laser provides little control over the branching ratio for different reaction channels because the states excited by a single laser are usually superpositions spanning more than one set of possible products. Brumer and Shapiro [5.7-5.9] first proposed using two weak lasers to excite the molecule simultaneously by two distinct optical paths. The key property of these pulses is that they are coherent and have an adjustable phase difference. The pulse populates a coherent, degenerate state which correlates to a linear combination of the possible reaction products. By adjusting the relative phase of the two beams it is possible to alter this combination in such a way as to enhance one product channel at the expense of the other.

Park, Lu, and Gordon [5.10] reported their experiment of coherent control of the ionization of HCl in 1991. Using three 336 nm photons and one 112 nm photon to resonantly excite the intermediate $j^3\Sigma^-$ ($\Omega=0^+$) state of HCl molecular beam, they observed the coherent laser control of the resonance enhanced multiphoton ionization.

Enhancement and suppression were illustrated recently by Szoke, Kulander, and Bardsley [5.11], who presented, for one-dimensional short-range potential and simple model system, photoelectron energy spectra obtained by solving numerically the time-dependent Schrodinger equation. They described two different behaviors that result from the variation of the relative phase during simultaneous irradiation by a coherent laser beam and its harmonic, and found that they enhance and then suppress multiphoton ionization, depending on the relative phase or the two field components, even in the case of realistic, time-dependent pulses. For the case of a laser and its second harmonic, they presented both a one-dimensional and a three-dimensional calculation that showed a strong dependence of

the photoelectron angular distribution on the relative phases of the two colors, and a strong enhancement of the ionization probability by the second harmonic.

5.2 Principle of photoionization interference for two-color laser fields

The interference of the photoelectron angular distribution produced by two laser fields with different frequencies can be described through the following discussions. We concentrate in this study on the ionization of an alkali atom by a superposition of a linearly polarized optical field ω and its second harmonic field 2ω. When the fundamental field is incident on an alkali atom, the atom in ground state absorbs two photons and is ionized. As mentioned in chapter 4, the angular distribution cross section for two-photon ionization is:

$$\frac{d\sigma_1}{d\Omega} = \frac{1}{2}\left\{\left|T^0_{1++}\right|^2 + \left|T^0_{1--}\right|^2 + \left|T^0_{1+-}\right|^2 + \left|T^0_{1-+}\right|^2\right\}$$

$$\equiv \left|T_1(\theta)\right|^2, \qquad (5.1)$$

where T^0_{1++}, T^0_{1--}, T^0_{1+-}, and T^0_{1-+} are

$$T^0_{1++} = \left(E^{\omega}e^{i\phi_1}\right)^2\left[Y_{00}(\hat{R})e^{i\delta_0}\left(\frac{1}{9}\right)(S_1 + 2S_2)\right.$$
$$\left. + Y_{20}(\hat{R})e^{i\delta_2}\left(\frac{-2}{45\sqrt{5}}\right)(5S_3 + S_4 + 9S_5)\right] = T^0_{1--} \qquad (5.2)$$

$$T^0_{1-+} = \left(E^{\omega}e^{i\phi_1}\right)^2\left[Y_{21}(\hat{R})e^{i\delta_2}\left(\frac{1}{15}\sqrt{\frac{2}{15}}\right)(5S_3 + S_4 - 6S_5)\right] = T^0_{1+-}. \qquad (5.3)$$

The E^{ω} represents the fundamental field and ϕ_1 is the phase of the laser field. Here we may neglect the phase of radiation field.

Because the electron current received by the electron multiplier is proportional to the square of field amplitude, the photoelectron angular distributions are independent of the phase of the field.

If the atom is ionized by the second harmonic field, the one-photon absorption process is involved. The angular distribution, as shown in formula (1.18), is

$$\frac{d\sigma_2}{d\Omega} = \frac{1}{2}\left\{\left|T^0_{2++}\right|^2 + \left|T^0_{2--}\right|^2 + \left|T^0_{2+-}\right|^2 + \left|T^0_{2-+}\right|^2\right\}$$

$$\equiv \left|T_2(\theta)\right|^2, \qquad (5.4)$$

where T^0_{2++}, T^0_{2--}, T^0_{2+-} and T^0_{2-+} have the form

$$T^0_{2++} = \left(E^{2\omega}e^{i\phi_2}\right)\frac{1}{3\sqrt{3}}Y_{10}(\Theta,\Phi)\left(2R_{3/2} + R_{1/2}\right) = T^0_{2--} \qquad (5.5)$$

$$T^0_{2+-} = \left(E^{2\omega}e^{i\phi_2}\right)\frac{2}{3\sqrt{3}}Y_{11}(\Theta,\Phi)\left(R_{3/2} - R_{1/2}\right) = T^0_{2-+} \qquad (5.6)$$

and $E^{2\omega}$ represents the fundamental field and ϕ_2 is the phase of the laser field. Here we neglect the phase difference between $P_{3/2}$ and $P_{1/2}$ states, because in most situations this phase difference equals zero to a good approximation as mentioned in Chapter 3. As we indicated above the phase change of the field is neglected in this process.

Now let us consider that both the second-harmonic and the fundamental fields are incident on the atom. (Figure 5.1) In this situation the phase difference $2\phi_2 - \phi_1$ between these two fields can no longer be neglected because the relative phase difference between them is extremely important. The atom interacts with both the fundamental and the second-harmonic fields and is ionized by both fields. The one-photon ionization and two-photon ionization

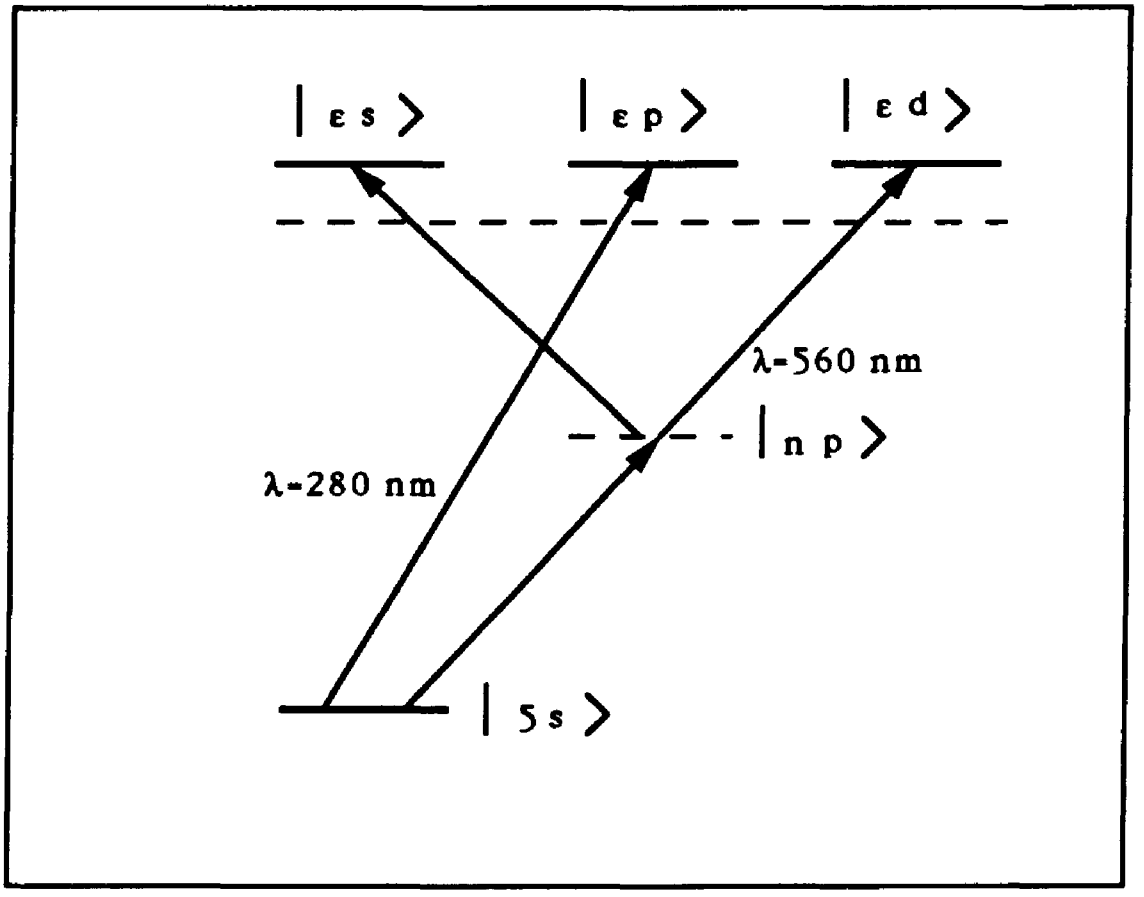

Figure. 5.1 Transition energy levers for interference between one-photon and two-photon ionization transitions.

processes described above are not valid and can not be treated separately. An interference between these two interactions may exist. The photoionization intensity received for this process is expressed as:

$$\frac{d\sigma}{d\Omega} = \frac{1}{2}\left\{\left|T^0_{++}\right|^2 + \left|T^0_{--}\right|^2 + \left|T^0_{+-}\right|^2 + \left|T^0_{-+}\right|^2\right\}$$

$$= \frac{1}{2}\left\{\left|T^0_{1++} + T^0_{2++}\right|^2 + \left|T^0_{1--} + T^0_{2--}\right|^2\right.$$

$$\left. + \left|T^0_{+-} + T^0_{2+-}\right|^2 + \left|T^0_{1-+} + T^0_{2-+}\right|^2\right\}$$

$$= \frac{1}{2}\left\{\left|T^0_{1++}\right|^2 + \left|T^0_{1--}\right|^2 + \left|T^0_{1+-}\right|^2 + \left|T^0_{1-+}\right|^2\right\}$$

$$+ \frac{1}{2}\left\{\left|T^0_{2++}\right|^2 + \left|T^0_{2--}\right|^2 + \left|T^0_{2+-}\right|^2 + \left|T^0_{2-+}\right|^2\right\}$$

$$+ \frac{1}{2}\left\{\left(T^0_{1++}T^{0*}_{2++} + T^0_{1--}T^{0*}_{2--} + T^0_{+-}T^{0*}_{2+-} + T^0_{1+-}T^{0*}_{2+-}\right) + \text{c. c.}\right\} \qquad (5.7)$$

Using equations (5.1) and (5.4), we get

$$\frac{d\sigma}{d\Omega} = \left|T_1(\Theta)\right|^2 + \left|T_2(\Theta)\right|^2 + \left(E^{\omega}e^{i\phi_1}\right)^2\left(E^{2\omega^*}e^{-i\phi_2}\right)$$

$$\left\{Y_{00}Y^*_{10}e^{i(\delta_0-\delta_1)}\left(\frac{1}{9}\right)\frac{1}{3\sqrt{3}}\left(2R_{3/2}+R_{1/2}\right)\left(2S_1+S_2\right)\right.$$

$$\left. + Y_{20}Y^*_{10}e^{i(\delta_2-\delta_1)}\frac{-2}{45\sqrt{5}}\frac{1}{3\sqrt{3}}\left(5S_3+S_4+9S_5\right)\left(2R_{3/2}+R_{1/2}\right)\right.$$

$$+ Y_{21}Y_{10}^{*}e^{i(\delta_2-\delta_1)}\frac{\sqrt{2}}{15\sqrt{15}}\frac{\sqrt{2}}{3\sqrt{3}}(5S_3+S_4-6S_5)(R_{3/2}-R_{1/2})\}$$

$$+c.c. \qquad (5.8)$$

If we put the group factors (4.15-4.17) into equations (5.8), this equation becomes

$$\frac{d\sigma}{d\Omega}=|T_1(\Theta)|^2+|T_2(\Theta)|^2+\frac{2(E^{\omega})^2E^{2\omega'}\cos\theta}{36\pi(R_{3/2}-R_{1/2})}\{Ax\cos(\delta_0-\delta_2+\delta)$$

$$-Bx(3\cos^2\Theta-1)\cos\delta+C(1-\cos^2\Theta)\cos\delta\}, \qquad (5.9)$$

where $\delta=\delta_2-\delta_1+2\phi_1-\phi_2$. Using $\tilde{A}=A/B$, $\tilde{C}=C/B$ to replace A, B and C, and considering

$$\cos(\delta_0-\delta_2+\delta)=\cos(\delta_0-\delta_2)\cos\delta-\sin(\delta_0-\delta_2)\sin\delta \qquad (5.10)$$

$$K=\frac{(E^{\omega})^2E^{2\omega'}}{36\pi}\frac{2B}{(R_{3/2}-R_{1/2})}, \qquad (5.11)$$

we get the final formula

$$\frac{d\sigma}{d\Omega}=|T_1(\Theta)|^2+|T_2(\Theta)|^2+K\cos\theta\{[\tilde{A}x\cos\delta_{02}-x(3\cos^2\Theta-1)\delta_{02}$$

$$+\tilde{C}\sin^2\Theta]\cos\delta-\tilde{A}x\sin\delta_{02}\sin\delta\}, \qquad (5.12)$$

where $\delta_{02}=\delta_0-\delta_2$ is a constant for a given wavelength. The factors $\tilde{A}$, $\tilde{B}$, and x have already been determined through one-photon ionization and two-photon ionization experiments discribed in Chapter 3 and 4. Equation (5.12) is the function of the phase difference δ. This exhibits the importance of the relative phase

difference in interfering multi-photon ionization processes. Figure 5.2 shows the calculated interference pattens of photoelectron angular distributions. Here although we discuss the effect of interference on the angular distribution of photoionization specifically for the fundamental field and second-harmonic field, these arguments can be extended to other similar interference phenomena as well.

5.3 Experimental setup for observation of photoionization interference

In this interference experiment, the equipment we used and experimental procedures we followed are basically similar to those we discussed in chapter 2. In order to control the relative phase difference of the fields, we inserted a gas cell in front of the interaction area as a dispersion cell. This gas cell was filled 99.99% pure nitrogen, although any other nonabsorbing gas for the fundamental and second-harmonic laser fields could be used. Passing through the gas cell, these two laser fields of different frequencies experience different phase delays. The following formula determined the change of the phase difference $2\phi_2 - \phi_1$:

$$\frac{\Delta(2\Phi_2 - \Phi_1)}{\Delta P} = \frac{2(n_2 - n_1)L}{P_0 \lambda} \qquad (5.13)$$

where ΔP is the pressure change in gas cell, n_1, n_2 are refractive indices for fundamental and second harmonic laser fields separately under standard condition STP, and L is the path length of laser light in gas cell. For pure nitrogen n_2-n_1 equals 1.617×10^{-5} for 280 and 560 nm wavelength [5.12]. L is 13 cm in our experiment. In order to induce a complete 2π phase shift between these two interference terms, a change of 101.2 torr nitrogen pressure is required. Under this change of pressure the angular distribution of the photoelectron is expected to change through one complete cycle.

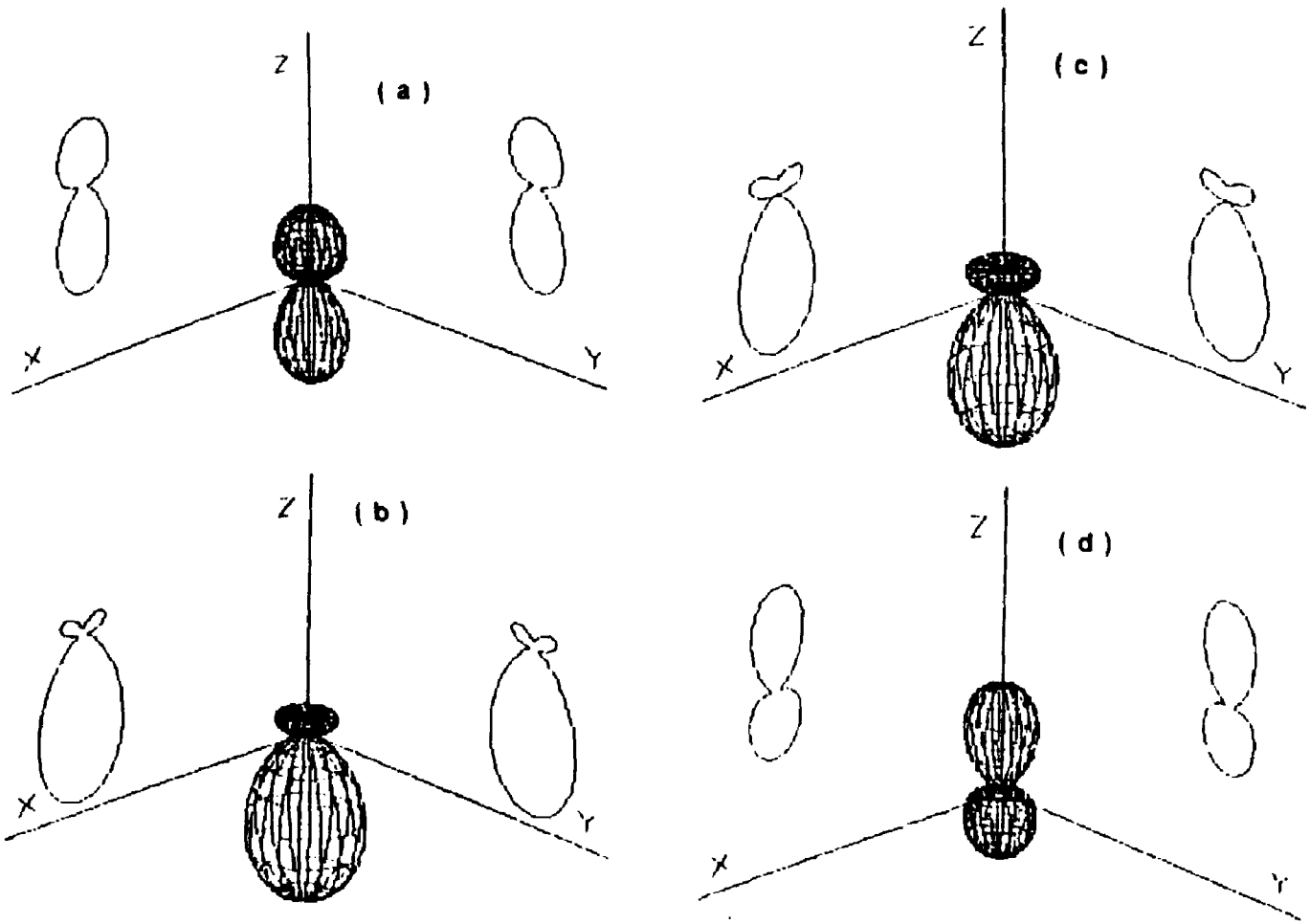

Figure.5.2 Calculated interference pattens of photoelectron angular distributions. (a) $-\pi/2$, (b) 0, (c) $\pi/4$, (d) $\pi/2$.

The fundamental laser was chosen at the wavelength of 560 nm. The second harmonic was generated by passing the dye laser through a β-BaB_2O_4 crystal phase matched for type 1 doubling. The polarization of second harmonic was measured to be 5000:1. The phase matching condition ensured that the generated 280 nm light has a definite and stable phase relationship to the fundamental. The fundamental light was linearly polarized in the vertical direction, and the second harmonic produced by the crystal was polarized horizontally. A zero order waveplate was used to rotate the fundamental light 90 degrees to the horizontal direction. The polarization of fundamental light was measured to be 4000:1. Careful adjustment was done to make these two light polarizations parallel to within less than one degree.

One of the critical techniques for obtaining interference in the angular distributions of the photoelectrons is to obtain a fixed phase difference between these two fields. There are many factors which influence the phase difference between these two fields: possible position drift and mode change of Nd: YAG second-harmonic laser light, the fluctuations of dye laser which mainly comes from motion of dye solution, the drift of optical components, the perturbation of air, the vibrations from different electrical instruments, vacuum pump (mechanical pump, cryopump), cooling system, fans, etc. All those factors will not only change the phase difference time by time but also change the dye laser mode structure and ruin the interference effect. Unfortunately, because our vacuum system in which the atomic beam was generated was installed separately from the optical table, in order to keep the relative position between laser beam and atomic beam fixed, we can not float the optical table to avoid outside vibrations which make the experiment especially difficult.

Another critical technique in this interference experiment is that a good Gausian beam is required. Although the dye laser is pumped longitudinally by the second-harmonic of the Nd: YAG laser to get the nearly TEM_{00} mode, after three stages of dye amplifiers the

transverse mode of the output dye laser is strongly influenced by the mode structure of the Nd: YAG laser pump light. The Nd: YAG laser is an unstable cavity. After a long time its output is not a well-defined Gaussian mode. We adjusted the Nd: YAG cavity such that its second harmonic output is somewhat close to a round and uniform pattern. When adjusting the dye laser oscillator, we make the dye laser beam profile on the card as round and uniform as possible. The three stages of the dye amplifier will affect the dye laser quality strongly. The pumping beams are focused to the dye amplifier cells in a proper size to ensure the most efficient amplification. The profile of the output of the dye laser is very sensitive to the relative position of the pumping beam and the laser beam at the amplifiers. The stability of the dye laser system, which is influenced by many factors, also sets a limit to the data taking time.

In doing this interference experiment, two methods were considered:

1) A fundamental laser beam with vertical polarization is passed through a β-BaB_2O_4 crystal, and creates a second-harmonic field which vibrates in the horizontal direction. The polarizations of the fundamental and second-harmonic beams are aligned by passing through a polarizer. Then a rhomb is used to rotate the polarization of the two beams in order to measure the photoelectron angular distributions.

The advantage of this method is that the visible beam and ultraviolet beam go through exactly the same path and the same components, so when the fixed phase difference is established, it is relatively easy to maintain. The disadvantage of the method is that in order to keep these two laser beams with large difference of frequency in exactly the same path, all the optical components after β-BaB_2O_4 crystal (include β-BaB_2O_4 crystal) are required to be perfectly parallel, flat, highly achromatic and to display very little absorption over a very wide frequency range. By calculation only 3×10^{-4} rad deviation between these two beams may destroy the interference between them. Obviously this is a high standard which is not easily satisfied.

2) The second-harmonic beam and fundamental beams pass through separate paths, then we make these two beams overlap and enter vacuum chamber to interact with the atomic beam. By using this method, one could prevent the requirement of perfect optical components. Intensity matching of these two laser fields is relatively easy, because these two beams can be controlled separately. But since two beams go different ways, a very little vibration of the optical components or any perturbation may make the interference impossible. Another difficulty is the optical path adjustment. As mentioned above, even very small deviations would destroy the interference, so very careful adjustment is required in this interference experiment.

We chose the second method. The experimental set-up is shown in figure 5.3. We arranged a path with a shape of a parallelogram to guarantee that almost the same optical path length is following by both beams, and to avoid the influence of dye laser beam motion.

In order to get a very good Gausian beam, three pinholes were used to obtain a uniform and round laser spot. They were installed after the dye laser oscillator, between the second and third stages of the amplifier, and after the third stage of the dye laser separately. In addition to these methods an optical spatial filter was designed. A pair of lenses was used to focus the laser light and a 0.55 mm pinhole was put at the focal point. After these careful adjustments, the output of the dye laser system was measured to be very close to TEM_{00} mode and its beam profile is shown as in figure 5.4. Figure 5.4 (a) is the horizontal profile, and (b) is the vertical profile.

We used two 1.85 inch diameter, 3/8 inch thick fused silica optical flats as the windows. As mentioned previously, only a non-dispersive optical system can maintain the transverse and longitudinal overlap of the fundamental and second harmonic fields. A wedged window is like a prism. Two parallel windows were used for the front entrance and rear exit of the chamber to avoid prism effects. Another effect would influence the overlap even if the windows are highly parallel. If the field is incident upon the window

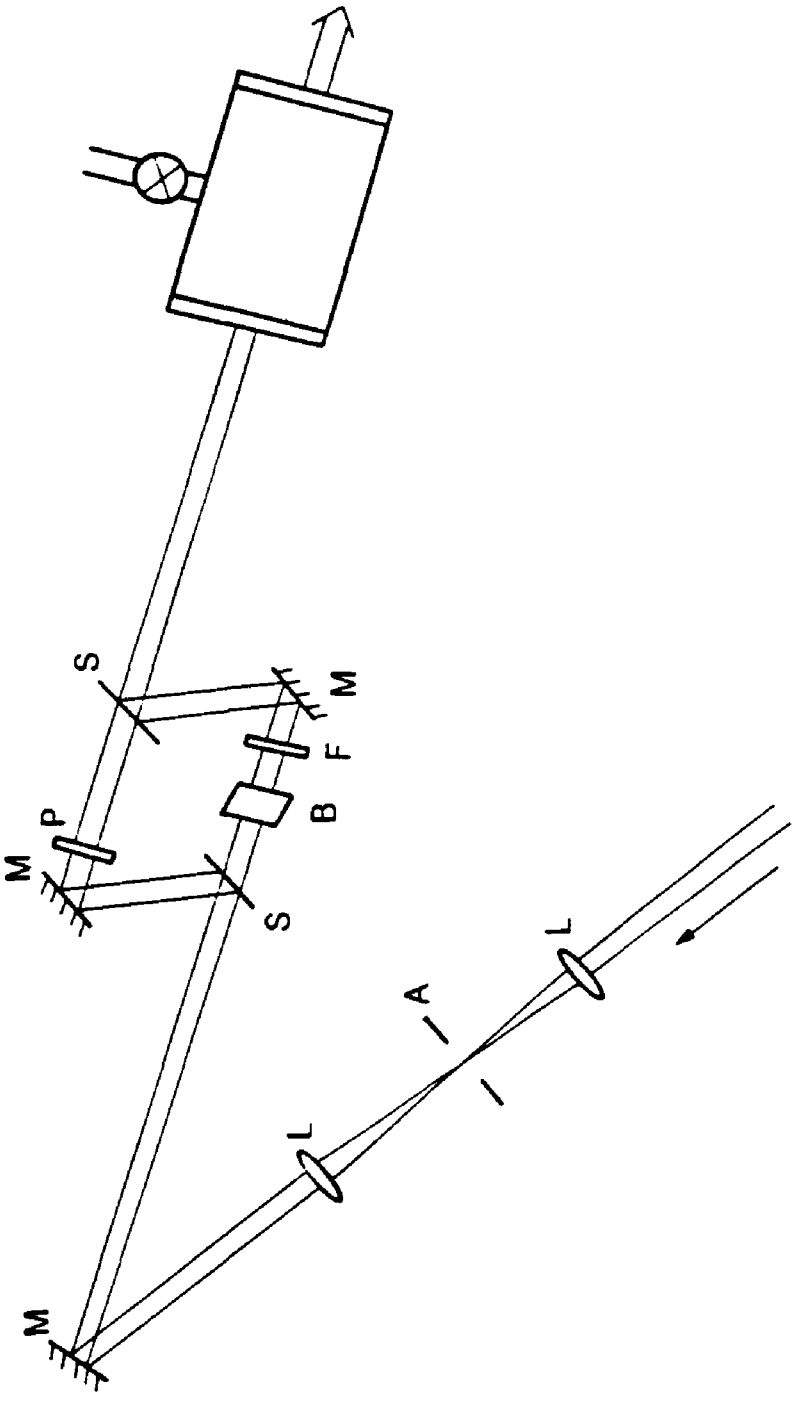

Figure 5.3 Interference experimental setup. (A) aperture, (B) β-$B_aB_2O_4$ crystal, (F) Lens, (M) millors, (P) half waveplane, (S) beam spliters.

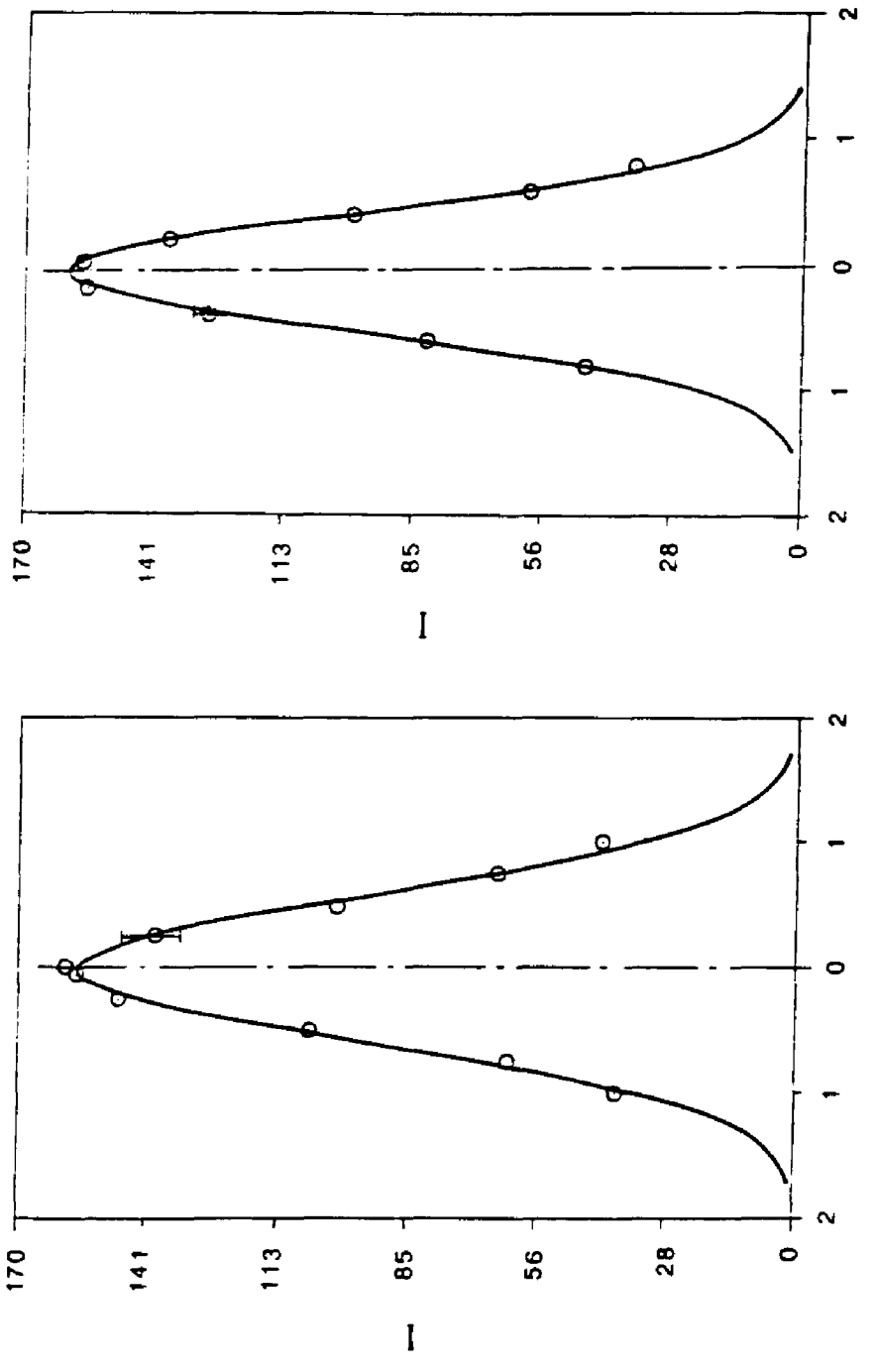

Figure 5.4 Gausian beam profiles. (a) the holizontal profile, (b) the vertical profile.

at an angle other than normal incident, it may cause a "walk off" of the two components of the field with different wavelength.

When we measured the one-photon or two-photon angular distributions, an optical rhomb was used to rotate the polarization of laser light. The detector was fixed perpendicular to the plane of laser beam and atomic beam. In order to measure interference between one- and two-photon ionization processes the angular distribution must be measured simultaneously in the different directions. A detector array, which consisted of four photoelectron detectors, was designed to collect the ejected electron in different directions. The schematic of the detector array is shown in figure 5.5. Each detector consisted of an electron lens and an electron multiplier. They are arranged at orientations of 0°, 45°, 90°, and 180° where 0° and 180° are each in the direction of the light polarization. Each detector has an angular resolution of nine degrees. Careful adjustment was done to ensure good alignment. Each detector had a separate high voltage power supply so the gain could be controlled to get balance between different channels. Every detector was connected to an independent delay and gate system. The gate in each channel needed to be adjusted carefully to get the best ratio of signal to noise.

In this interference experiment, the overlap of the two beams is very important. We adjusted and fixed the fundamental laser beam first, making sure that it passed the atomic beam and got the largest ionization electron signal. Then we adjusted the uv laser to overlap with visible laser. Because of the large difference between one- and two-photon ionization processes the laser intensities of the visible and the uv beams were very different. The uv laser at 100 μJ produced about the same number of electrons as the visible beam at 4 mJ. The intensity difference of these two laser beams makes the adjustment of the overlap difficult by. Two photodetectors which were installed before and after the interaction area were used to determine the position of laser beams. Each detector has a pinhole diameter of 0.75 mm and 0.85 mm respectively. The sizes of the pinhole are determined by the diameter of laser beam, so that the

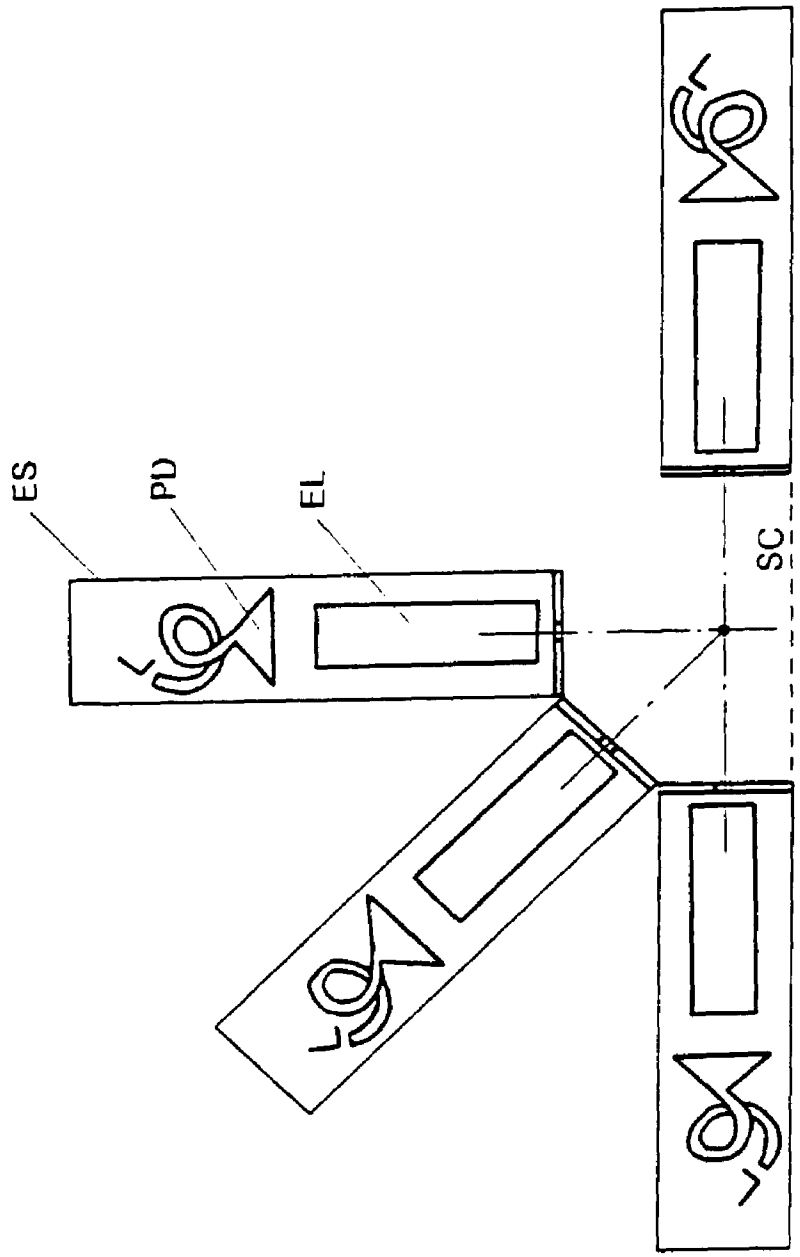

Figure 5.5 Photoelectron angular distribution detector array. The detectors are instaled at 0°, 45°, 90°, and 180° seprately.

measurement of position is most sensitive. Using these detectors the position error of laser may be as small as 5 μm.

Careful adjustment of normal incidence at the two parallel windows during the interference experiment was very important. It seems that the normal incidence of the fields onto the rear window and the front window of the chamber is much more critical than we estimated by calculation. By our adjustment the incidence angle is better than 0.3° from normal.

In order to get the best interference effect, a one-photon ionization signal must be comparable to the two-photon ionization signal at their maximum ejection direction. For rubidium at the wavelength of our laser, both interactions have the maximum of the angular distribution at $\Theta=0^{\circ}$. With the ultraviolet beam blocked we observed the familiar two-photon ionization angular distribution patten, and then with the fundamental beam blocked the one-photon ionization pattern was observed. Adjusting the energies of these two lasers one may get equal signals for these two ionization processes. Carefully choosing the ratio of the beam splitter we may satisfy this condition. In our experiment a 35% reflection beam splitter was used.

5.4 Experiment results of interference between one- and two-photon ionization processes

The interference phenomena between one- and two-photon ionization processes in rubidium was observed (figure 5.6). Pulse energies of 4 mJ and 100 μJ for fundamental and second harmonic laser beams respectively were used. The photoelectron signal received by four detectors are shown in figure 5.6 as function of nitrogen pressure in the gas cell. Each data point in figure 5.6 was determined from 900 laser shots. The maximum data count represents nearly 180 photoelectrons, the error bar shown for some of the data points is the standard deviation of the mean. The solid line is the least mean square fit to the data by adjusting the period, amplitude and phase of a cosine function and the average DC level. This figure shows that the total ionization signal is modulated by the

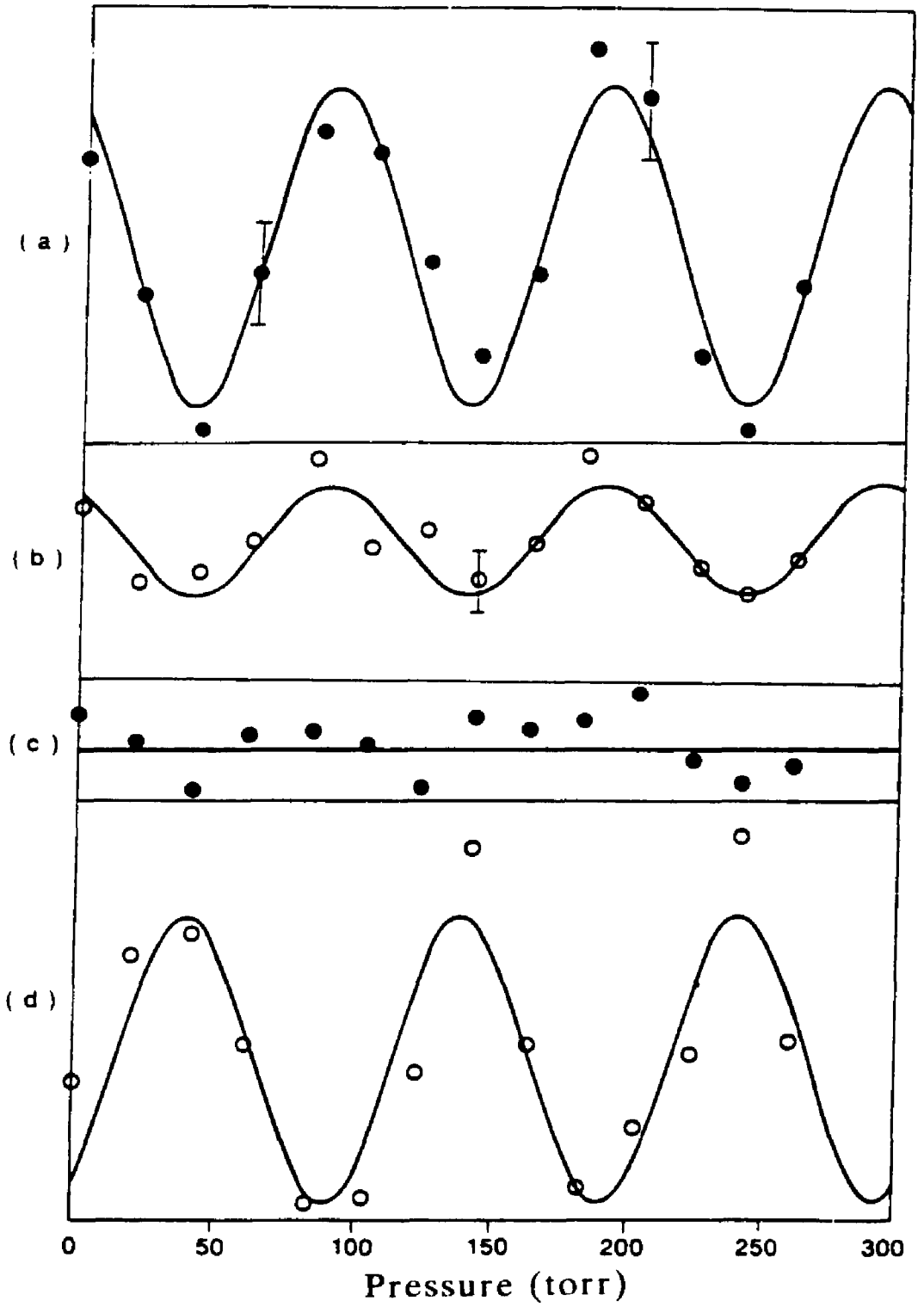

Figure 5.6 Experimental results for interference between one-photon and two-photon ionization processes. (a) 0, (b) $\pi/4$, (c) $\pi/2$, (d) π.

nitrogen pressure change. From this diagram the nitrogen pressure difference corresponding to the phase change 2π is 104 torr, in reasonable agreement with our calculation. The depth of modulation for the 0° and 180° signals close to 50%. This could be improved through better matching of the transition amplitude for the individual interactions. Further improvement of the interference conditions such as beam overlap of two laser beams, transverse mode structure, or vibration of laser beam, could help get better interference patterns.

As mentioned above we have gotten the angular distribution for interference in equation (5.12). Putting the data for $\tilde{A}$, $\tilde{C}$, x, and δ_{02} obtained in Chpter 3 and 4 into this equation we get:

$$\frac{d\sigma}{d\Omega} = |T_1(\Theta)|^2 + |T_2(\Theta)|^2 + K\cos\Theta\{[0.577 - 3.36(3\cos^2\Theta - 1)$$

$$+ 0.415\sin^2\Theta]\cos\delta + 1.23\sin\delta\}. \qquad (5.14)$$

At $\Theta=0$, from our experiment data we may get

$$\frac{d\sigma}{d\Omega} = 37.6 + 22.5\cos(\delta - \varphi_0), \qquad (5.15)$$

where the φ_0 equals 169°. Correspondingly we get the photoelectron angular distributions for $\Theta=\pi/4$, $\Theta=\pi/2$, and $\Theta=\pi$ respectively

at $\Theta=\pi/4$

$$\frac{d\sigma}{d\Omega} = 11.6 + 3.84\cos(\delta - \varphi_{\pi/4}), \qquad (5.16)$$

where $\varphi_{\pi/4}$ equals 126°.

at $\Theta=\pi/2$

$$\frac{d\sigma}{d\Omega} = 9.44, \qquad (5.17)$$

at $\Theta=\pi$

$$\frac{d\sigma}{d\Omega} = 37.6 - 22.5\cos(\delta - \varphi_\pi), \qquad (5.18)$$

where φ_π equals φ_o.

For the calculations of $\Theta=\pi/2$ and $\Theta=\pi$ agreement was obtained with our experiment result. For $\Theta=\pi/4$ the modulation of this signal of nearly the same phase as the $\Theta=0$ signal, but the statistics are not sufficient to determine this phase shift with precision. Future investigations are planned to determine their phase shifts δ_2-δ_1. Measurement of φ_Θ vs. Θ would give us more detail about the phase shift. In future studies we will explore the potential of using this phase shift to determine relative strengths of transition elements to continuum states.

Our experiment is the first successful demonstration of using interference for control of final states. This work demonstrates experimentally the possibility of coherent control over a process. This is meaningful in light of recent studies of phase control of chemical reactions.

5.5 List of references

5.1 J. J. Wynne, "Polarization Renormalization due to Nonlinear Optical Generation", Phys. Rev. Lett., Vol. 52, p. 751, (1984).

5.2 D. J. Jackson and J. J. Wynne, "Interference Effects Between Different Optical Harmonics", Phys. Rev. Lett., Vol. 49, p. 543, (1982).

5.3 P. R. Blazewicz and J. C. Miller, "Nonlinear Optical Processes in Xenon and Krypton Studied by Two-Color Multiphoton", Phys. Rev. A, Vol. 38, p. 2863, (1988).

5.4 G. S. Agarwal and S. P. Tewari, "Quantum Theory of the Competition between Multiphoton Ionization and Third-Harmonic Generation", Phys. Rev. A, Vol. 29, p. 1922, (1982).

5.5 R. M. Potvliege and P. H. Smith, "Two-Colour Multiphoton Ionization of Hydrogen by an Intense Laser Field and Its Third Harmonic", J. Phys. B: Atom. Mol. Opt. Phys., Vol. 24, p. L641, (1991).

5.6 K. J. Schafer and K. C. Kulander, "Phase-Dependent Effects in 1ω-2ω Multphoton Ionization", submittal to Phys. Rev. A.

5.7 P. Brumer and M. Shapiro, "Control of Unimolecular Reactions Using Coherent Light", Chem. Phys. Lett., Vol. 126, p. 541, (1986).

5.8 P. Brumer and M. Shapiro, "Coherent Radative Control of Unimolecular Reactions", Faraday Dis. Chem. Soc., Vol. 82, p. 177, (1986).

5.9 M. Shapiro and P. Brumer, "Laser Control of Product quantum State Populations in Unimolecular Reactions", J. Chem. Phys., Vol. 84, p. 4103, (1986).

5.10 Seung Min Park, Shao-Ping Lu, and Robert J. Gordon, "Coherent Laser Control of the Resonance-Enhanced Multiphoton Ionization of HCl", J. Chem. Phys., Vol. 94, p. 8622, (1991)..

5.11 A. Szoke, K. C. Kulander, and J. N. Bardsley, "Simple Calculations on Two-Colour Multiphoton Ionization", J. Phys. B: Atom. Molec. Opt. Phys., Vol. 24, p. 3165, (1991).

5.12 E. W. Washburn, "International Critical Tables of Numerical Data, VII", McGraw-Hill Book Co., New York, p. 11, (1930).

CHAPTER 6
CONCLUSION

Photoelectron angular distributions provide an important tool to study atomic structure. They are used to investigate the effect of spin-orbit coupling on relative cross-section for different ionization channels, continuum state phase shifts, and interference phenomena between different ionization processes for alkali atoms.

We experimentally studied the interference phenomenon between one-photon and two-photon ionization in rubidium by measuring the photoelectron angular distribution. Using a detector array with four detectors to collect the photoelectron distributions simultaneously, and by changing the nitrogen pressure in the dispersion cell, we were able to externally control the phase difference of fundamental and second-harmonic fields and directly study the interference phenomenon. We observed that photoelectron angular distribution patterns which appear from the 5S state of rubidium varied periodically with the change of the relative phase.

We also measured the energy dependence of photoelectron angular distributions of cesium and rubidium in the single-photon ionization from its ground state to continuum in the vicinity of a Cooper minimum. Our work clearly shows the effect of spin-orbit coupling on the one-photon ionization processes. The asymmetry parameter has the general shape expected on the basis of ab initio calculations. Good agreement is found between our asymmetry parameter β and the results of measurements of Fano effect and with calculated results of Norcross.

Two-photon ionization was also studied through measurements of photoelectron angular distribution. These processes are influenced by spin-orbit coupling and quantum defects.

In the ionization process induced by an optical field the phase of the field does not often produce direct observables. The interference between different optical processes is an important exception to this rule. Because of the existence of two or more pathways induced by different fields, the interactions depend on the phase relations between the fields.

To carry out these studies, we have developed and constructed the dye laser system, high vacuum system, optical system, photoelectron measurement system, and data analysis process. Similar experimental setups and methods can be applied to the studies of any phase sensitive processes including potential applications in coherent control of chemical reactions.

The experiments we have done are new and quite significant. However there is room for improvements and future studies. For example, a recycling alkali oven will allow us to work at a much longer time and higher atomic density in the interaction region. Under high atomic density, a smaller pinhole in the photoelectron collector may be used to get higher resolution. A more stable experimental system and a better control over the experimental conditions can produce quantitatively more respectable measurements of the depth of modulation of the ionization signal. All these improvements are needed in carrying out further investigations of photoelectron angular distributions and the interference phenomenon.

VITA

VITA

Yi-Yian Yin was born in Shanghai, China in 1946. He received the B.S. degree in Physics from Fudan University, Shanghai in 1968, the M.S. degree in Physics from Fudan University in 1981.

He worked as a engineer for ten years and an university assistant professor for five years in China. Currently he is working towards his Ph.D degree at the Electrical Engineering Department of Purdue University, West Lafayette, Indiana, U. S. A.